

ABSTRACT

# Extending Coherence in Superconducting Qubits: from microseconds to milliseconds

Adam Patrick Sears

2013

Circuit quantum electrodynamics (circuit QED) is the extremely successful framework for studying quantum devices developed along with the transmon, a superconducting charge qubit with an insensitivity to several types of dephasing. It involves the description of superconducting qubits and harmonic oscillators as quantized circuits. This thesis describes the implementation of two experiments that reduce circuit QED to its simplest components. Both experiments utilize elements that are known to have low dissipation: excited electron spin defects in crystals may take seconds to decay at cryogenic temperatures and the Josephson junction in superconducting qubits is nearly lossless; we begin by discussing the proper perspective for the remaining lossy elements. In the first experiments, a collection of magnetic dipoles is coupled as an ensemble to a superconducting resonator to investigate their suitability as a quantum memory; in the second a transmon “artificial atom” is placed inside a three-dimensional superconducting box. We further extend the study of the “3D transmon” and the harmonic oscillator modes of its rectangular waveguide cavity in terms of a new description of their hybridization (Black-box Quantization). Finally, we identify and resolve issues of photon induced dephasing in the first new devices. This thesis follows the evolution of superconducting qubits from coherence times of several microseconds to nearly a millisecond.

Extending Coherence in Superconducting Qubits:  
from microseconds to milliseconds

A Dissertation  
Presented to the Faculty of the Graduate School  
of  
Yale University  
in Candidacy for the Degree of  
Doctor of Philosophy

by  
Adam Patrick Sears

Dissertation Director: Professor Robert J. Schoelkopf

May 2013

© 2013 by Adam Patrick Sears  
All rights reserved.

---

# Contents

---

<b>Contents</b>	<b>iv</b>
<b>List of Figures</b>	<b>viii</b>
<b>Acknowledgements</b>	<b>xii</b>
<b>Publication list</b>	<b>xiii</b>
<b>1 Introduction</b>	<b>14</b>
1.1 Thesis Organization . . . . .	17
<b>2 Resonators and Dissipation</b>	<b>20</b>
2.1 Circuit Resonators . . . . .	21
2.1.1 Participation Ratio . . . . .	22
2.2 Transmission Line Resonators . . . . .	22
2.2.1 Quarter-wave Resonators . . . . .	23
2.2.2 Coplanar Waveguide . . . . .	26
2.3 Rectangular Cavities . . . . .	29
2.3.1 Rectangular Waveguide . . . . .	29
2.3.2 Dielectric Loss . . . . .	31
2.3.3 Conductor Loss . . . . .	33
2.3.4 Power Coupling . . . . .	34
2.3.5 Conclusions . . . . .	38
<b>3 Circuit QED</b>	<b>39</b>
3.1 Introduction . . . . .	40
3.2 Cooper-pair Box and Transmon . . . . .	41

3.2.1	Circuit Quantization	41
3.2.2	Cooper-pair Box	42
3.2.3	Dipolar coupling	43
3.2.4	Transmon	48
3.2.5	Dispersive Regime	52
3.2.6	Coherent Drive	53
3.3	Black-box Quantization	54
3.3.1	Two coupled LC Resonators	54
3.3.2	HFSS Solution	55
3.3.3	Far detuned cavity modes	59
3.3.4	Purcell Decay	59
<b>4</b>	<b>Experimental Techniques</b>	<b>62</b>
4.1	Resonator Fabrication	63
4.1.1	Coplanar waveguide	63
4.1.2	3D Resonators	64
4.1.3	Qubit Fabrication	65
4.2	Experimental Setup	66
4.2.1	Reflective Attenuation	66
4.2.2	Absorptive Attenuation	69
4.3	Sample Holder and 3D Cavity	71
4.3.1	Octobox	71
4.3.2	Rectangular waveguide cavity	72
4.4	Pulse Generation	75
4.5	Measurement	77
<b>5</b>	<b>Spins</b>	<b>78</b>
5.1	Sensitivity	80
5.2	ESR of DPPH	84
5.3	ESR of Diamond	89
5.4	ESR of Ruby	93
5.5	Considerations for Future Work	96
5.6	Outlook	99
<b>6</b>	<b>3D Transmon</b>	<b>102</b>
6.1	Design	103
6.1.1	Cavity	103
6.1.2	Qubit	105
6.2	Measurements	107
6.2.1	Cavity Nonlinearity	108
6.2.2	Readout	109
6.2.3	Saturation spectroscopy	109

6.2.4	Rabi Experiments	111
6.2.5	Coherence Measurements	114
6.2.6	Pulsed cavity experiments	115
6.2.7	Qubit Anharmonicity and Excited State Population	116
6.2.8	Temperature dependence	117
6.3	Devices	119
6.3.1	Qubit S (SQUID)	121
6.3.2	Qubits J <sub>1</sub> , J <sub>2</sub> , J <sub>3</sub>	122
6.3.3	Qubits J <sub>4</sub> , J <sub>5</sub> , and J <sub>6</sub>	123
6.3.4	D <sub>1</sub> , D <sub>2</sub> , and D <sub>3</sub>	124
6.3.5	Qubits SP <sub>1</sub> , SP <sub>2</sub> , and cQED <sub>457</sub>	124
<b>7</b>	<b>Introduction to Dephasing</b>	<b>126</b>
7.1	Dephasing	126
7.2	Gaussian Noise	127
7.3	Random Telegraph Noise	129
7.3.1	Exact solution	130
7.4	Mechanisms of Dephasing	131
7.4.1	Charge Noise	131
7.4.2	Critical Current Noise	133
7.4.3	Photon Induced Dephasing	135
<b>8</b>	<b>Photon Induced Dephasing</b>	<b>137</b>
8.1	Strong Photon-Induced Dephasing	138
8.2	Photon Injection	140
8.3	Temperature Dependence	145
8.4	Generalization	147
<b>9</b>	<b>Conclusions and Outlook</b>	<b>153</b>
9.1	Expanded Hamiltonians	153
9.2	Conclusive Dissipation	154
9.3	New experiments and hybrid systems	155
	<b>Bibliography</b>	<b>158</b>
	<b>Appendices</b>	<b>170</b>
<b>A</b>	<b>Input-Output Theory of Transmission</b>	<b>170</b>
<b>B</b>	<b>ESR of Substrates</b>	<b>172</b>
<b>C</b>	<b>Ramsey Incoherent Response</b>	<b>174</b>

CONTENTS

vii

**Copyright Permissions**

**178**

---

## List of Figures

---

<b>1</b>	<b>Introduction</b>	
1.1	Exponential coherence increase . . . . .	16
<b>2</b>	<b>Resonators and Dissipation</b>	
2.1	An LC resonator coupled to the environment . . . . .	21
2.2	Transmission line resonators . . . . .	23
2.3	Shunt resonator transmission . . . . .	25
2.4	Details of coplanar waveguide resonators . . . . .	26
2.5	Resonator quality and dimension . . . . .	29
2.6	Rectangular Cavity TE <sub>10n</sub> Modes . . . . .	30
2.7	Location of lossy dielectric surfaces . . . . .	32
2.8	Measurements of Coupling Q compared to HFSS . . . . .	37
<b>3</b>	<b>Circuit QED</b>	
3.1	Cooper-pair Box Diagram . . . . .	42
3.2	Coplanar Waveguide current and field profiles . . . . .	47
3.3	Charge Dispersion in the Transmon . . . . .	48
3.4	Jaynes-Cummings Energy Levels . . . . .	51
3.5	Circuit model of the qubit and cavity . . . . .	55
3.6	HFSS Simulation of the qubit . . . . .	56
3.7	Thermal baths connected to a resonator . . . . .	61
<b>4</b>	<b>Experimental Techniques</b>	
4.1	Spins block diagram . . . . .	64
4.2	SEM image of Josephson junction . . . . .	65
4.3	Block diagram of qubit experiments . . . . .	67

4.4	Reflective attenuation . . . . .	68
4.5	Eccosorb filter housing and performance . . . . .	69
4.6	Sample holder construction and transmission . . . . .	71
4.7	Rectangular cavity transmission . . . . .	72
4.8	Fridge base plate configuration . . . . .	73
4.9	Coupling Q Measurement in Reflection . . . . .	74
4.10	Block diagram of microwave components . . . . .	76
4.11	Properties of mixed up RF noise . . . . .	76
<b>5</b>	<b>Spins</b>	
5.1	Spins block diagram . . . . .	79
5.2	An ESR spectrum of diamond . . . . .	81
5.3	Millikelvin ESR of DPPH on a chip . . . . .	86
5.4	Picture of the DPPH Chip . . . . .	87
5.5	Anti-crossings between DPPH and Coplanar Waveguide Resonators . . . . .	88
5.6	A nitrogen doped diamond placed on a Coplanar Waveguide chip . . . . .	89
5.7	Anti-crossing of diamond P1 centers with coplanar resonators . . . . .	90
5.8	Observing field localization in CPW resonators . . . . .	91
5.9	Saturation of a diamond spin ensemble . . . . .	92
5.10	P1 center anti-crossings with CPW resonators and the return of polarization . . . . .	92
5.11	The symmetries and energy levels of sapphire and ruby in ESR . . . . .	93
5.12	Issues of coupling strength and energy levels in ruby . . . . .	94
5.13	The transitions of ruby at millikelvin temperatures . . . . .	96
5.14	Dipolar broadening limits to spin linewidth . . . . .	97
5.15	Magnet field homogeneity . . . . .	98
5.16	Coplanar waveguide resonator quality factors in a magnetic field . . . . .	99
<b>6</b>	<b>3D Transmon</b>	
6.1	Cavity Drawing . . . . .	103
6.2	Cavity dissipation and wafer issues . . . . .	104
6.3	Charging energy of qubit pads . . . . .	106
6.4	Junction Resistance and Qubit Frequency . . . . .	107
6.5	The non-linear cavity . . . . .	108
6.6	Incremental high power readout fidelity . . . . .	110
6.7	Cavity spectroscopy . . . . .	111
6.8	Cavity sidebands . . . . .	112
6.9	Fluctuations of power Rabi experiments . . . . .	113
6.10	Coherence measurements . . . . .	114
6.11	Cavity decay details . . . . .	115
6.12	Measurement of qubit steady-state excitation . . . . .	117
6.13	Temperature response of qubit . . . . .	118
6.14	Tunable Qubit S . . . . .	121

<b>7</b>	<b>Introduction to Dephasing</b>	
7.1	Gaussian noise from a TLS . . . . .	129
7.2	Critical current fluctuations . . . . .	133
<b>8</b>	<b>Photon Induced Dephasing</b>	
8.1	Qubit spectroscopy showing photon number splitting . . . . .	139
8.2	Power Rabi measurement of a cavity thermal state . . . . .	141
8.3	Qubit dephasing due to photon noise . . . . .	143
8.4	Decoherence due to thermal photons . . . . .	146
8.5	Decoherence due to noise on weakly couple modes . . . . .	148
8.6	The global maximum in dephasing with respect to coupling quality factor . . . . .	149
8.7	Improvements with proper heatsinking and filtering . . . . .	150
8.8	Cavity ground state measurement . . . . .	151
<b>9</b>	<b>Conclusions and Outlook</b>	
9.1	Thesis abstract . . . . .	157
B.1	Oxford ESR of our common substrates . . . . .	173
C.1	A set of Ramsey experiments . . . . .	175

*for my parents*

---

## Acknowledgements

---

**M**Y physics Ph.D. owes the most to my parents HOWARD and LYNNE SEARS. I would also like to thank my labmates, LUIGI FRUNZIO, and my advisor ROB SCHOELKOPF.

---

## Publication list

---

This thesis is based in part on the following published articles:

1. A. P. Sears, A. Petrenko, G. Catelani, L. Sun, H. Paik, G. Kirchmair, L. Frunzio, L. I. Glazman, S. M. Girvin, and R. J. Schoelkopf, “Photon shot noise dephasing in the strong-dispersive limit of circuit QED,” *Physical Review B* **86**, 180504 (2012).
2. H. Paik, D. Schuster, L. Bishop, G. Kirchmair, G. Catelani, A. Sears, B. Johnson, M. Reagor, L. Frunzio, L. Glazman, S. Girvin, M. Devoret, and R. Schoelkopf, “Observation of high coherence in josephson junction qubits measured in a three-dimensional circuit QED architecture,” *Phys. Rev. Lett.* **107**, 240501 (2011).
3. D. Schuster, A. Sears, E. Ginossar, L. DiCarlo, L. Frunzio, J. Morton, H. Wu, G. Briggs, B. Buckley, D. Awschalom, and R. Schoelkopf, “High-cooperativity coupling of electron-spin ensembles to superconducting cavities,” *Phys. Rev. Lett.* **105**, 140501 (2010).

# CHAPTER 1

---

## Introduction

---

**T**HE Quantum mechanics has its roots in the explanation of several technical problems [1,2] in physics; it was developed a century ago and is quite possibly the most successful scientific theory in history. Its canonical system is the hydrogen atom [3], which provides an exquisite study in quantization and interaction of light and matter. Its spectrum has components calculated to a precision of better than a part per million [4]. One may ask about its broader application to larger systems: is it a useful theory for objects as large as a thimble or tea kettle? As the description of a system grows in size the quantum nature quickly disappears, scattered by bits of dissipation and ultimately it behaves classically. Today, researchers in the field of quantum information and quantum computation are developing larger and more controllable quantum systems, motivated not simply by technical questions but to provide revelations about information [5], probabilities, and the limits of the knowable [6].

The miniaturization of transistors and accompanying expansion of computing has been a great boon to the modern era, changing nearly every part of civilization. Moore's Law is the exponential increase in computer chip transistor density, both enhancing device operation and depressing costs. But physical limits make it conceivable that within the next decade this growth may not continue, when gate sizes reach atomic dimensions. Rather than compete in size and density, quantum computers are intended to transcend the capabilities of classical computers. They may allow reduction of complicated intractable problems to ones solvable

with more reasonable requirements. Richard Feynman discussed [7] the problem of simulating quantum Hamiltonians, which must keep track of not just 0's and 1's, but superpositions of them as well. These can create entangled parts that are correlated with each other, even if individual measurements produce random results. A true quantum information processor will preserve these superpositions, allowing coherent interference using quantum logical gates before a readout step which summarizes the parallel processing performed by the superpositions. The extremely large solution space makes similar computation using a classical computer with  $2^N$  bits intractable. However, its power makes moderate growth in quantum computing a reasonable alternative to keeping up with the pace of Moore's law.

Specific interest in quantum computing was sparked with the publication of Peter Shor's number factorization algorithm [8]. The difficulty of reducing a number to its prime factorization is the basis of one of the most common encryption schemes, RSA public-key cryptography [9], and the successful implementation of Shor's algorithm would release a treasure trove of information locked up by mathematics. While the most visible example of the power of quantum computers, it is not the only one, and there may be ways to leverage quantum mechanics in engineered systems differently. Fantastic protocols exist that allow secret or encrypted communication [10], money impossible to counterfeit [11], and the fast search of information databases [12].

However, this thesis is not about carrying out these wondrous possibilities using a quantum computer, nor even the construction of a suitable device; instead it is an investigation into several strategies for creating useful quantum bits (qubits) from microscopic systems that are more naturally decoupled from the environment. In fact great progress has been made already using exotic systems, building larger quantum information processors to ensure quantum coherence remains in the final configuration. The building block of a qubit is the electron and its dipole interaction with the electromagnetic field, forming a nominally a two-level ( $\uparrow$  or  $\downarrow$ ) microscopic system. Quantum dots, which rely on single electrons with very weak magnetic dipole moment [13], are naturally decoupled from the environment to the point where strong enough radio-frequency pulses become infeasible due to cryogenic restrictions. Other electron spins come naturally connected to even weaker systems: nuclear spins [14]. Trapped ions [15] and some solid-state electron spins such as NV-centers in diamond may have a large optical moment [16] that allows manipulation with fast pulses of light, while retaining low rates of dissipation unrivaled by other systems. Alternatively, the electric dipole of a spin may be enhanced, such as with the Rydberg atom [17] where it has been enlarged to

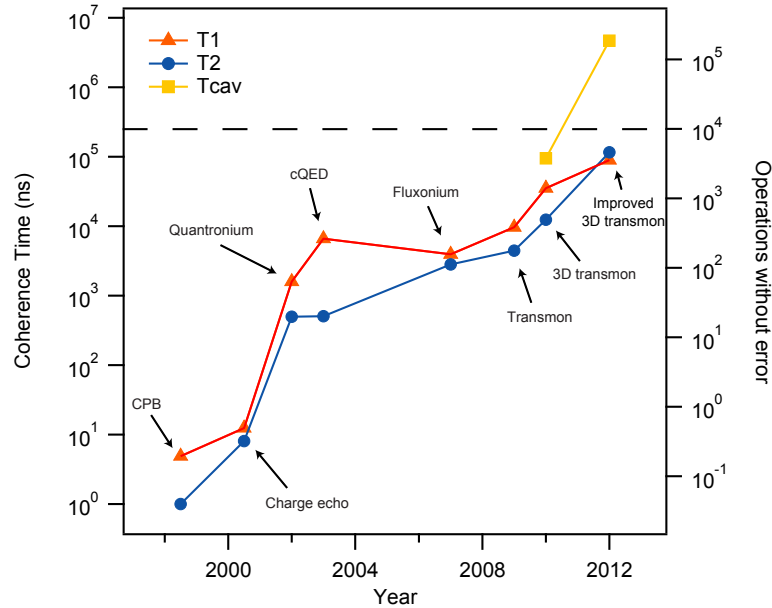


**Figure 1.1:** Schoelkopf’s Law: the coherence of superconducting qubits has increased an order of magnitude every 3 years. State-of-the-art devices are nearly at the threshold of  $10^4$  operations per error.

a thousand times that of the basic atomic unit, permitting interesting experiments with a resonant cavity.

The Schoelkopf and Devoret labs at Yale specialize in artificial atoms made from superconducting circuits, a field that has made tremendous progress. In the superconducting transmon qubit [18], for example, the electric dipole moment is a product of fabrication parameters, and strong enough to demonstrate already proofs of concept for many of the major requirements of a quantum computer. Many have been coupled together [19], with interactions mediated by a quantum bus, and readout techniques have steadily improved [20]. More generalized evaluations of quantum gates have been developed, suitable for extension to larger combinations of qubits. There are several proposed schemes to scale these ideas for larger projects in quantum information processing.

In parallel with this push for complexity, there has been increased attention put towards eliminating or understanding the decoherence in superconducting devices. The first task after assembling a collection of quantum bits is to ensure that each qubit retains its individual coherence, immune from decay and dephasing. It must be able to keep its own “time”, and in addition, in any difference frequency (when it is paired with any other spin) is constant. More fundamentally, it must store its energy in lossless media such as vacuum, high quality

crystals, Cooper-pair supercurrents, or Josephson junctions. Superconducting devices are robust due to the frictionless flow of superconductivity and the dissipationless Josephson effect [21]. As our understanding of remaining loss mechanisms has grown over the years (see Fig. 1.1), coherence times have increased several orders of magnitude. A qubit must retain its information without fail during read, write, wait, and other usage, and superconducting qubits are approaching a ratio of gate duration to coherence time that should allow an error rate of  $\sim 10^{-4}$  necessary to implement error correction procedures, creating a persistent logical bit or further extending its usefulness at the expense of complexity.

Reaching this threshold is a tough bill for any hardware to satisfy, as the requisite isolation can be tough to engineer alongside the ability to precisely control qubit interferences. In particular, at least one part of the quantum computer must be strongly coupled to the outside world for state readout, which must ideally be fast and accurate. Superconducting circuits achieve this in part by using microwave tones whose strength can be controlled over ten orders of magnitude, leaving only the residual cryogenic temperature as the main source of unintended measurement photons. Both trapped ions and solid-state systems like diamond NV-centers achieve the same effect using lasers, and enabling this sort of dynamic range is a large portion of what makes one particular exotic physical system a good platform for quantum computing. Future progress may require the combination of these systems in hybrid configurations; this is already being attempted [22–24]. While the ultimate goal requires stringing together devices in a scalable way that combines coherence with entanglement, communication, feedback, and readout, there is much to be learned from simplification as well; in fact, the first experiments with the 3D transmon, the focus for the second half of this thesis, are an example of what can be learned by removing as many distractions as possible.

## 1.1 Thesis Organization

This thesis covers the implementation of several new ideas in circuit QED for the purpose of increasing coherence times in superconducting qubits. I first review classic results from the field of high quality microwave resonators. Ch. 2 discusses the theory of lumped element circuit representation of a harmonic oscillator and the various locations and materials that store and dissipate energy. Power coupling out of a resonator is particularly important, and the ability to tune this property *in situ* is a useful feature for experiments. In fact, this is used in chapter 8 to investigate the dominant source of dephasing in a newly implemented superconducting qubit design.

Ch. 3 outlines the physics of coupling electric and magnetic dipoles to an electromagnetic cavity mode, explaining the difficulty of matching the interaction strength of electric dipoles using magnetic dipoles. The equivalence of coupling to reasonably sized three-dimensional (3D) cavities motivates the construction of a classic superconducting transmon device in a 3D resonator. The new architecture motivates a closer examination of the qubit Hamiltonian, and a brief consideration of the new environment presented by a cavity with many modes.

In Ch. 4, I describe the fabrication procedure for planar resonators on sapphire and ruby substrates, as well as the traditional Dolan-bridge recipe used for the 3D transmon. I will also detail the extra filtering used to correct thermalization issues and obtain the best qubit coherence times, the first mechanically adjustable coupler for the 3D cavities, and experimental details for the artificial heat bath generated for chapter 8.

Ch. 5 begins with the coupling an ensemble of simple organic spins to a superconducting resonator as a proof of concept. This verifies several bits of physics known but untested in our lab: that superconducting films may have high quality factors even with large magnetic fields applied in parallel, and that strong coupling is achievable using large numbers of magnetic spins in an ensemble. After this, we use more exotic spins such as nitrogen substitutions in diamond and observe the hyperfine splitting with carbon-13, before demonstrating low-field resonance by utilizing the zero-field-splitting in ruby and obtaining gorgeous broadband spectra. We conclude that the true promise of hybrid spin systems may lie in low-number isotopically enriched samples.

In Ch. 6 we return to superconducting devices and try a radically simple architecture for the transmon, placing a standard device on a sapphire chip inside a much larger rectangular waveguide cavity. This removes all non-qubit lithography and makes the device “wireless” without wirebonds, circuit boards, or solder. The resulting 10x increase in energy decay times broke coherence records for superconducting devices and quickly became the most popular superconducting qubit design in experiments across the world.

The increased coherence interestingly exposed the entanglement of the qubit with several fluctuating parts of the system: trapped charges, Josephson junction conduction channels, and errant cavity photons. The effect of these fluctuations is summarized in Ch. 7. The 3D transmon was designed with the same classic parameters as the planar transmon, but the lengthened timescale of dephasing and decay revealed sensitivities to correspondingly weaker fluctuations. We pick one of them to study in the final experimental chapter.

The first 3D transmons were placed in high-Q cavities to prevent rapid energy decay from the Purcell effect. Their improved coherence times in combination with this design choice

meant that a single cavity transit of a microwave photon would completely dephase the qubit. In Ch. 8, I explore this by changing both the rate and number of photons in the exterior mode, by raising the fridge temperature, and by adding extra filtering to eliminate this effect.

The thesis ends in Ch. 9 with some final thoughts about coherence.

## CHAPTER 2

---

### Resonators and Dissipation

---

**I**N circuit quantum electrodynamics (circuit QED) quantum devices are often protected from dissipation and decoherence by microwave resonators. They shield outside interference, inhibit spontaneous emission, and often share locations of energy storage and loss with their embedded qubits. In fact, we know resonators of different geometries have a different distribution of energy among bulk dielectrics, surface dielectrics, and conductors. Conscious engineering to place the majority of this energy in a lossless or high quality material has the potential to improve useful qubit lifetimes substantially; alternatively, concentrating it in small volumes may allow us to magnify interactions with isolated devices.

In this chapter we first define the quality factor for an ideal electromagnetic resonator, then broaden the definition in the presence of a dissipative environment. We give a crucial relation that defines the resonator quality factor while accounting for storage and dissipation of energy in its different parts. Then, we study two physical geometries for resonators used in experiment later in this work: planar and three-dimensional cavities. In considering their respective mechanisms of dissipation, we evaluate their suitability for embedded, simple lumped devices within these cavities in Ch. 3.

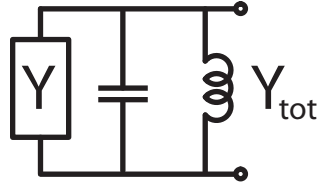


**Figure 2.1:** A parallel resonator with some connection to the environment will have a finite quality factor

## 2.1 Circuit Resonators

Energy storage in an oscillator can be defined through a description of admittance  $Y = \tilde{I}/\tilde{V}$  with the time-dependent phasors  $\tilde{V} = |V|e^{j\phi_V}$  and  $\tilde{I} = |I|e^{j\phi_I}$  and initial phases  $\phi_V$  and  $\phi_I$ , which give the current and voltage across the oscillator  $I(t) = \Re[\tilde{I}e^{j\omega t}]$  and  $V(t) = \Re[\tilde{V}e^{j\omega t}]$ . When composed of an inductor  $L$  and a capacitor  $C$ , it has resonant frequency  $\omega_0 = 1/\sqrt{LC}$ , and stores a constant total energy  $U = U_e + U_m = \frac{1}{2}CV(t)^2 + \frac{1}{2}LI(t)^2$ , of which the time-averaged capacitive and inductive energies are:

$$U_e = \frac{1}{2}C\langle V(t)^2 \rangle = \frac{1}{4}C \cdot \Re[\tilde{V}\tilde{V}^*] \quad (2.1)$$

$$= \frac{1}{4}C|V|^2 \quad (2.2)$$

and

$$U_m = \frac{1}{2}L\langle I(t)^2 \rangle = \frac{1}{4}L \cdot \Re[\tilde{I}\tilde{I}^*] \quad (2.3)$$

$$= \frac{1}{4}L|I|^2 \quad (2.4)$$

$$= \frac{1}{4}|V|^2 \frac{1}{\omega^2 L} \quad (2.5)$$

When a dissipative element is added, the device has a quality factor defined by the ratio of energy storage to dissipation per cycle:

$$Q = \frac{\omega U}{P_{\text{diss}}} \quad (2.6)$$

where  $P_{\text{diss}}$  is the time-averaged rate of dissipation. More generally we add an admittance  $Y = G + iX$  connected in parallel (see Fig. 2.1); then clearly for a purely resistive shunt  $Y = G$

giving time-averaged dissipation  $P_{\text{diss}} = \frac{1}{2}G|V|^2$  we have

$$Q = \frac{1}{2} \frac{\Im \left[ j\omega \left( C + \frac{1}{\omega^2 L} \right) \right] |V|^2}{\Re [G] |V|^2} \quad (2.7)$$

and in fact more generally for total admittance  $Y_{\text{tot}}$  we have

$$Q = \frac{1}{2} \frac{\Im [Y_{\text{tot}}]}{\Re [Y_{\text{tot}}]} \quad (2.8)$$

for total admittance  $Y_{\text{tot}}$ . For a circuit the characteristic energy decay time  $\tau$  is related to the quality factor by  $Q = \omega\tau$ .

### 2.1.1 Participation Ratio

Understanding and localizing dissipation (and noting the attendant Joule heating) is important for increasing the coherence times of quantum devices. The concept of participation ratio is convenient for keeping an account of the effect of specific materials and processes on the total quality factor of a device. Of the total energy stored in a device, a fraction  $p_i$  is stored in volume  $i$ , subject to a decay process at rate  $\gamma_i$  which would limit the device to a quality factor  $Q_i$  if 100% of the stored energy were subject to it. The rate of total energy loss is  $\gamma = \sum_i p_i \gamma_i$  and the total quality factor is:

$$\frac{1}{Q} = \sum_i \frac{p_i}{Q_i} \quad (2.9)$$

In the remainder of the chapter, we examine two geometries for resonators with particular interest in their mechanisms for dissipation and the participation ratio of each process.

## 2.2 Transmission Line Resonators

Transmission lines are long microwave structures with a cross-section small in the transverse direction (relative to the signal wavelength at frequencies of interest), giving them a capacitance and inductance per unit length which can be determined by electrostatic integrals and precisely controlled by photolithography. Their geometry determines a capacitance and inductance per unit length,  $C_l$  and  $L_l$  of order  $\epsilon_0$  and  $\mu_0$ , and may be calculated through field integrals. They realize a device with a characteristic impedance  $Z_0 = \sqrt{\frac{L_l}{C_l}}$  which can be different from vacuum, even without the use of any dielectric material, and wavenumber

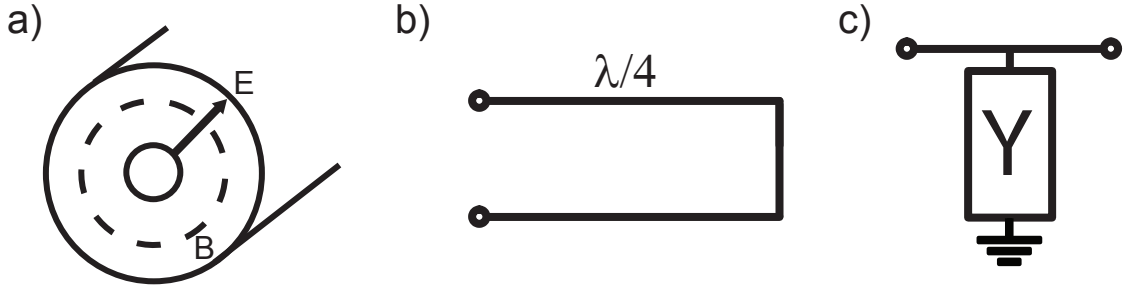


**Figure 2.2:** a) Integrals of the field  $\vec{E}$  and  $\vec{B}$  field lines of a transmission line define the capacitance  $C_l$  and inductance  $L_l$  per unit length. b) A  $\lambda/4$  length of line, shorted at the end, forms a transmission line resonator. c) Arrangement of such a resonator as a shunt allows the simultaneous testing and use of many resonators.

$\beta = \omega\sqrt{L_l C_l}$ . Voltage waves propagate  $V(z, t) \exp(\gamma t)$  with propagation factor  $\gamma = \alpha + i\beta$ , where  $\alpha$  is the amplitude attenuation per unit length.

When electromagnetic waves impinge upon a load with impedance different from the characteristic impedance of the transmission line  $Z_0$ , reflections are created; when loaded on both sides, multiple reflections produce standing waves which collect electromagnetic energy. This creates a  $\lambda/2$  resonator (for the fundamental mode) with both ends open, and a  $\lambda/4$  resonator (for the fundamental mode) with one end shorted.

### 2.2.1 Quarter-wave Resonators

For a line of length  $l$  with load  $Z_L$ , the input impedance is: (Pozar p274):

$$Z_{in} = Z_0 \frac{Z_L + Z_0 \tanh \gamma l}{Z_0 + Z_L \tanh \gamma l} \quad (2.10)$$

Choosing a microwave short  $Z_L = 0$  creates a resonance when  $l \approx \lambda/4$  with additional harmonics at  $(2n+1)\omega_0$  of the fundamental. Following Pozar, a  $\lambda/4$  resonator has impedance:

$$Z_{in}^{sh} = Z_0 \tanh(\gamma l) = Z_0 \frac{1 - j \tanh \alpha l \cot \beta l}{\tanh \alpha l - j \cot \beta l} \quad (2.11)$$

whose resonance at  $\omega_0$  we can expand about  $\beta l = (2n+1)\frac{\pi}{2}$ :

$$\beta l = \frac{[(2n+1)\omega_0 + \Delta\omega] l}{v} = (2n+1)\frac{\pi}{2} + \frac{\pi}{2}\delta x \quad (2.12)$$

where  $\delta x = (\omega - \omega_0)/\omega_0$ . For small loss  $\tanh \alpha l \approx \alpha l$ , and we approximate:

$$Z_{in}^{sh} \approx \frac{Z_0}{\alpha l + j\frac{\pi}{2}\delta x} \quad (2.13)$$

$$= \frac{Z_0/\alpha l}{1 + 2j\frac{(2n+1)\pi}{4\alpha l}\delta x_n} \quad (2.14)$$

where  $\delta x_n = (\omega - \omega_n)/\omega_n$ .

This has an equivalent parallel circuit which is:

$$R_n = \frac{Z_0}{\alpha l} \quad (2.15)$$

$$C_n = \frac{\pi}{4\omega_0 Z_0} \quad (2.16)$$

$$L_n = \frac{4Z_0}{(2n+1)^2\omega_0\pi} \quad (2.17)$$

with characteristic impedance and internal quality factor:

$$Z_n = \frac{4Z_0}{(2n+1)\pi} \quad (2.18)$$

$$Q_n = \frac{(2n+1)\pi}{4\alpha l} \quad (2.19)$$

### Resonator Coupling

Furthermore, following [25], we can limit the coupling of this resonator to the port or feedline by adding a capacitor in series that serves as an impedance mismatch or mirror. The Norton equivalent transformation of this capacitor places in parallel:

$$Y_k = \frac{j\omega C_\kappa}{1 + j\omega C_\kappa Z_{port}} = \frac{j\omega C_\kappa + q_{in}^2/Z_{port}}{1 + q_{in}^2} \quad (2.20)$$

where  $q_{in} = \omega C_\kappa Z_{port}$  and  $Z_{port}$  is the impedance of the input port.

For small  $q_{in}$ , this slightly reduces the resonant frequency (which we neglect for  $Q \gg 1$ ) and gives it a coupling quality factor:

$$Q_c = \frac{1}{Z_n \Re[Y_k]} = \frac{1}{q_{in}^2} \frac{Z_{port}}{Z_n} \quad (2.21)$$

$$= \frac{\pi}{4(2n+1)} \frac{1}{\omega_0^2 C_\kappa^2 Z_0 Z_{port}} \quad (2.22)$$

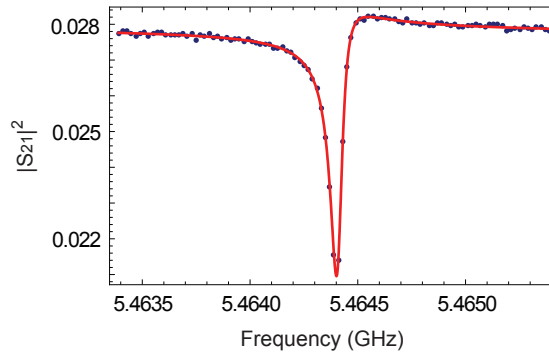


**Figure 2.3:** The transmission of a coupled  $\lambda/4$  shunt resonator with  $Q_c = 650,000$  and  $Q_i = 80,000$ .

which combines in parallel with the intrinsic quality  $Q_n$  from Eqn. 2.15 to give:

$$1/Q = 1/Q_n + 1/Q_c \quad (2.23)$$

### Power Absorption

A coupled  $\lambda/4$  resonator can be useful to deliver power to a localized area using small bandwidth; it modifies the transmission between two ports by partially absorbing and reflecting power (following [26]) where:

$$|S_{21}|^2 = \frac{S_{21}^{\min} + 4Q^2\delta x^2}{1 + 4iQ\delta x^2} \quad (2.24)$$

$$S_{21}^{\min} = \frac{Q_c}{Q_i + Q_c} \quad (2.25)$$

and the power dissipated in the resonator is

$$P_{\text{abs}} = P_{\text{in}}(1 - S_{21}^{\min}) \quad (2.26)$$

In practice (see Fig. 2.3), the transmission can be modified by cabling or components other than the device under test. Often in measurements of shunt admittances, we will be interested in the natural frequency  $\omega/2\pi$  of a shunt resonator, and its quality factor due to the coupling out of power as well as power dissipated internally. On occasions when Eqn. 2.2.1 is insufficient,

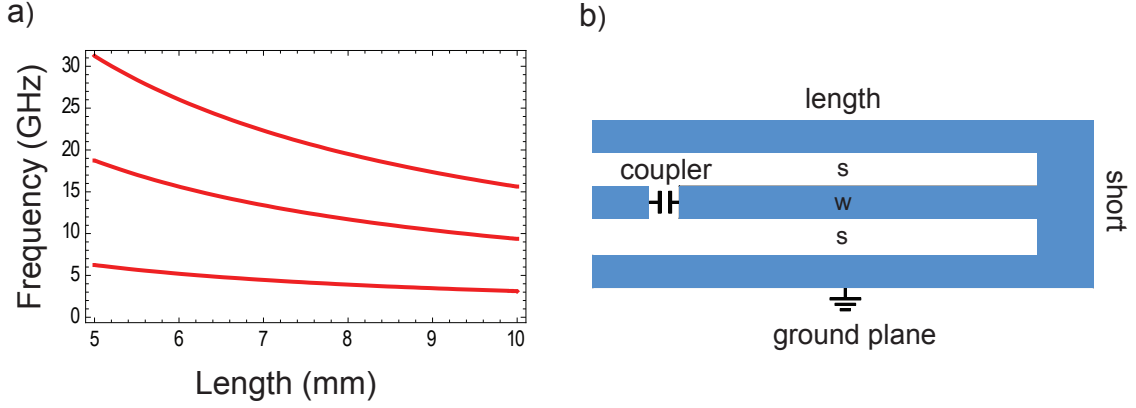


**Figure 2.4:** a) Approximate frequency of  $\lambda/4$  resonator higher resonances, given shunt length, for  $w = 10$  nm,  $s = 5$  nm a) A schematic of a capacitively coupled length of coplanar waveguide, including gaps  $s$  and centerpin width  $w$ .

we will use a formula that assumes a 2-port device with only a single pole and dissipation only provided by the resonator, but with the possibility of nearby reflections [? ], accounted for by the complex  $\tilde{Q}_c$ .

$$S_{21} = T_{\max} \left[ \frac{-\tilde{Q}_c(Q_i \delta x - i)}{iQ_i - \tilde{Q}_c(2Q_i \delta x - i)} \right] \quad (2.27)$$

$$= T_{\max} \left[ 1 - \frac{iQ_i}{iQ_i - \tilde{Q}_c(2Q_i \delta x - i)} \right] \quad (2.28)$$

for  $\delta x = (\omega - \omega_0)/\omega$ ,  $\omega_0$  the frequency of the resonator (loaded only by  $Q_i$ ). Then the true coupling quality factor quantifying power loss is  $1/Q_c = \Re[1/\tilde{Q}_c]$ .

## 2.2.2 Coplanar Waveguide

A coplanar waveguide (CPW) is the 2D analog of a coaxial transmission line. In fact it is easy to fabricate, and readily assembled into an array of shunt resonators for many useful purposes. Their properties and design tradeoffs have been reviewed in depth in several recent publications [25, 27]. Its capacitance and inductance per unit length are given by:

$$L_l = \frac{\mu_0 K(k'_0)}{4 K(k_0)} \quad (2.29)$$

$$C_l = 4\epsilon_0 \epsilon_{\text{eff}} \frac{K(k'_0)}{K(k_0)} \quad (2.30)$$

where  $K$  is the complete elliptic integral of the first kind with arguments combining the center strip width  $w$  and gaps  $s$ , and the effective dielectric constant  $\epsilon_{\text{eff}}$  and:

$$k_0 = \frac{w}{w + 2s} \quad (2.31)$$

$$k'_0 = \sqrt{1 - k_0^2} \quad (2.32)$$

This allows us to compute the characteristic impedance  $Z_0 = \sqrt{L_l C_l}$  and lengths necessary for practical resonators. The frequency and  $Q_c$  of a device can easily be controlled with the resolution of achievable photolithography.

### Kinetic Inductance

Because of the geometry in thin film coplanar waveguides, there is the potential for a large fraction of the resonator inductance to come from the kinetic energy stored in the charge carriers. A length of CPW has a total capacitance  $C = C_l l$  and  $L = L_m + L_k$ , the sum of magnetic inductance  $L_m = L_l l$  (noted above) and a kinetic inductance  $L_k$ . These determine the resonant frequency  $\omega_0 = 1/\sqrt{LC}$ . Following [25] the kinetic energy of a supercurrent is

$$U_{\text{kin}} = \int \frac{1}{2} n_s m v^2 dV \quad (2.33)$$

$$= \frac{1}{2} \frac{n_s m}{A e^2} I^2 \quad (2.34)$$

$$= \frac{1}{2} \mu \lambda_L^2 \frac{l}{A} I^2 \quad (2.35)$$

for an area  $A = wt$ , using  $\lambda_L = \sqrt{\mu m / n_s e^2}$  the London penetration depth, and yielding a total kinetic inductance which is

$$L_k = \mu \frac{\lambda_L^2}{wt} g(s, w, t) \quad (2.36)$$

where  $g(s, w, t)$  depends upon the CPW centerpin and spacing widths and film thickness [28]; for our devices it is of order unity, and as an example with our standard choices for dimensions and geometry ( $w = 10 \mu\text{m}$ ,  $s = 5 \mu\text{m}$ , sapphire thickness  $450 \mu\text{m}$ ), niobium film ( $\lambda_L = 40 \text{ nm}$ ) resonators have  $L_k \sim 1 \text{ nH/m}$  whereas  $L_m = \mu_0 l$  is  $1 \text{ nH/mm}$ .

The kinetic inductance can be modified *in situ* by the application of a magnetic field in

parallel with the superconducting film such that:

$$L_k(B) = \frac{L_k(0)}{1 - \left(\frac{B}{B_c}\right)^2} \quad (2.37)$$

Here the quadratic functional form is suggested by non-linearities in the London Equations, caused by pair breaking in response to increased current [29]. Then the frequency of the resonator depends on magnetic field:

$$\omega(B) = \frac{\omega_0}{\sqrt{1 + \alpha \frac{B_c^2}{B_c^2 - B^2}}} \quad (2.38)$$

where we define the geometric kinetic inductance fraction:

$$\alpha = L_k(0)/L_m \quad (2.39)$$

which captures the sensitivity of the device to fluctuations in quasiparticles and stray magnetic fields. For our resonators, the kinetic inductance fraction is small, on the order of  $10^{-3}$ , making us relatively insensitive to poor quality films. However other researchers have leveraged kinetic inductance for interesting applications such as wideband parametric amplifiers [30] or photon detection through quasiparticle sensing [31].

### Dielectric losses

Coplanar waveguide stores much of its field in the bulk substrate and a large portion in surface materials. The half-plane substrate is often of high- $\epsilon$  silicon or sapphire; this is accounted for in resonators through the  $\epsilon_{\text{eff}}$ , where for sapphire  $\epsilon = 10.5$  and in practice on our devices  $\epsilon_{\text{eff}} \approx 5.2$ . We will exploit this in Ch. 5, where the substrate is doped with spins and we wish for the majority of the resonator electromagnetic energy to interact with them. In addition, this planar geometry stores much of the mode energy at the surface of the substrate, an area subject to violent electron beam currents in lithography, adsorbed water molecules, and other contaminants whose lossiness may damp the cavity quality factor.

In fact, several experimental surveys of loss in coplanar waveguides have identified the surface as the likely region which whose dissipation limits resonator quality factors [33–35], with improved results for devices with larger and wider features. It is with this in mind that we consider 3D cavities with large mode volumes that “dilute” the importance of thin dielectric films.

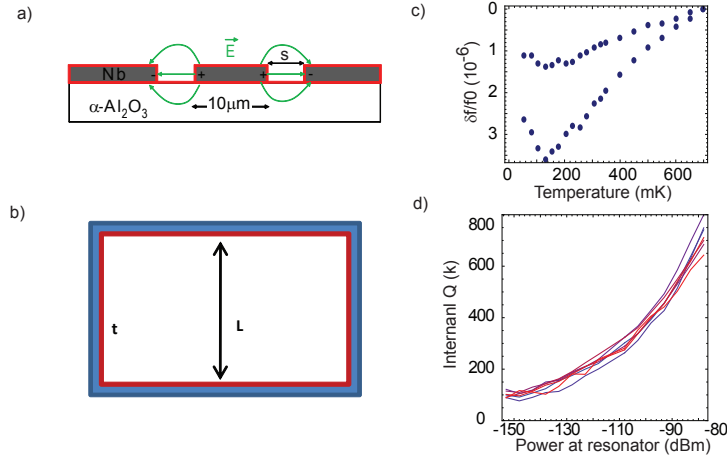


**Figure 2.5:** a) Coplanar waveguide resonators store most of their energy in the surface dielectric [32]. b) The participation of a lossy dielectric film is  $t/L$ , where for a 3D resonator whose cross-section we illustrate,  $L$  approaches  $\lambda$ . c) A layer of dielectric on the surface of CPW is predicted [33] to induce a frequency-shift in the resonator frequency as its complex dielectric constant changes with temperature. This effect varies for different center-pin width (above:  $30\mu\text{m}$ , below:  $10\mu\text{m}$ ) d) The power dependence of resonator quality factor indicates the presence of saturable two-level systems which otherwise leech energy.

## 2.3 Rectangular Cavities

Several styles of 3D resonators are well-known, including notably the pillbox cylinder, but we will study a rectangular cavity composed of or a length of rectangular waveguide shorted on both ends. It can be designed with resonant modes in the microwave frequencies, stores the majority of the electromagnetic energy in vacuum, and is readily machined.

### 2.3.1 Rectangular Waveguide

Rectangular waveguide is useful for its power transmission capability, with smaller conductor losses than other geometries due to the large wall area. For perfectly conductive walls the fields of the resonator standing modes are particularly easy to describe. Solutions to Maxwell's Equations can be divided into two families, the Transverse Electric (TE) and Transverse Magnetic (TM) modes, dependent upon which component parallel to propagation,  $H_z$  or  $E_z$ , is null throughout. Rectangular waveguide has solutions for traveling TE waves:

$$H_z = H_0 \sin\left(\frac{m\pi x}{a}\right) \sin\left(\frac{n\pi y}{b}\right) e^{-j\beta z} \quad (2.40)$$

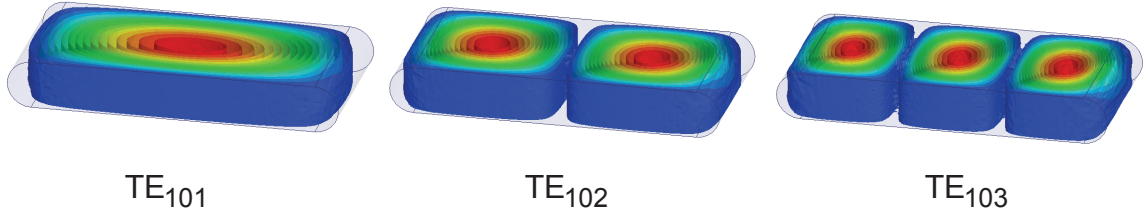


**Figure 2.6:** The lowest three resonant modes of a length of shorted rectangular waveguide

and TM waves:

$$E_z = E_0 \cos\left(\frac{m\pi x}{a}\right) \cos\left(\frac{n\pi y}{b}\right) e^{-j\beta z} \quad (2.41)$$

with

$$\gamma = \sqrt{\omega^2 \mu \epsilon - \left(\frac{m\pi}{a}\right)^2 - \left(\frac{n\pi}{b}\right)^2} \quad (2.42)$$

given a filled volume with dielectric constant  $\epsilon$  and magnetic permeability  $\mu$ , and a cutoff wavenumber which limits propagation below a certain frequency to evanescent waves

$$k_c = \sqrt{k_x^2 + k_y^2} \quad (2.43)$$

and with wavenumbers:

$$k_x = (m\pi/a), k_y = (n\pi/b), \quad k_z = (p\pi/d) \quad (2.44)$$

When bounded by conductive walls, these give standing wave solutions, similar to transmission line resonators. Fig. 2.6 displays the field magnitude for the first few  $TE_{10n}$  modes of a rectangular cavity. We can generally describe the fields of the  $TE_{mnp}$  mode with the following equations [36] for a waveguide cavity filled with the magnetic permeability  $\mu$  and electric permittivity  $\epsilon$  and of the material filling the waveguide (see Fig. 2.6):

$$E_x = jE_0 \frac{k_y}{k_c} \cos(k_x x) \sin(k_y y) \sin(k_z z) \quad (2.45)$$

$$E_y = -jE_0 \frac{k_x}{k_c} \sin(k_x x) \cos(k_y y) \sin(k_z z) \quad (2.46)$$

$$E_z = 0 \quad (2.47)$$

and

$$H_x = -H_0 \frac{k_x k_z}{k k_c} \sin(k_x x) \cos(k_y y) \cos(k_z z) \quad (2.48)$$

$$H_y = -H_0 \frac{k_y k_z}{k k_c} \cos(k_x x) \sin(k_y y) \cos(k_z z) \quad (2.49)$$

$$H_z = H_0 \frac{k_c}{k} \cos(k_x x) \cos(k_y y) \sin(k_z z) \quad (2.50)$$

with resonant frequencies:

$$\omega = \frac{1}{\sqrt{\mu \epsilon}} \sqrt{(m\pi/a)^2 + (n\pi/b)^2 + (p\pi/d)^2} \quad (2.51)$$

We have normalized these to an energy:

$$U_E = \frac{1}{8} abd \epsilon E_0^2 \quad (2.52)$$

$$U_H = \frac{1}{8} abd \mu H_0^2 \quad (2.53)$$

for  $m, n, p > 0$ , or  $\frac{1}{4} abd \epsilon E_0^2$  when an index  $m$  or  $n$  is zero.

### 2.3.2 Dielectric Loss

A vacuum-filled rectangular cavity may nevertheless have dielectric loss due to a thin layer of lossy material which is placed on the sidewalls (see Fig. 2.7). Dielectric loss at the walls for the  $TE_{101}$  consists solely of loss for  $E_y$  field, which is only nonzero at the  $x = 0, a$  walls. The complex electric energy in a dielectric layer of thickness  $t$  at the walls is:

$$U_{\text{diel}} = \frac{1}{2} \int_0^t dx \int_0^b dy \int_0^d dz [\epsilon \vec{E} \cdot \vec{E}^*]_{x=0} \quad (2.54)$$

$$= \frac{t}{2} \epsilon |E_0|^2 \int_0^b dy \int_0^d dz \left[ \sin^2 \left( \frac{\pi y}{b} \right) \sin^2 \left( \frac{\pi z}{d} \right) \right] \quad (2.55)$$

$$= \frac{t}{b} \frac{V}{8} \epsilon |E_0|^2 \quad (2.56)$$

such that the time averaged dissipation for  $\epsilon = \epsilon' + i\epsilon''$  is:

$$P_{\text{diel}} = \frac{V_\epsilon}{8} \omega \epsilon'' |E_0|^2 \quad (2.57)$$

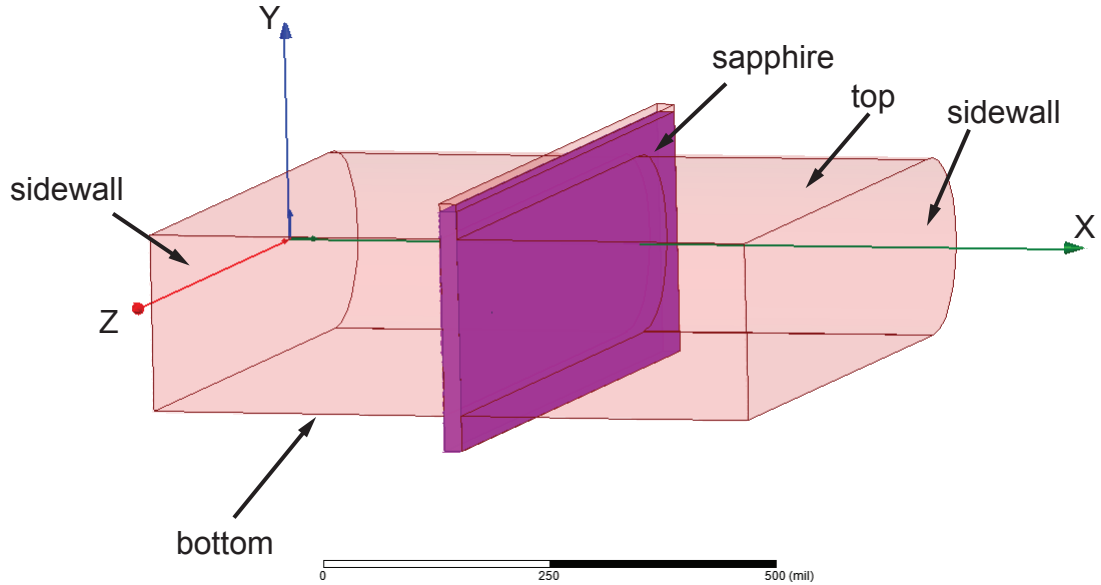


**Figure 2.7:** A cross-section of a rectangular waveguide cavity. Lossy dielectric material may cover the surface of the embedded sapphire substrate (dark purple) the top and bottom of the cavity, or the sidewalls. Substrate and sidewall surfaces share the same  $TE_{101}$  mode participation.

Because of the uniformity of the fields a substrate we place in the center of the cavity, a wafer of thickness  $t$  which stretches the full width has the same amount of dissipation. Comparing to the total electric energy:

$$W_E = \frac{1}{2} \int [\epsilon \vec{E} \cdot \vec{E}^*] dV \quad (2.58)$$

$$= \frac{V + (\epsilon_r - 1)V_\epsilon}{8} \epsilon' |E_0|^2 \quad (2.59)$$

which approximately gives a total quality factor due to the lossy dielectric proportional to its participation ratio:

$$Q_{\text{diel}} \approx \left( \epsilon_r \frac{V_\epsilon}{V} \right) / \tan \delta \quad (2.60)$$

for dielectric volume  $V_\epsilon$  and  $\tan \delta = \epsilon' / \epsilon''$ . By purposely providing a dielectric, such as the sapphire we use as a substrate for devices, a measurement of cavity Q gives a lower bound on the  $1 / \tan \delta$  or the quality factor. Our measurements indicate that bulk sapphire has at

least  $Q_{\text{sap}} \geq 1.7 \times 10^6$ . Many other lossy dielectrics or oxides, whether undiscovered or simply unavoidable, have much less importance in a 3D cavity. The added dimension of rectangular waveguides reduces the participation of surface contaminants from  $p_{\text{diel}} \approx 10^{-2} - 10^{-3}$  in CPW or striplines to  $p_{\text{diel}} \approx 10^{-6}$  or less in 3D resonators. If we are concerned about surface dielectrics, we have come to the right place.

### 2.3.3 Conductor Loss

Standing waves allowed in a rectangular waveguide resonator do not all vanish at the walls, there is some finite magnetic field tangent to them. This creates a current in the metal which dissipates energy according to its conductivity. For very good conductors, dissipation in lossy wall conductivity is proportional to  $H_{\parallel}$ , the tangent magnetic field, and to first order we can use this magnitude to estimate the dissipation due to finite conductivity with a surface current.

#### Surface Impedance

The complex average power entering a conducting surface is:

$$P_{av} = \oint_{S'} (\vec{E} \times \vec{H}^*) \quad (2.61)$$

$$= \oint_{S'} \eta |H|^2 \quad (2.62)$$

where  $\eta$  is the complex impedance of the conductor. Because transverse magnetic fields are screened and disappear rapidly inside the surface, this is simply:

$$= \int \eta |H_{\parallel}|^2 \quad (2.63)$$

and for good conductors with conductivity  $\sigma$  or skin depth  $\delta_s$ :

$$\eta = (1 + j) \sqrt{\frac{\omega \mu}{2\sigma}} \quad (2.64)$$

$$= (1 + j) / \sigma \delta_s \quad (2.65)$$

Then, for normal metals, the extra energy effectively increases the resonator dimensions by  $\delta_s$ , and all  $Q_s = \mathcal{I}[\eta] / \mathcal{R}[\eta] = 1$  such that essentially all of the stored energy within the normal metal is dissipated each cycle. Although finite, the conductivity of copper is sufficient to

permit 3D cavities with  $Q \approx 10^4$  at millikelvin temperatures because of their small magnetic participation ratio  $\alpha$ , defined in analogy with Eqn. 2.9 through

$$Q_{\text{cond}} = \frac{\omega \mu_0 \lambda}{R_s} \frac{\int_V |H|^2 dV}{\int_S |H|^2 dA \times \lambda} \quad (2.66)$$

$$= \frac{Q_s}{\alpha} \quad (2.67)$$

where  $\lambda$  is the skin depth,  $R_s = \Re[\eta]$  is the surface resistance, and  $\alpha$  is also called the kinetic inductance fraction in superconducting resonators. As we saw with CPW, energy can be stored losslessly as a supercurrent of Cooper pairs. We described this using a complex conductivity which leads to a complex surface impedance and surface quality factor that can be greater than unity. In resonator geometries, we often combine the participation ratio of the conductive walls with the surface resistance to express the overall contribution to the quality factor:

$$Q_{\text{cond}} = \frac{\Gamma}{\Re[\eta]} \quad (2.68)$$

This  $\Gamma$  geometric factor varies by mode even for the same cavity, and is related to the kinetic inductance fraction by  $\alpha \Gamma = \omega \mu_0 \lambda$ . It can range from  $10^{-2} \Omega$  for lumped element cavities to  $\sim 10^3 \Omega$  for rectangular waveguide.

The kinetic inductance fraction for 3D cavities is very small, although its effect can be observed for temperatures near the critical temperature  $T_c$  of the superconductor. While a superconductor ideally has an infinite surface Q (or one that increases exponentially with the superconducting gap frequency), our most refined devices have  $Q_s \sim 5000$ , with improvement by using better quality aluminum and through chemical etching, and there is ongoing work both to quantify and improve this for our resonators.

### 2.3.4 Power Coupling

Because we must design a way to get power out of our resonator, we study the effect of a wire antenna inserted into an aperture of the rectangular cavity. Collin defines the solutions to the electromagnetic field inside a perfectly conducting, closed cavity [37]. Here the electric field has two orthonormal sets of field modes. The solenoidal modes satisfy the Helmholtz

Equation:

$$\nabla^2 E_n + k_n^2 E_n = 0, \text{ in the volume} \quad (2.69)$$

$$n \times E_n = 0, \text{ on the walls} \quad (2.70)$$

and there are an additional set of irrotational modes  $F_n$  defined by  $l_n F_n = \nabla \Phi_n$  using scalar function  $\Phi_n$ .

Similarly, the magnetic field inside the cavity can be expanded in terms of orthonormal magnetic modes  $H_n$  following:

$$\nabla^2 H_n + k_n^2 H_n = 0 \quad (2.71)$$

$$n \cdot H_n = 0, \text{ on the walls} \quad (2.72)$$

$$n \times \nabla \times H_n = 0, \text{ on the walls} \quad (2.73)$$

as well as a set of irrotational modes  $G_n$  defined by  $p_n G_n = \nabla \psi_n$  using scalar function  $\psi_n$ .

These modes are orthonormal as determined, for example, by:

$$\int E_n \cdot E_m dV = \delta_{nm} \quad (2.74)$$

$$\int E_n \cdot F_m dV = 0 \quad (2.75)$$

$$(2.76)$$

giving  $E_n, F_n, H_n, G_n$  the units of  $\sqrt{V}^{-1}$ . We can express the total field by:

$$\vec{E} = \sum_n e_n \vec{E}_n + f_n \vec{F}_n \quad (2.77)$$

$$\vec{H} = \sum_n h_n \vec{H}_n + g_n \vec{G}_n \quad (2.78)$$

For the TE modes of a rectangular waveguide cavity, the electric field modes are:

$$E_n = \sqrt{\frac{4}{abd}} \cdot \left( \cos \left[ \frac{n\pi x}{a} \right] \sin \left[ \frac{m\pi y}{b} \right] \sin \left[ \frac{p\pi z}{d} \right] \hat{x} + \right. \quad (2.79)$$

$$\left. \sin \left[ \frac{n\pi x}{a} \right] \cos \left[ \frac{m\pi y}{b} \right] \sin \left[ \frac{p\pi z}{d} \right] \hat{y} \right) \quad (2.80)$$

while the total electric and magnetic field energy are:

$$W_e = \frac{\epsilon}{4} \int |E|^2 dV = \frac{\epsilon}{4} \sum_n |e_n|^2 \int E_n^* \cdot E_n dV \quad (2.81)$$

$$= \frac{\epsilon}{4} \sum_n |e_n|^2 \quad (2.82)$$

and

$$W_m = \frac{\mu}{4} \int |H|^2 dV = \sum_n \frac{\mu}{4} |h_n|^2 \int H_n^* \cdot H_n dV \quad (2.83)$$

$$= \frac{\mu}{4} \sum_n |h_n|^2 \quad (2.84)$$

For a current element exciting a cavity electric orthonormal mode  $E_n$  with amplitude  $e_n$ , we find:

$$e_n = \frac{-j\omega\mu_0 \left(1 + \frac{1-j}{Q_n}\right) \int J \cdot E_n}{k_n^2 - k_0^2 \left(1 + \frac{1-j}{Q_n}\right)} \quad (2.85)$$

When driving on resonance for high Q modes this gives an average stored electric energy:

$$W_e = \frac{\epsilon}{4} \left[ \omega^2 \mu_0^2 / k_0^4 \left( \int J \cdot E_n \right)^2 \right] Q^2 \quad (2.86)$$

$$(2.87)$$

Using the approximation that there is a sinusoidal current distribution  $I(y)$ , in the wire and defining  $\bar{E}_n = E_n(x, y, z)$  the strength of the mode at the coupling probe assuming it has little variation along its short length, we derive for  $J$  the volume current density in the wire:

$$\int (J \cdot E_n) dV = \int dA \int_0^h I(y) \cdot \bar{E}_n dy \quad (2.88)$$

$$= \int_0^h I(y) \cdot \bar{E}_n dy \quad (2.89)$$

$$= \bar{E}_n \int_0^h I_0 \sin[k_0(h-y)] dy \quad (2.90)$$

$$= I_0 \bar{E}_n \left( \frac{\cos k_0 h - 1}{k_0} \right) \quad (2.91)$$

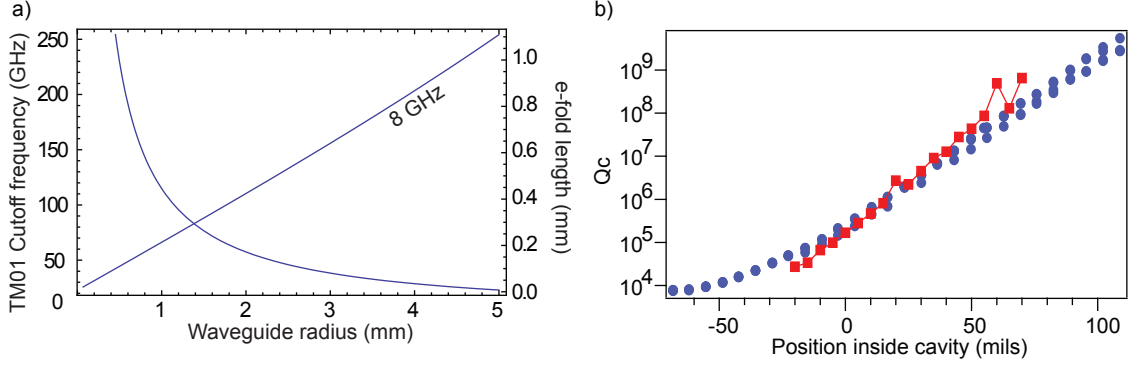


**Figure 2.8:** a) Evanescent coupling through circular waveguide with radius  $a$  has cutoff wavenumber  $2.405/a$  for  $TM_{01}$ . The increase is largely independent of frequency, but shown for 8 GHz. b) The exponential increase of evanescent  $Q_c$  as the coupler is retracted as simulated by HFSS (red) and in experiment (blue) using  $a = 1.18$  mm.

where  $I_0$  has units of Amperes. The time averaged power coupled out is:

$$P_{\text{coup}} = \frac{1}{2} I_0^2 \sin^2[k_0 h] \cdot Z_L \quad (2.92)$$

where  $Z_L$  is the characteristic impedance of the transmission line feeding the port. Based on the dissipation principle (Eqn. 2.1) we find:

$$Q = \omega \frac{2W_e}{P_{\text{coup}}} \quad (2.93)$$

$$= \frac{\omega \epsilon}{2} \left[ \omega^2 \mu_0^2 Q^2 / k_0^4 \cdot (I_0 \bar{E}_n \frac{\cos[k_0 h] - 1}{k_0})^2 \right] / P_{\text{coup}} \quad (2.94)$$

$$= \frac{1}{2} Q^2 \left[ \frac{\omega \mu_0}{k_0 Z_L} \frac{\bar{E}_n^2}{k_0^3} \tan^2[k_0 h / 2] \right] \quad (2.95)$$

which when solved self-consistently gives:

$$Q = \frac{2(Z_L / \eta)}{(\bar{E}_n^2 / k_0^3) \tan^2[k_0 h / 2]} \quad (2.96)$$

As expected  $Q$  increases when a probe is placed near a node of  $\bar{E}$ , for shorter length, for larger volumes and for higher frequencies.

### Evanescent Coupling

Without a pin in the vicinity of the aperture, the cavity couples inductively to the circular waveguide. Collin's dipole excitation formula above does not work as  $J = 0$ , and power must couple out through the circular waveguide, below cutoff. The power  $P_c$  lost through the aperture defines  $Q_c$  according to Eqn. 2.1, and may have a complicated analytical expression. However, below the cutoff frequency of the lowest frequency mode of the waveguide,  $TM_{01}$ , complex power  $S = \frac{1}{2}\Re[E \times H^*]$  flows only evanescently. We expect it will evanescently decay for a length  $\Delta z$  before reaching the coaxial probe and finally scattering into the  $TM_{00}$  (TEM) mode of the transmission line and dissipating in a load  $Z_L$  at the end of the line. We can determine the coupling quality factor from Eqn. 2.1

$$Q_c = \frac{\omega U}{\frac{1}{2}\Re[\int (\vec{E} \times \vec{H}^*) \cdot d\hat{A}]} \quad (2.97)$$

Below cutoff both  $E$  and  $H$  are attenuated by a factor  $\exp(i\beta\Delta z)$  for  $\beta = \sqrt{k^2 - k_c^2}$ , leading to an exponential increase in  $Q_c$  as the probe is retracted a distance  $1/2\beta$  (see Fig. 2.8). The suppression per unit length is determined by  $k_c = p_{nm}/a$  the cutoff wavenumber for a circular waveguide in terms of  $p_{nm}$  the  $m$ th root of  $J_n$  and the waveguide radius  $a$ .

### 2.3.5 Conclusions

There are many mechanisms of loss for resonant cavities. The use of superconductors mitigates some, and the choice of geometry can alter participation of lossy materials by several orders of magnitude. Furthermore the identification of sources of dissipation is difficult, and knowing the participation enables sound judgement and prioritization of further research. A 3D cavity geometry allows us to remove many of the prime suspects of dissipation in planar cavities and qubit experiments: the damaged possibly polycrystalline surface of a wafer, or cavity wall oxidized. The wireless interaction removes the need for wirebonds and solder. Nevertheless we retain planar resonators for Ch. 5 where the large percentage of energy stored in the substrate of planar resonators is used for the coupling of extremely weakly interacting magnetic spins. But first, we further develop the behavior of simple dipoles embedded within cavity resonators, which benefit as well from the lack of dissipation.

# CHAPTER 3

---

## Circuit QED

---

CIRCUIT quantum electrodynamics (circuit QED), in analogy with cavity QED, is the use of circuits as artificial atoms coupled to microwave resonators and often in modeling the resonators themselves. The physics of atoms, electrons and the fluctuations of discrete electromagnetic modes are explored instead using superconducting devices with effective dipole moments. There have been many dissertations in the Schoelkopf Lab and at Yale that develop this correspondence, addressing (among other things) issues of design [25], extended descriptions of the Hamiltonian [38], techniques of quantum measurement [39], and implementation of quantum algorithms [40]. This work concentrates on the implementation circuit QED in three-dimensional (3D) cavities.

In this chapter we introduce cavity QED and review the recreation of its classic Jaynes-Cummings Hamiltonian using superconducting circuits coupled to a microwave cavity. We then express the limitations to coupling strength for magnetic spins (which we implement experimentally in Ch. 5) and derive equivalence of electric dipoles in a 3D cavity with traditional circuit QED (see experiments in Ch. 6). We discuss the transmon as an electric dipole, leaning heavily on a recent review [41]. We then proceed to a new description of coupled circuit behavior that better captures the multimode environment presented by 3D cavities to a qubit. This model uses a pole decomposition of the environment which motivates a discussion of dissipation in this new picture.

### 3.1 Introduction

In cavity QED the electromagnetic field modes are quantized as harmonic oscillators. We write the electric field operators in terms of the vacuum electric field  $\mathcal{E}_0$  and a factor  $\vec{f}(r)$  containing polarity and amplitude normalization [17]:

$$\hat{E}(r) = i\mathcal{E}_0 [f(r)\hat{a} - f^*(r)\hat{a}^\dagger] \quad (3.1)$$

where  $\hat{a}$  and  $\hat{a}^\dagger$  are the annihilation and creation operators, and the quantum harmonic oscillator Hamiltonian is  $H = \hbar\omega_c(a^\dagger a + 1/2)$ . The normalization is related to the vacuum energy found by integrating over the volume:

$$\langle 0 | \int \epsilon_0 \frac{1}{2} |\hat{E}|^2 dV | 0 \rangle = \frac{1}{4} \hbar\omega_c \quad (3.2)$$

which for effective volume

$$\mathcal{V} = \int |f(r)|^2 dV \quad (3.3)$$

defines the rms electric field amplitude of the mode:

$$\mathcal{E}_0 = \sqrt{\frac{\hbar\omega_c}{2\epsilon_0\mathcal{V}}} \quad (3.4)$$

The potential energy of a point-like dipole is  $U = -\vec{d} \cdot \vec{E}$  leading to an interaction Hamiltonian [41] (assuming the atom is a two-level system):

$$H = \hbar g (\hat{a} + \hat{a}^\dagger) \sigma_x \quad (3.5)$$

where  $g$  is the vacuum Rabi coupling which quantifies the dipole matrix element between ground and excited states is

$$\hbar g = -\mathcal{E}_0 \langle e | \hat{d} \cdot \vec{f}(r) | g \rangle \quad (3.6)$$

and is proportional to the zero-point electric field at the dipole. The dimensionless ratio  $g/\omega$  determines the regime of interaction between dipole and cavity, and in the limit of when  $g$  is larger than the decay rate of every dissipative element of the system (the cavity decay rate  $\kappa$ , the spontaneous emission  $\gamma$  or captive lifetime of the atom  $\gamma_\perp$ ), we enter the strong coupling regime of the Jaynes-Cummings Hamiltonian [42], which in the rotating wave approximation

is given by:

$$H = \hbar\omega a^\dagger a + \frac{1}{2}\hbar\omega_q\sigma_z + g(a\sigma^+ + a^\dagger\sigma^-) \quad (3.7)$$

## 3.2 Cooper-pair Box and Transmon

Replicating the Hamiltonian Eqn. 3.7 and its generalization for a superconducting qubit with many energy levels has been the subject of much previous work [38]. The transmon qubit has become the dominant variety of superconducting qubit due to its ease of fabrication, control, measurement, and performance as a coherent quantum device. It is an evolution of the Cooper-pair box (CPB), a superconducting island coupled to the environment through a Josephson junction and was designed to eliminate several mechanisms of decoherence while having a large electric dipole coupling with its host cavity.

### 3.2.1 Circuit Quantization

In circuit QED, experiments with the transmon qubit involve a superconducting circuit instead of an atomic dipole, although the interaction with the cavity mode is similar. Rather than handle the electric field directly, we model the cavity with an equivalent LC circuit. In fact, by quantizing the modes of an LC oscillator here, we can extend the treatment in a later section to a multimode description of the environment as a generalized impedance.

The charge and flux (integrated voltage) parameters of an LC oscillator can be quantized much as can a mass on a spring [43]. The Hamiltonian is written

$$H_{LC} = \frac{1}{2C}\hat{Q}^2 + \frac{\hat{\Phi}^2}{2L} \quad (3.8)$$

where

$$\hat{Q} = -iQ_{ZPF}(\hat{a} - \hat{a}^\dagger) \quad (3.9)$$

$$\hat{\Phi} = \Phi_{ZPF}(\hat{a} + \hat{a}^\dagger) \quad (3.10)$$

for charge  $\hat{Q}$ , flux  $\hat{\Phi}$ , and  $Z_0 = \sqrt{L/C}$ , in terms of the unitless ladder operators and the

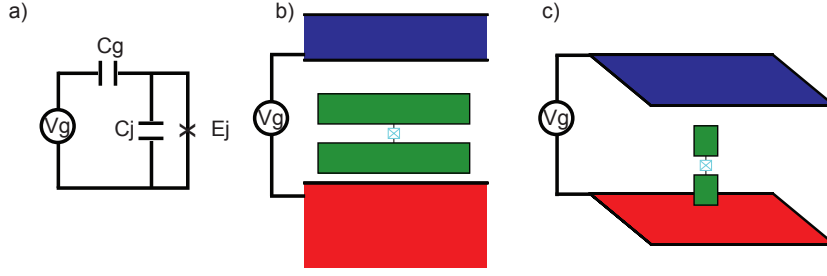


**Figure 3.1:** a) The bias configuration of the CPB. b) Planar and c) 3D cavity coupling to the CPB, including electrodes that provide  $C_\Sigma$  and voltage division  $\beta$ .

root-mean-squared zero-point fluctuations

$$Q_{ZPF} = \sqrt{\frac{\hbar}{2Z_0}} \quad (3.11)$$

$$\Phi_{ZPF} = \sqrt{\frac{\hbar Z_0}{2}} \quad (3.12)$$

and give the usual Hamiltonian

$$H = \hbar\omega_c (a^\dagger a + 1/2) \quad (3.13)$$

The effective LC circuit is determined by the resonant frequency  $\omega_c$  and the requirements of geometry.

### 3.2.2 Cooper-pair Box

The transmon exists in a special regime of CPB parameters where  $E_J \gg E_C$ . The CPB Hamiltonian is

$$H = 4E_C (\hat{n} - n_g)^2 - E_J \cos \hat{\phi} \quad (3.14)$$

where  $E_C = e^2/2C_\Sigma$  is the electrostatic energy to add a single electron to the island,  $E_J$  is the Josephson energy, and  $\hat{\phi}$  is the superconducting phase across the junction. It is coupled capacitively via a voltage  $V_g$ , which applies a voltage across the junction  $V_J = \beta V_g$ , where  $\beta = C_g/C_\Sigma$  is a voltage division factor and  $C_g$  is the gate capacitance. This voltage alters the energy of the CPB, and when coupled to a quantized cavity mode with  $\hat{V} = \hat{Q}/C$  and  $V_g = V_{DC} + \hat{V}$  allows for both a classical charge bias and quantum state control of the

observable  $\hat{N}$ . Expanding the electrostatic Hamiltonian:

$$H_{\text{el}} = 4E_C (\hat{N} - n_g/2)^2 + \frac{4E_C C_g^2 \hat{V} (2V_g + \hat{V})}{e^2} - \frac{4E_C C_g \hat{V} \hat{N}}{e} \quad (3.15)$$

where the last term couples cavity ladder operators ( $\hat{V}$ ) to junction charge number ( $\hat{N}$ ).

The particular bias charge determines the transition matrix elements, but for  $n_g = 1$ , the charge number operator has matrix elements  $\langle e | \hat{N} | g \rangle = \langle e | \sigma_x | g \rangle$ ; in this case we replace  $\hat{N} \approx \sigma_x = \sigma^- + \sigma^+$ , approximating the interaction Hamiltonian using the rotating wave approximation

$$H_i = \hbar g (a^\dagger + a) \sigma_x \quad (3.16)$$

$$= \hbar g (a^\dagger \sigma^- + a \sigma^+) \quad (3.17)$$

as that of a dipole coupling to the cavity. Then the Hamiltonian for the CPB matches Eqn. 3.7 with

$$g = \frac{eV_{\text{rms}}}{\hbar} \beta \quad (3.18)$$

The coupling  $g$  can be hundreds of MHz, sufficient to perform quantum operations in nanoseconds yet still small enough that counter-rotating terms in the Hamiltonian can often be ignored.

### 3.2.3 Dipolar coupling

The strength of coupling between atom and cavity is important and has significant physical limitations. In particular, the dimensionless  $g/\omega$  is restricted by geometry and remarkably involves the fine structure constant  $\alpha$ . We now calculate  $g$  semi-classically by beginning with the power emitted as the dipole radiates into free space and instead forcing it instead to couple with a 1D transmission line.

### Electric dipole

An oscillating electric dipole  $p_0$  emits radiation power [44] which may be expressed as

$$\langle P \rangle = \frac{\mu_0 p_0^2 \omega^4}{12\pi c} \quad (3.19)$$

$$= \frac{\mu_0 p_0^2 \pi \omega^2}{\epsilon_0 \lambda^2 3} \quad (3.20)$$

after replacing two factors of frequency  $\omega/2\pi = c/\lambda$  with the wavelength  $\lambda$ . In the semi-classical approximation this radiated power obeys

$$\langle P \rangle = \Gamma \hbar \omega \quad (3.21)$$

and we may simplify further using the terms for the vacuum impedance  $\eta_0 = \sqrt{\mu_0/\epsilon_0}$  and the resistance quantum  $R_K = 2\pi\hbar/q_e^2 \approx 26 \text{ k}\Omega$ , giving:

$$\Gamma = \frac{2\pi^2 \eta_0 p_0^2}{3 R_K \lambda^2 q_e^2} \omega \quad (3.22)$$

$$= \frac{4\pi^2 \alpha \Delta x^2}{3 \lambda^2} \omega \quad (3.23)$$

where the fine structure constant is  $\alpha = \eta_0/2R_K \approx 1/137$  and  $p_0 = q_e \Delta x$  is the dipole moment. Fermi's Golden Rule for decay to a continuum of states determines  $\Gamma = \frac{g^2}{\omega}$  according to coupling strength  $g$ . We are interested primarily in the order of magnitude of the electrostatic coupling of such a dipole; although we began with a formula for the 3D radiation of a dipole, we will now approximate a solution for a 1D transmission line by simply substituting  $w^2$  (the approximate cross-sectional area for the dipole to emit into) for  $\lambda^2$ . Furthermore define a voltage division factor  $\beta = \Delta x/w$  to obtain

$$\frac{g}{\omega} = 2\pi\beta\sqrt{\frac{\alpha}{3}} \quad (3.24)$$

An alternative derivation yields a similar but more precise relation [25, 45], and suggests that we may use the root-mean-squared electric field  $E_{\text{rms}}$  as in Eqn. 3.6 to determine  $g$  for an electric dipole in a 3D cavity.

Since we know the electromagnetic mode structure (the TE and T

$$\frac{1}{2} \left( \frac{1}{2} \hbar \omega \right) = \frac{1}{2} \int_0^a dx \int_0^b dy \int_0^d \varepsilon_0 [E_0 \sin(\pi x/a) \sin(\pi z/d)]^2 dz \quad (3.25)$$

$$= \frac{1}{8} abd \varepsilon_0 E_0^2 \quad (3.26)$$

taking  $a, b, d \rightarrow \lambda$  for the generic 3D resonator, we note that  $E_{\text{rms}} = E_0/\sqrt{2}$  and substitute 1, such that

$$\frac{g}{\omega} = \frac{q_e \Delta x}{\hbar \omega} E_{\text{rms}} \quad (3.27)$$

$$= \left( \frac{\Delta x}{\lambda} \right) \sqrt{2\alpha} \quad (3.28)$$

$$= \beta \sqrt{2\alpha} \quad (3.29)$$

which retains the fine structure constant, and is very close to Eqn. 3.24, so indeed we can expect 3D cavities to couple to electric dipoles with a  $g$  of the same order of magnitude.

### Magnetic dipole

We can show that an electron coupling through its magnetic moment has an interaction which is miniscule in comparison using a similar semi-classical calculation of the dipole radiation. From Griffiths we know the power radiated by a magnetic dipole in free space is:

$$\langle P \rangle = \frac{\mu_0 m_0^2 \omega^4}{12\pi c^3} \quad (3.30)$$

where  $c$  is the speed of light and for a spin-1/2 particle  $m_0 = g_S \frac{1}{2} \frac{\hbar q_e}{m_e}$  is the transition magnetic dipole moment, and  $g_S \approx 2$  is the Lande g-factor. We can make the semi-classical approximation again to get:

$$\Gamma = \frac{\mu_0 m_0^2 \omega^3}{12\pi c^3 \hbar} \quad (3.31)$$

$$= \frac{\pi}{3} \frac{\eta_0}{\hbar/q_e^2} \left( \frac{m_0}{c q_e \lambda} \right)^2 \omega \quad (3.32)$$

after substituting  $\omega^2 = \left(\frac{2\pi c}{\lambda}\right)^2$ . Using the continuum decay rate  $\Gamma = \frac{g^2}{\omega}$  before replacing the wavelength  $\lambda^2 \rightarrow w^2$  we obtain

$$\frac{g_m}{\omega} = \frac{m_0}{wq_e c} \sqrt{\frac{\pi}{3} \frac{\eta_0}{\hbar/q_e^2}} \quad (3.33)$$

$$= \frac{2\pi m_0}{wq_e c} \sqrt{\frac{\alpha}{3}} \quad (3.34)$$

and  $g_m \sim 50$  Hz for the typical  $w = 5 \mu\text{m}$  gaps in our coplanar waveguide. Here there is no perfect equivalent of  $\beta$  with magnetic spins, but one analog is the filling factor  $\nu$  of the mode with spins. Alternatively, we may calculate the strength of coupling via the rms current vacuum fluctuations of our resonators. Using Eqn. 2.15 the effective parameters of a quarter-wave shorted resonator are:

$$L_{\lambda/4} = \frac{4Z_0}{\pi\omega_0} \quad (3.35)$$

$$C_{\lambda/4} = \frac{\pi}{4Z_0\omega_0} \quad (3.36)$$

$$Z_{\lambda/4} = \frac{4Z_0}{\pi} \quad (3.37)$$

An effective circuit model produces the root-mean-squared B field using the zero-point current in the resonator. At 1/2 photon, half the energy is magnetic, such that

$$I_0 = \sqrt{\frac{\hbar\omega}{2L}} \quad (3.38)$$

$$= \frac{1}{2} \sqrt{\frac{\pi\hbar\omega^2}{2Z_0}} \quad (3.39)$$

A current creates a magnetic field  $B = \frac{\mu_0 I}{4\pi r^2}$  which couples to an electron spin at rate 2.86 MHz/gauss, and when placed just above the stripline may have only  $g_m = 5$  Hz for typical coplanar waveguide shunt parameters. This too suggests coupling many orders of magnitude smaller than that which we can create using a CPB. In fact, comparing Eqn. 3.33 and Eqn. 3.24 for stripline gaps  $w = 5 \mu\text{m}$ :

$$\frac{g}{g_m} = \frac{q_e \Delta x}{2\mu_B} c \quad (3.40)$$

$$\approx 10^7 \quad (3.41)$$

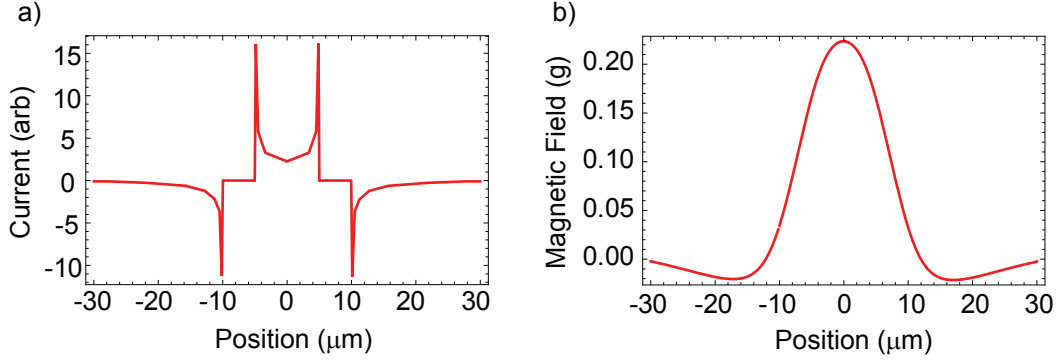


**Figure 3.2:** a) Current distribution in coplanar waveguide with  $w = 5 \mu\text{m}$ ,  $d = 10 \mu\text{m}$  b) the approximate magnetic field  $5 \mu\text{m}$  within the substrate, with 1 mA current flowing.

where  $\mu_B = \frac{\hbar}{2} \frac{q_e}{m_e}$  is the Bohr magneton. Quantum operations between a qubit or cavity and a single magnetic spin are infeasible with such a small coupling.

One strategy to overcome this deficiency is to organize a collective coupling through the use of an ensemble of electron spins. Because they must be distributed throughout the mode, they all experience a different coupling  $g_m$  (this complicates other matters, including the use of Hahn echo pulses). We can simulate the rms  $g_m$  by considering the field profile of the coplanar waveguide, modelling with Sonnet, a semi-2D finite element simulator\*. Plotting the estimated current and field profiles at representative positions, we see that there are small regions close to the gaps that have divergent B next to the superconductor. Regardless, drawing at random from points in the substrate along a  $50 \Omega$ ,  $\omega/2\pi = 14 \text{ GHz}$  resonator, we find:

$$B_{\text{rms}} = \left[ I_0 \sqrt{\int_0^{\pi/2} \sin[x]^2 dx} \right] \sqrt{\frac{1}{M} \sum B(\vec{r}_i)^2} \quad (3.42)$$

$$\approx 20 \text{ Hz} \quad (3.43)$$

We can then expect an ensemble of  $M$  spins couple collectively with  $g_{\text{tot}} = g_{\text{rms}} \sqrt{M}$ ; because of their small size, it is reasonable to imagine the  $10^{12}$  necessary to reach coupling strengths on par with the CPB, and the prospect of using spins for a quantum memory makes for an interesting object of study. Our experimental work in implementing them is presented in Ch. 5. In the remainder of the present chapter, having justified the use of electric dipoles in

\* [www.sonnetsoftware.com](http://www.sonnetsoftware.com)

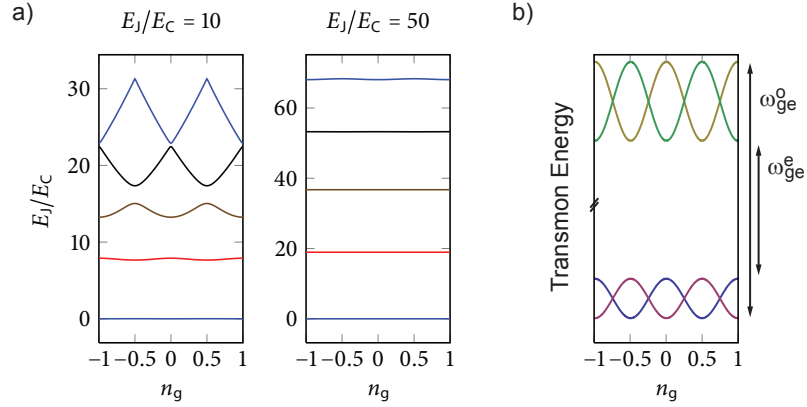


**Figure 3.3:** a) The first four levels of the transmon in units of  $E_C$ . Reproduced from [38]. b) Quasiparticle parity permits two different transitions  $\omega_{ge}$ , with difference no greater than the charge dispersion  $\hbar\varepsilon$ .

circuit QED, we summarize the useful properties of the transmon and introduce black-box quantization in order to more accurately model a qubit inside a 3D cavity.

### 3.2.4 Transmon

While the Cooper-pair box may couple with a large electric dipole to the cavity, its sensitivity to fluctuations in charge offset  $n_g$  is inconvenient, and the CPB is often implemented in the transmon limit where the Josephson energy  $E_J$  is much greater than the charging energy  $E_C$  [45]. This flattens the electrostatic energy levels (see Fig. 3.3a), effectively removing the dependence on  $n_g$  and increasing the frequency stability of the qubit against the presence of trapped electrons on the sapphire surface, piezoelectric effects driven by mechanical oscillations, quasiparticle tunneling across the junction or otherwise uncontrolled gate voltage. The charge dispersion for each level  $|m\rangle$  of the qubit is suppressed exponentially as  $E_J/E_C$  increases

$$\varepsilon_m = E_m(n_g = 1) - E_m(n_g = 0) \quad (3.44)$$

$$\sim (-1)^m E_C \frac{2^{4m+5}}{m!} \sqrt{\frac{2}{\pi}} \left(\frac{E_J}{2E_C}\right)^{\frac{m}{2} + \frac{3}{4}} \exp(-\sqrt{8E_J/E_C}) \quad (3.45)$$

Neglecting gate charge  $n_g$ , we may expand the Hamiltonian for small values of  $\phi$ , in the form

of an effective LC circuit:

$$H = H_0 + V \quad (3.46)$$

$$= \frac{1}{2C_\Sigma} Q^2 + \frac{1}{2L_J} \Phi^2 + V_{\text{nl}} \quad (3.47)$$

where  $C_\Sigma$  is the electrostatic charging energy of a pad and the effective inductance is  $L_J = (\frac{\hbar}{2e})^2 / E_J$ , the linear part of the Josephson potential. Furthermore, in the transmon limit where large  $E_J/E_C$ ,  $\phi_{ZPF} = \sqrt{\frac{2E_C}{E_J}}$  is small and the quartic term in the remaining Josephson potential gives

$$V_{\text{nl}}^{(4)} = -\frac{1}{24} E_J \phi^4 \quad (3.48)$$

$$= -\frac{1}{12} E_C (a + a^\dagger)^4 \quad (3.49)$$

$$\approx -\frac{E_C}{2} (a^\dagger a^\dagger a a + 2a^\dagger a) \quad (3.50)$$

which renormalizes the harmonic oscillator frequency and introduces an anharmonicity of approximately  $E_C/\hbar$ . This allows us to use qubit pulses as fast as a few nanoseconds without unintentionally addressing higher levels, although these can in fact be a resource for quantum gates between multiple qubits [46].

The reduction of the anharmonicity to  $\alpha \approx E_C$  which can be 100-500 MHz means that the transmon has many addressable levels and its interaction with the cavity is best described by a generalization of the the Jaynes-Cummings Hamiltonian (see Fig. 3.4):

$$\hat{H} = \hbar \sum_j \omega_j |j\rangle \langle j| + \hbar \omega_r \hat{a}^\dagger \hat{a} + \left( \hbar \sum_i g_{i,i+1} |i\rangle \langle i+1| \hat{a}^\dagger + h.c. \right) \quad (3.51)$$

where  $\hbar \omega_j$  are the qubit energy levels and we neglect for a moment the anharmonicity of the cavity. Energy levels  $|i\rangle, |i \pm 1\rangle$  are connected through the ladder operators while connection between non-adjacent levels is omitted to first order. Because it is so nearly a harmonic oscillator, driving higher transitions becomes easier, with matrix elements  $\sim \sqrt{N}$ ; in addition, the dipole interaction energy increases slightly with larger  $E_J/E_C$  as the number operator

from Eqn. 3.14 changes

$$\hbar g_{ij} = \beta e V_{\text{rms}} \langle j | \hat{N} | i \rangle \quad (3.52)$$

$$\sim \frac{-i\beta e V_{\text{rms}}}{\sqrt{2}} (E_J/8E_C)^{1/4} \langle j | \hat{b} - \hat{b}^\dagger | i \rangle \quad (3.53)$$

through the participation of many charge states (or many Cooper pairs).

### Hybridization

The physics of the cavity-qubit interaction described in Eqn. 3.51 can take on a different characters depending upon how close to resonance the two are, as the systems hybridize, and altering the detuning within an experiment or on the fly can be very useful. The classic transmon design includes two junctions in a SQUID configuration that allows us to change the frequency of the qubit by modulating the Josephson term in Eqn. 3.14 with applied flux. The new Josephson potential

$$V = E_{J\Sigma} \cos\left(\frac{\pi\phi}{\phi_0}\right) \sqrt{1 + d^2 \tan^2\left(\frac{\pi\phi}{\phi_0}\right)} \quad (3.54)$$

where

$$E_{J\Sigma} = E_{J1} + E_{J2} \quad (3.55)$$

$$d = \frac{E_{J1} - E_{J2}}{E_{J1} + E_{J2}} \quad (3.56)$$

describes the joint effect of individual junctions  $J1$  and  $J2$ . We can tune over a wide range, altering among other things the degree of hybridization between qubit and cavity. The effect can be seen in the new eigenbasis for the diagonalized Hamiltonian, which is already available in a block-diagonal form:

$$H^{(n+1)} = \hbar \begin{pmatrix} n\omega_c + \frac{1}{2}\omega_{ge} & g\sqrt{n+1} \\ g\sqrt{n+1} & (n+1)\omega_c - \frac{1}{2}\omega_{ge} \end{pmatrix} \quad (3.57)$$

$$(3.58)$$

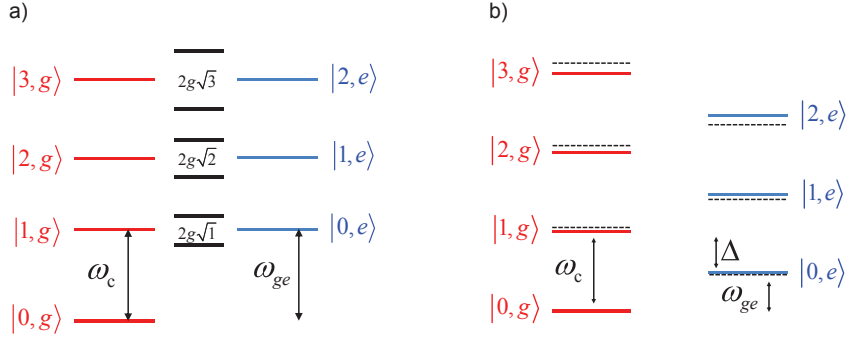


**Figure 3.4:** a) Vacuum-rabi splitting of energy levels for a resonant cavity and qubit. b) Energy levels in the dispersive case  $\omega_c = \omega_{ge} + \Delta$  showing repulsion which leads to a qubit frequency shifts down when the cavity is in an excited state (dashed lines are dressed states).

which conserves total photon and qubit excitation number  $n + 1$ , and has eigenvalues

$$E_{\pm}^{(n+1)} = \left( n + \frac{1}{2} \right) \hbar \omega_c \pm \frac{\hbar}{2} \sqrt{\Delta^2 + 4g^2(n+1)} \quad (3.59)$$

The new eigenkets are

$$|-, n\rangle = \cos(\theta_n) |e, n\rangle + \sin(\theta_n) |g, n+1\rangle \quad (3.60)$$

$$|+, n\rangle = -\sin(\theta_n) |e, n\rangle + \cos(\theta_n) |g, n+1\rangle \quad (3.61)$$

where  $\Delta = \omega_{ge} - \omega_r$  is the detuning between qubit and cavity and the degree of hybridization of the qubit with the cavity is given by

$$\tan(2\theta_n) = \left( \frac{2g\sqrt{n}}{\Delta} \right) \quad (3.62)$$

One important consequence of this exact solution is that on resonance the cavity and qubit each contain half of the system energy, and so dissipation occurs at the average of their individual rates of energy decay. Conversely, we can potentially decrease any decay of the qubit through a lossy cavity by more than an order of magnitude by detuning the qubit far enough from the cavity.

### 3.2.5 Dispersive Regime

As we have seen, the Jaynes-Cumming Hamiltonian (Eqn. 3.7) can be diagonalized exactly, yielding dressed qubit-cavity states. In the dispersive regime where the qubit-cavity system is operated with  $\frac{g}{\Delta} \ll 1$  for qubit detuning, we can make this more clear by making the unitary transformation [47]:

$$U = \exp \left[ \frac{g}{\Delta} (a\sigma^+ - a^\dagger\sigma^-) \right] \quad (3.63)$$

to find

$$UHU^\dagger = \hbar \left[ \omega_r + \frac{g^2}{\Delta} \sigma_z \right] a^\dagger a + \frac{\hbar}{2} \left[ \omega_q + \frac{g^2}{\Delta} \right] \sigma_z \quad (3.64)$$

such that the qubit transition has been shifted, and the cavity transition frequency depends on the qubit state. Or equivalently,

$$H_{\text{eff}} = \hbar \omega a^\dagger a + \frac{\hbar}{2} \left[ \omega_q + \frac{g^2}{\Delta} (1 + 2a^\dagger a) \right] \sigma_z \quad (3.65)$$

Here it is clear that the qubit transition frequency changes with photon number by an amount  $\chi = 2g^2/\Delta$ . In fact it can be shown more precisely that the transmon dispersive shift of qubit frequency is  $\chi = 2g^2\alpha/\Delta(\Delta - \alpha)$  [45], where  $\alpha$  is the qubit anharmonicity. Because  $g$  can be rather large due to the transmon's electric dipole coupling to the cavity,  $\chi$  can be 10's of MHz, and much larger than the qubit or cavity linewidth  $\gamma$  or  $\kappa$ . This is the strong-dispersive regime of cavity QED, and it has striking consequences for qubit coherence which will be explored further in Ch. 8; in particular, any photon which transits the cavity will contain in its frequency complete information about the qubit state.

In the dispersive regime, the slight  $g/\Delta$  hybridization of cavity and qubit gives for the one-excitation dressed states

$$|-, 0\rangle \sim -\frac{g}{\Delta} |e, 0\rangle + |g, 1\rangle \quad (3.66)$$

$$|+, 0\rangle \sim |e, 0\rangle + \frac{g}{\Delta} |g, 1\rangle \quad (3.67)$$

and consequently a portion of the decay occurs at some fraction of the rate of other system's

intrinsic rate:

$$\kappa_y = \left(\frac{g}{\Delta}\right)^2 \gamma \quad (3.68)$$

$$\gamma_\kappa = \left(\frac{g}{\Delta}\right)^2 \kappa \quad (3.69)$$

In fact the qubit and cavity may be connected to several dissipation baths; the cavity decays through input and output couplers ( $\kappa_{\text{in}}, \kappa_{\text{out}}$ ) as well as internal losses ( $\kappa_{\text{int}}$ ). The energy decay rate of the qubit is the sum of many processes, including contributions from the cavity Purcell effect ( $\gamma_\kappa$ ), junction quasiparticle damping, or some other intrinsic limit:

$$\gamma_{\text{tot}} = \gamma_\kappa + \gamma_{\text{qp}} + \gamma_i + \dots \quad (3.70)$$

### 3.2.6 Coherent Drive

Coherent control of the cavity or qubit quantum state is achieved through an additional drive Hamiltonian, following [38]

$$H_{\text{dr}} = \varepsilon(a + a^\dagger)(d + d^\dagger) \quad (3.71)$$

where  $\varepsilon$  describes the coupling between the cavity  $\omega_a$  and reservoir harmonic oscillator  $\omega_d$ . Approximating a stiff drive with  $d|\alpha\rangle = \alpha|\alpha\rangle$  we have

$$H_{\text{dr}} = (a + a^\dagger)(\xi e^{-i\omega_d t} + \xi^* e^{i\omega_d t}) \quad (3.72)$$

$$= a\xi^* e^{i\omega_d t} + a^\dagger \xi e^{-i\omega_d t} \quad (3.73)$$

where to allow the rotating wave approximation the interaction energy  $\xi = \varepsilon\beta$  is not so strong compared to the driven transition energies  $\hbar\omega_{ij}$ . Transforming into the frame rotating with the drive using the operator

$$U(t) = \exp\left[i\omega_d t \left(a^\dagger a + \sum_j j|j\rangle\langle j|\right)\right] \quad (3.74)$$

we find

$$\hat{H} = U(H + H_{\text{dr}})U^\dagger - iU\dot{U}^\dagger \quad (3.75)$$

$$= \Delta_r a^\dagger a + \sum_j \Delta_j |j\rangle\langle j| + \sum_j g_{j,j+1}(|j+1\rangle\langle j| a + h.c.) + (a\xi^*(t) + a^\dagger \xi(t)) \quad (3.76)$$

for detunings  $\Delta_r = \omega_r - \omega_d$ ,  $\Delta_j = \omega_j - j\omega_d$ , and allowing for a slowly varying  $\xi(t)$ . In particular when the qubit is far detuned  $\Delta \gg g$  from the qubit we may drive the cavity on resonance, creating an interaction which reduces to the slowly varying terms

$$H_{\text{int}} = a\xi^*(t) + a^\dagger\xi(t) \quad (3.77)$$

effecting a displacement  $D[\beta]$  of the cavity from the vacuum state where  $\beta = \int \xi(t)dt$ , and placing the cavity in a coherent state. If the cavity is sufficiently anharmonic we substitute  $(\sigma^- + \sigma^+)$  for  $(a + a^\dagger)$ , and a similar expression applies for driving of a qubit. Placement of the qubit inside a resonator alters its spontaneous emission rate through the Purcell effect. In fact, the same pseudo-resonator or mode which allows a means of driving the Hamiltonian also provides a thermal bath into which the qubit and cavity dissipate.

### 3.3 Black-box Quantization

There have been several attempts at extensions of circuit QED [48–50] with the goal of modelling a small number of harmonics or parasitic modes of the cavity and their influence on the qubit. In planar experiments with coplanar waveguide resonators there are an infinite number of harmonics in addition to the electromagnetic mode structure of the sample holder itself. However after the move from planar to 3D cavities, where the existence of a large (possibly infinite) number of modes can be examined more accurately, a group of colleagues at Yale developed a serious treatment of a Josephson junction in the presence of an environmental admittance. This landmark paper [51] on Black-box quantization (BBQ) successfully described the spectrum of all the early 3D transmons and holds great promise for application in more diverse cavities and multiple-qubit experiments.

#### 3.3.1 Two coupled LC Resonators

In classic circuit QED, the qubit is coupled to a single mode of a resonator. In fact, we may reduce the problem by linearizing the qubit and deal only with two coupled LC resonators. Given flux and charge parameters  $\Phi_1$ ,  $\Phi_2$ ,  $Q_1$ , and  $Q_2$ , the Hamiltonian is

$$H_0 = \frac{1}{2}L_1\omega_1^2Q_1^2 + \frac{1}{L_1}\Phi_1^2 + \frac{1}{2}L_2\omega_2^2Q_2^2 + \frac{1}{2L_2}\Phi_2^2 \quad (3.78)$$

$$V = \beta\sqrt{L_1L_2}\omega_1\omega_2Q_1Q_2 \quad (3.79)$$

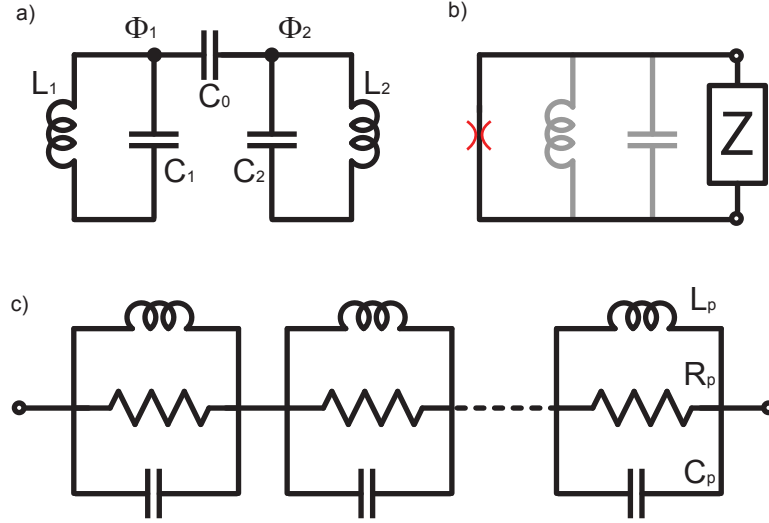


**Figure 3.5:** a) Schematic of a Josephson junction and its coupling to an environmental impedance b) Replacement of Josephson junction with linearized  $C_J$ ,  $L_J$  (both absorbed into  $Z$ ), and nonlinear "spider" element. c) pole-decomposition of environment  $Z(\omega)$ .

where the potential mixes operators between the two circuits with bare frequencies  $\omega_q$  and  $\omega_c$ . We may find the normal modes of the two dressed harmonic oscillators by using a Bogoliubov transformation to find the dressed frequencies

$$\omega_{\pm} = \left[ \frac{1}{2} \left( \omega_1^{-2} + \omega_2^{-2} \pm \sqrt{(\tilde{\omega}_1^{-2} + \tilde{\omega}_2^{-2})^2 - 4[\omega_1^{-2}\tilde{\omega}_2^{-2} + \tilde{\omega}_1^{-2}\omega_2^{-2} - \omega_1^{-2}\omega_2^{-2}]} \right) \right]^{-1/2} \quad (3.80)$$

for  $\tilde{\omega}_1 = 1/\sqrt{L_1(C_0 + C_1)}$  and  $\tilde{\omega}_2 = 1/\sqrt{L_2(C_0 + C_2)}$ . These procedures find the normal coordinates of the circuit. More complex circuit designs are quantized using the spanning-tree technique [43]. Starting with selected nodes and their flux variables we may find the Lagrangian, before defining the canonical momenta. In order to deal with a cavity environment which may include many modes with fields solutions not quite as analytic as the rectangular cavity's  $TE_{nml}$ , we turn instead to a numerical solution of the normal modes of the circuit model for the qubit environment.

### 3.3.2 HFSS Solution

By Foster's Theorem, any admittance can be decomposed into an equivalent circuit of parallel LCR oscillators in series. In fact, modern finite-element electromagnetic simulations can be

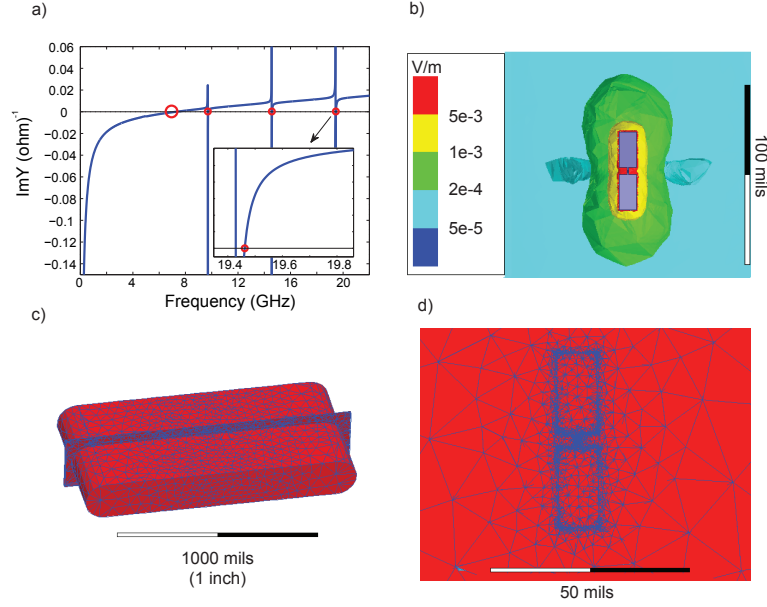


**Figure 3.6:** a) The imaginary part of the admittance  $Y(\omega)$  of the cavity seen by a port at the Josephson junction. Frequencies where  $\Im[Y(\omega)] = 0$  are resonances, emphasized here with a red circle. The circle at 8 GHz is the qubit mode. b) the magnitude of the qubit mode electric field near the device. c) Meshing of the cavity surface in HFSS. d) Meshing near the qubit junction and antenna.

used to produce the normal mode field solutions by solving the S parameters or impedance of a single-port junction device. This simplifies calculation of the dressed qubit and cavity mode frequencies, anharmonicities, and state-dependent energies.

We begin by replacing the qubit with an LC circuit in parallel with a "spider" element representing the remaining anharmonicity from  $\cos(\phi)$ . The circuit has

$$C_J = \frac{e^2}{2E_C} \quad (3.81)$$

$$L_J = \frac{\hbar^2}{4e^2 E_J} \quad (3.82)$$

and in Fig. 3.5b, we absorb this into  $Z(\omega)$ . Each pole of the impedance

$$Z(\omega) = \sum_{p=1}^M \left( j\omega C_p + \frac{1}{j\omega L_p} + \frac{1}{R_p} \right)^{-1} \quad (3.83)$$

is a zero of the admittance  $Y(\omega) = 1/Z(\omega)$  and

$$L_p = \frac{2}{\Im Y'(\omega_p)} \quad (3.84)$$

$$R_p = \frac{1}{\Re Y(\omega_p)} \quad (3.85)$$

$$C_p = \frac{\Im Y'(\omega_p)}{2} \quad (3.86)$$

$$Z_p^{\text{eff}} = \frac{2}{\omega_p \Im Y'(\omega_p)} \quad (3.87)$$

where  $Y'(\omega_p) = \left. \frac{\partial \Im[Y(\omega)]}{\partial \omega} \right|_{\omega=\omega_p}$ . This simplifies the calculation of the mode quality factor when lossy materials are simulated:

$$Q_p = \frac{\omega_p \Im Y'(\omega_p)}{2 \Re Y(\omega_p)} \quad (3.88)$$

In Fig. 3.6a we show the simulated port admittance for a lossless rectangular waveguide cavity with an inserted sapphire wafer and transmon device. Here the lowest zero-crossing is the qubit mode, whose  $|\vec{E}|$  is displayed in Fig. 3.6b. When the exact dimensions and loss tangents of surface contaminants and lossy materials are unknown at the time of simulation, their participation in the qubit mode may still be calculated after the fact. As these provide the ultimate limit to qubit quality factor (after detuning from cavity modes that might spoil it through the Purcell effect), this is an important topic for future work.

Finally, the flux variable (or time integral of voltage) across the junction is just the sum of the voltage across each resonator in Fig. 3.6c,  $\phi(t) = \sum_p \phi_p(t)$ , or

$$\hat{\phi} = \sum_{p=1}^M \sqrt{\frac{\hbar}{2} Z_p^{\text{eff}}} (\hat{a}_p + \hat{a}_p^\dagger) \quad (3.89)$$

where annihilation and creation operators  $\hat{a}_p, \hat{a}_p^\dagger$  produce a linearized Hamiltonian  $H_0 = \sum_p \hbar \omega_p \hat{a}_p^\dagger \hat{a}_p$ . Because measured modes are a linear combination of qubit and cavity modes (which are independent of  $n_g$ ), the effects of charge dispersion are expected to be reduced compared to the bare (uncoupled) case. However, as higher levels of the transmon (known to have increased charge dispersion) are also hybridized, exact calculation of charge dispersion is still an open problem.

### Josephson Non-linearity

The remaining non-linear part of the Josephson potential is written in the  $\phi$  basis, and a simple evaluation in perturbation theory gives the anharmonicities  $\chi_{pp}$  and cross-mode energies,  $\chi_{pp'}$ . Using the perturbation

$$H_{\text{nl}}^{(4)} = -\phi^4/24\phi_0^2L_J \quad (3.90)$$

and assuming the linear Hamiltonian  $H_0$  has eigenstates  $|n_1, n_2, \dots, n_M\rangle$  with non-degenerate energies

$$E_{n_1, n_2, \dots, n_M}^{(0)} = \sum_i n_i \hbar \omega_i \quad (3.91)$$

we apply first order perturbation theory using  $E_{n_1, n_2, \dots, n_M}^{(1)} = \langle n_1, n_2, \dots, n_M | H_{\text{nl}} | n_1, n_2, \dots, n_M \rangle$  giving, in addition to fast-rotating terms which we drop,

$$H_1 = H_0 + \sum_p \Delta_p \hat{n}_p + \frac{1}{2} \sum_{pp'} \chi_{pp'} \hat{n}_p \hat{n}_{p'} \quad (3.92)$$

determining the Lamb shift correction  $\Delta_p$  as well as the state-dependent frequency shifts  $\chi_p$ . To lowest order this gives each mode  $\omega_p$  an anharmonicity

$$\chi_{pp} = -\frac{L_p}{L_J} \frac{C_J}{C_p} E_C / \hbar \quad (3.93)$$

which is proportional to the ratio of the linear mode characteristic impedances, and a state-dependent frequency shift

$$\chi_{pp'} = -2\sqrt{\chi_{pp}\chi_{p'p'}} \quad (3.94)$$

which is twice their product. Of these parameters,  $L_p$ ,  $C_p$ , and  $E_C$  can be solved numerically using HFSS, and  $E_J$  can be controlled by junction design. The geometric capacitance of the junction  $C_J \approx \epsilon_0 l$  is of order a few femtofarads. When considering a single cavity mode interacting with the qubit, the new effective Hamiltonian is

$$H_{\text{eff}}/\hbar = \omega_c a^\dagger a + (\omega_q - \chi a^\dagger a) b^\dagger b - \frac{\alpha}{2} b^\dagger b^\dagger b b, \quad (3.95)$$

where  $a$  and  $b$  are the cavity and qubit annihilation operators,  $\alpha$  is the qubit anharmonicity, and  $\chi$  is the cross-Kerr or state-dependent shift.

### 3.3.3 Far detuned cavity modes

Returning to the example of two coupled LC oscillators, we can consider the shunted Josephson junction capacitance  $C_\Sigma$  and inductance  $L_j$  linked through an effective capacitor  $C_g = C_j/C_\Sigma$ , along with an effective L,C for the TEM modes of the 3D resonator. The constant  $E_y$  electric field of the  $TE_{101}$  mode of a rectangular cavity with dimensions  $a, b, d$  is described using an effective LC circuit with

$$L_{101} = \frac{a}{\epsilon b d \omega_r^2} \quad (3.96)$$

$$C_{101} = \epsilon b d / a \quad (3.97)$$

and explains the particularly simple coupling of the mode to the typical 3D transmon antenna with length  $d_0/2$ . We can calculate  $\chi_n$  in the dispersive limit. The admittance from the junction port is

$$Y(\omega) = \frac{1}{i\omega L_j} + i\omega C_j + \frac{1}{\frac{1}{i\omega C_0} + \frac{1}{i\omega C_r + (i\omega L_r)^{-1}}} \quad (3.98)$$

We can verify using Eqn. 3.80 that  $\Im[Y(\omega_\pm)] = 0$ . In the fully buffered limit where  $\beta \approx C_j/C_0 \ll 1$ , we have using Eqn. 3.94

$$\chi = \frac{C_0^2 q_e^2 \omega_{ge} \omega_r^4 Z_r}{C_j^2 (\omega_{ge}^2 - \omega_r^2)^2} / \hbar \quad (3.99)$$

Using the Eqn. 3.96 for the effective LC circuits of the rectangular cavity  $TE_{101}$  and in fact all  $TE_{10n}$  modes, this is for volume  $V$ ,

$$\chi_n = \frac{a^3}{V} \frac{q_e^2}{\hbar \epsilon d_0} \frac{\omega_q \omega_r^3}{(\omega_{ge}^2 - \omega_r^2)^2} \beta \quad (3.100)$$

which in the limit of large detuning decreases as  $1/\omega_n$ . A similar estimate can be obtained using the vacuum fluctuation electric field of the mode as in Eqn. 3.25.

### 3.3.4 Purcell Decay

Using the black-box circuit model we can re-introduce dissipation in a quantized LC circuit which qualitatively follows the Purcell effect in Eqn. 3.68. A lossless LC resonator can be given a finite quality factor  $Q = \omega\tau$  and ringdown time  $\tau$  with the addition of a parallel

admittance  $Y$  with real conductance  $G = 1/R$ . Current fluctuations  $\hat{I}$  in the resistor induce corresponding fluctuations in the flux  $\hat{\Phi}$  parameter of the LC, with interaction

$$H_{\text{int}} = \hat{\Phi} \hat{I} \quad (3.101)$$

In fact, Fermi's Golden Rule gives that there are transitions in the oscillator:

$$\Gamma^{m \rightarrow n} = \frac{1}{\hbar^2} |\langle n | \hat{\Phi} | m \rangle|^2 S_{II}[\omega] \quad (3.102)$$

for current noise two-sided spectral density

$$S_{II}[\omega] = \frac{2\hbar\omega \Re[Y]}{1 - \exp(-\hbar\omega/k_b T)} \quad (3.103)$$

For an LC oscillator in parallel with a conductance  $G_{\text{int}}$ , the transition rates from state  $|n\rangle$  at  $T = 0$  we evaluate the matrix elements and the spectral density for both positive and negative frequencies, finding

$$\Gamma_{\uparrow}^n = \frac{(n+1)\kappa}{1 - \exp(\hbar\omega/k_b T)} \quad (3.104)$$

$$\Gamma_{\downarrow}^n = \frac{n\kappa}{1 - \exp(-\hbar\omega/k_b T)} \quad (3.105)$$

$$(3.106)$$

where  $\kappa = 1/\tau$  for  $\tau = RC = 1/\Gamma_0$  the exponential time constant of the circuit. At zero temperature,  $\Gamma_{\uparrow}^n = 0$  and fluctuations only stimulate decay, but for finite temperature the rates produce a thermal state, with steady-state probability of finding  $N$  excitations given average number  $\bar{n}$  [52]

$$P(\bar{n}, N) = \bar{n}^N / (\bar{n} + 1)^{N+1} \quad (3.107)$$

and mean excitation number which is the Bose-Einstein occupancy,  $\bar{n} = 1/(\exp(\hbar\omega/k_b T) - 1)$  from a detailed balance of the transition rates of the harmonic oscillator. With the addition of a coupling impedance (see Fig. 3.7) to an outside bath, we may use Foster's Theorem to represent transformed conductances  $G_{\text{in}}$  and  $G_{\text{out}}$  which may be at different temperatures  $T_{\text{in}}$  and  $T_{\text{out}}$ , distinct from  $T_{\text{int}}$ , the temperature of lossy cavity materials internal to the cavity. These are only effective temperatures, as often they describe the black-body radiation from higher stages, and we prefer to use mean photon numbers  $\bar{n}_{\text{in}}$ ,  $\bar{n}_{\text{out}}$ , or  $\bar{n}_{\text{int}}$ . Then the sum of

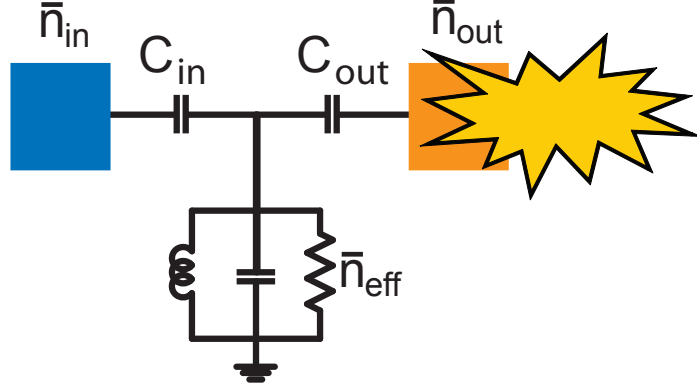


**Figure 3.7:** A circuit model for thermal baths connected to a resonator.

rates determines the steady state population  $\bar{n}_{\text{eff}}$  of the cavity:

$$\bar{n}_{\text{eff}} = \frac{\sum_i n_i \kappa_i}{\sum_i \kappa_i} \quad (3.108)$$

which is balanced by the total decay rate of the cavity. Typically these  $\kappa_i$  are fixed, but a crucial component of this work is the implementation of a variable coupler (see Sect. 4.3.2) which allows the adjustment of  $\kappa_{\text{out}}$  over several orders of magnitude. With it we investigate the influence of  $\bar{n}_{\text{eff}}$  on qubit coherence. In addition, we observe how an oscillator that is overcoupled to a cold output mode can have low steady-state population even if the cavity itself is hot. When a non-equilibrium noise temperature is enforced, as we do in Ch. 8 with an incoherent drive, photons from one mode can overwhelm all others, and we may write

$$\bar{n}_{\text{eff}} = \bar{n}_{\text{dr}} \kappa_c / \kappa \quad (3.109)$$

for a mode with coupling rate  $\kappa_c$  and mean photon number  $\bar{n}_{\text{dr}}$ . Also note that when the entire apparatus has its temperature raised,  $\bar{n}_{\text{eff}}$  is given by this physical temperature.

## CHAPTER 4

---

### Experimental Techniques

---

CIRCUIT QED experiment already has large legacy of experimental techniques. Much of the work for this thesis was done in dilution refrigerators installed two generations of graduate students ago, whose microwave components are largely unchanged. But, 2010 saw a number of transitional forms in the Schoelkopf laboratory. We received installation of several new dry ( $^4\text{He}$  cryogen-free) refrigerators, and experiments moved from circuit boards and planar resonators to cavities that themselves appeared very much like our traditional sample holders. In many ways the experiment design, measurement scheme and cryogenic techniques were largely unchanged, and much of it has been exquisitely described in past dissertations [25].

In this chapter, I will discuss a few interesting experimental details needed for this thesis and on examples that are pertinent to the transition between the old and new eras and deserve to be emphasized. First I will describe the fabrication of our coplanar resonators in Sect. 4.1. Then I will recount the prototyping and fabrication of the 3D transmons samples in Sect. 4.1.3. Next, I will give a description of the typical dilution fridge setup in Sect. 4.2, with closer examination of steps taken to ensure cryogenic thermalization. Finally, I note changes to the sample holder design in Sect. 4.3 and give a brief overview of the pulse generation and measurement chain in Sect. 4.4 and 4.5.

## 4.1 Resonator Fabrication

Device fabrication for circuit QED can have several steps with long lead times; despite the excellent cleanroom facilities a few doors down the hallway, it is often useful to create a large reserve of partly completed devices. This pipelining of the whole process minimizes idle time when starting a new experiment. Fabrication for planar circuit QED devices has traditionally begun with an optical lithography step. Starting with a wafer with sputtered niobium or aluminum, we use a mask (which itself can take a few weeks to design, a month to order) to pattern several dozen chip designs, dice the developed wafer, and store the results until a design is selected for further processing. A similar bank of useful printed circuit (PC) boards exists, and this process has an analog for 3D resonator experiments in which first we must obtain a supply of high-purity aluminum and then send out various designs for machining. This modularity of our experiments quickened the pace of new experiments.

Recently, much of this pipeline has moved in-house. The Becton cleanroom has purchased a mask making tool (Heidelberg), which allows laser printing of a mask with reasonable dimensions. Custom PC boards can now be made on demand by an LPKF MiniContac RS, instead of ordering large batches from Hughes Circuits or Bay Area Circuits. In fact the new 3D transmon design, with an entirely “wireless” qubit needs no circuit board for simple experiments. While machining its cavity might have been a slow step in the past, the cost of rapid machining has also decreased with the proliferation of CNC technology, allowing the ordering of sample holders (the “octobox”) and more recently 3D cavities from 3D Pros, Zero Hour Machining, and a handful of other machine shops in half the delivery time of the Yale Machine Shop (which is, however, of unrivalled quality).

### 4.1.1 Coplanar waveguide

The microwave platform for all early experiments in the lab has been coplanar waveguide. In fabrication of resonators for spin experiments, we needed cavities spread along a broad band of frequencies to match the diversity of spin species and their tunable range. To additionally take advantage of broadband spin ensembles, we chose a configuration which included a feedline with shunt resonators (see Sect. 2.2.1) rather than a chip with several cavities [54]. Using either capacitive finger [27] or inductive [55] couplers we create fixed coupling quality factors that ranged from several thousand to a million.

One possibility for added convenience in the process is to leave the cavity coupling

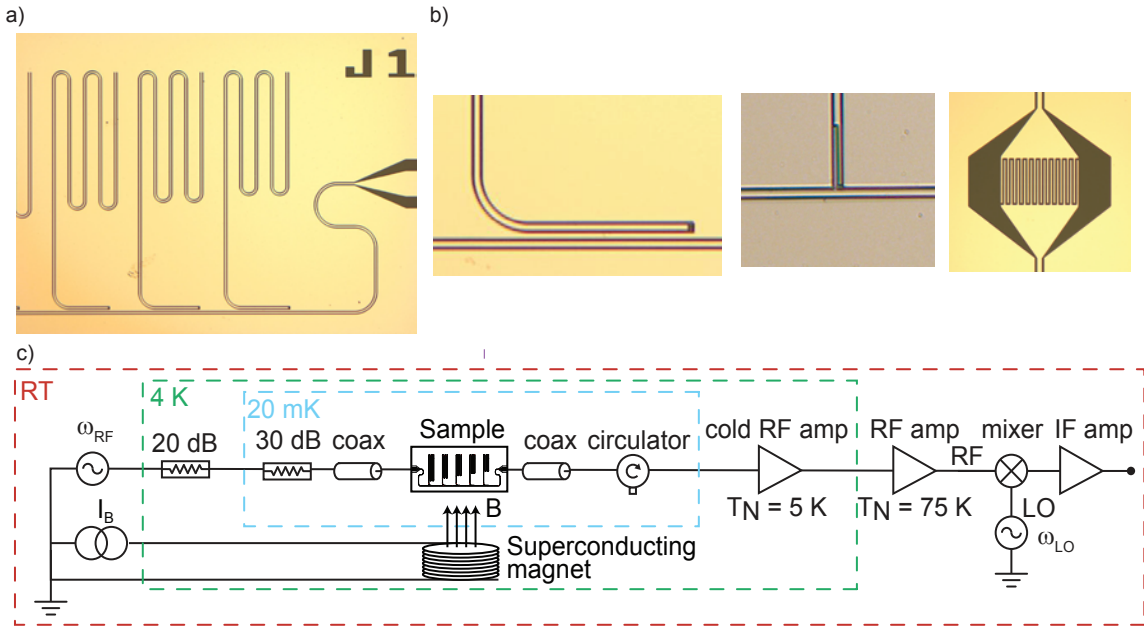


**Figure 4.1:** a) A closeup of chip AWo8J1, used as a control for the spin experiments. For many of the spin experiments, we used 180 nm of DC sputtered niobium film, etched using a Reactive Ion (RIE) process in an Oxford 80, etching for  $\approx 120$  seconds, with an endpoint detected optically. The wafer is then diced and stored with protective resist until needed. b) different cavity coupler geometries (left to right: inductive, single finger, multiple finger) to reach desired quality factors. c) block diagram of spin apparatus with magnet.

capacitors unwritten until the experiment design is fixed. These capacitors affect the rate of energy decay through the cavity, which can alter behavior of precision readout schemes or limit the performance of qubits too close to resonance through the Purcell effect (see Sect. 3.3.4). Until recently this has required an extra step involving lengthy calibration because of the large distance between couplers and qubits on a chip, however the new e-beam writer installed in 2012 is able to scan a much larger distance and would be able to write couplers separately as it is capable of writing devices across a full wafer.

#### 4.1.2 3D Resonators

Machined 3D resonators have a very similar process to the coplanar waveguide. In order to achieve a base level of reproducibility (and time-effectiveness!), rectangular cavities are provided to one of several mail-order companies for machining according to CAD instructions. Luckily, there is built in modularity that allows us to choose the cavity  $Q$  after fabrication simply choosing different lengths for SMA coupling pins. Turn-around time for a new 3D cav-

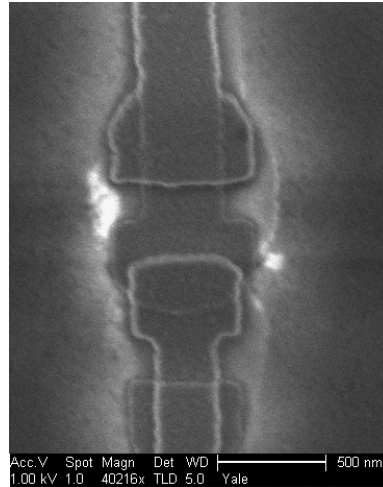


**Figure 4.2:** An SEM image of a Josephson junction from a 3D transmon test wafer.

ity design is 2-4 weeks, allowing rapid prototyping of new ideas. Electromagnetic resonator design is a classic field of physics [56, 57], the replication of which is an active area of interest for our lab and issues of material purity, electroplating, chemical polishing, and magnetic shielding have been discussed; however the experiments in this thesis are the results of our typical procedures as described in past work, and new best practices are still being developed.

### 4.1.3 Qubit Fabrication

Fabrication procedures for the classic transmon (described in [25] in detail) and the 3D transmon are nearly identical. All qubits for this thesis were on 450 or 500  $\mu\text{m}$  thick sapphire. This substrate is spun with two layers of resist, PMMA and PMA-MAA, in order to allow for construction of a Josephson junction using the Dolan bridge technique. Because sapphire is a good insulator and has little ability to dissipate charge, an initial layer of  $\sim 10$  nm Al was deposited to sink the electron beam current to ground while patterning.

All qubits except SP1 and SP2 (see Table 6.2 for a list of 3D qubit devices) were patterned using a Sirion SEM using a 30 keV beam and Nabity e-beam conversion software. Most lithography difficulties were due to overexposure and cross-dosing from the large coupling pad area; avoiding use of the largest beam spot size often reduced the number of shorted junctions. After e-beam resist development with Shipley MF-312, we deposited aluminum (purchased from Alfa Aesar, at 99.999% purity) in three steps: first a layer of Al, an oxidation, and a final layer deposited at an angle. Oxidation time, temperature, and pressure are crucial parameters that are carefully controlled so that only junction area varies in the fabrication

process. Becton has two excellent, automated, fully logged Plassys deposition and oxidation systems, and qubits J4, J5, and J6 were the first to utilize the newer one with a separate oxidation chamber. Hopefully its expanded Josephson junction formation capabilities will be further tested in the near future.

## 4.2 Experimental Setup

All experiments were performed with similar cryogenic apparatus, at  $\approx 10 - 30$  mK, the base temperature of a dilution refrigerator. Spin experiments used both a Cryoconcept fridge with  $100 \mu\text{W}$  at 100 mK and a Kelvinox fridge with  $400 \mu\text{W}$  at 100 mK cooling powers, while 3D transmons experiments were performed in these as well as several varieties of dry fridges (without the need for  $^4\text{He}$  consumption) from Vericold and Oxford Instruments. Microwave coaxial UT-85 lines connected the experiment with the top of the fridge; measurements were done in transmission, with two lines per experiment (fewer with the use of microwave switches from Radiall). All copper sample holders and brackets were seated firmly and made of OFHC copper for high thermal conductivity with plentiful copper braid straps to provide additional points for thermal anchoring, and both spin (Ch. 5) and qubit (Ch. 6 and 7) experiments used cryogenic attenuation to eliminate Johnson-Nyquist noise emitted by room-temperature electronics.

The large bias magnetic field used in spins experiments was created using massive superconducting magnets at the bottom of the Kelvinox and Cryoconcept fridges, immersed in liquid helium, and had a field per ampere which peaked near the samples at approximately  $985 \text{ G/A}$  and  $\approx 330 \text{ G/A}$ , respectively. The magnets included a secondary coil to cancel field at higher stages and prevent damage to sensitive microwave components like our circulators. They were driven first by an American Magnetics programmable current source, and later by a Kepco BOP 20-10M-4886, and had persistent switch elements to create a long-term stable field disconnected altogether from the supplies. Since the magnetic field tolerances for the first 3D transmon SQUID experiments were much more stringent, we drove the magnets through a  $10 \text{ k}\Omega$  resistor with a Yokogawa 7651 DC Voltage Source.

### 4.2.1 Reflective Attenuation

Cryogenic attenuation is a critical part of superconducting qubit experiments, and the basics have not changed. Each fridge is first wired with both dissipative and reflective attenuation

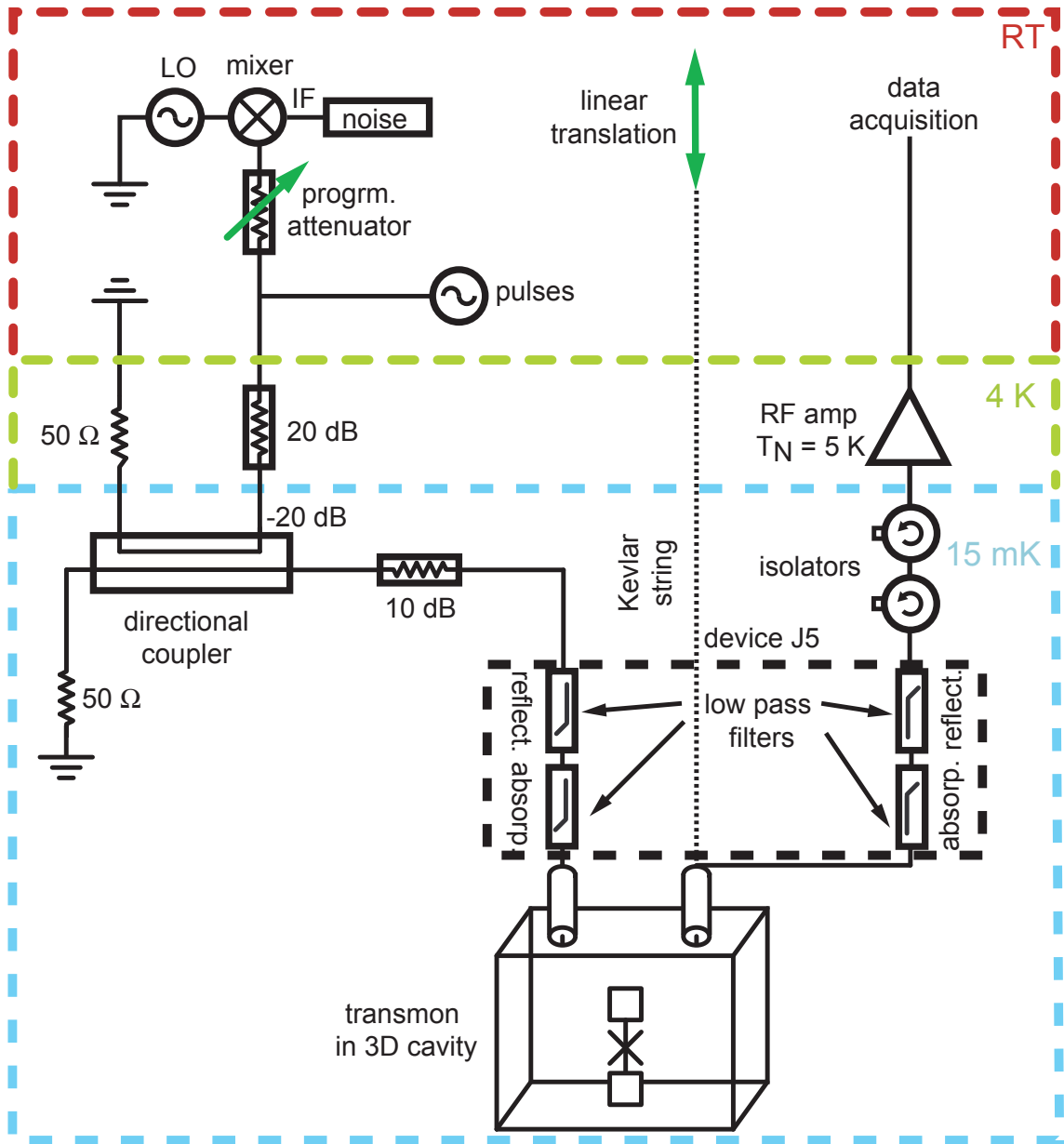
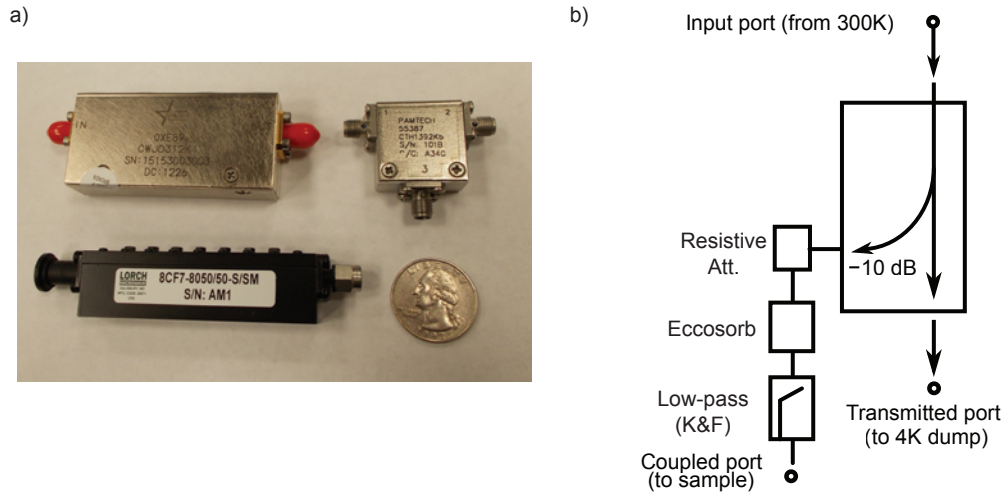


Figure 4.3: Experimental apparatus for photon induced dephasing experiments with qubit J3



**Figure 4.4:** a) Reflective attenuation. Clockwise from top left: Pamtech isolator, Pamtech circulator, Lorich cavity filter. b) Diagram of filtering on cavity input lines, including directional coupler to redirect power to 4K stage.

to isolate the experiment at the base plate from blackbody radiation above. Several reflective microwave components were incorporated into the lab's standard drive and measurement lines as experiments with the 3D transmon progressed. We used, for example, a K&F low-pass tubular filter with a passband below either 10 or 12 GHz (6L250-10000 and 6L250-12000), to reflect power at frequencies much higher than the qubit and cavity (up until self-resonance at  $\sim 20$  GHz). Reflective elements have the benefit of being more narrow band than many absorptive components, allowing us to block incidence or emission of radiation at specific frequencies. We tested multistage cavity filters from Lorich or K&L with precise passbands 100 MHz to several GHz wide. Placed on the typically overcoupled output port of a cavity, these allow fast readout while limiting Purcell decay rates of the detuned qubit.

In early 3D transmon experiments, directional couplers were used to redirect some incident drive power to stages of the fridge with surplus cooling power. Although potentially a four-port device, these had one  $50 \Omega$  termination, and were used as shown in Fig. 4.4b, to replace 10 dB-20 dB of absorptive attenuation at the base plate by routing drive signals through the weakly coupled port and sending the rest to be dissipated at 4K. Although a useful idea, one should be careful with this implementation; the broadband performance the directional coupler is unclear and it may no longer reject noise above  $\sim 18$  GHz. Microwave switches have been suspected of allowing either extra broadband noise or infrared light to

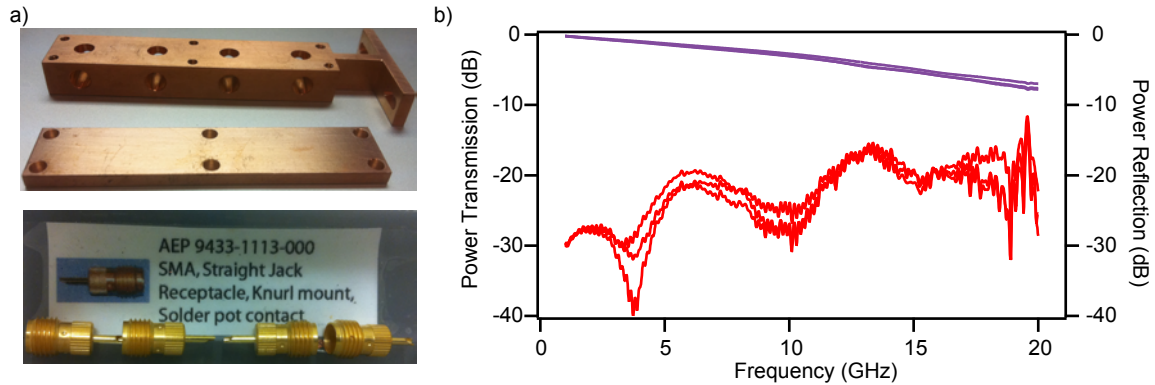


**Figure 4.5:** a) Eccosorb filter housing and jacks b) Broadband performance of the filters (purple:  $S_{21}$ , red:  $S_{11}$ )

reach the sample, and have been integrated into the modern generation of fridges at the base plate, possibly harming qubit coherence times; it may also be inappropriate to rely on directional couplers and microwave switches for blocking power (perhaps they must always be paired with resistive filters as described in the next Section)\*. On the output side, cryogenic isolators and circulators (manufactured by Pamtech) are used to reject blackbody noise from the HEMT amplifier and above; although they do a very good job at providing 20-30 dB isolation at 8 GHz (suppressing thermal excitations of the qubit and fundamental cavity mode), they have unknown behavior at microwave frequencies above 18 GHz.

#### 4.2.2 Absorptive Attenuation

Absorptive attenuation is used at different stages of the fridge, simultaneously fulfilling several purposes. First, a resistive connection from a coax centerpin to the ground shield (which is itself clamped and connected to a fridge plate) allows the centerpin to be thermally sunk. Providing a point of thermalization at as many stages as possible ensures cooling from plates with most cooling power; since cooling power in a fridge is generally quadratic in temperature  $T$ , it is beneficial to “sink early, sink often”. In addition to thermal sinking, resistors also reduce blackbody photons emitted from plates above the mixing chamber base plate. A resistor at a fixed temperature  $T$  will in steady state fill all modes with the Bose-Einstein population  $P_{BE}(T) = 1/(\exp(\hbar\omega/k_b T) - 1)$ . An attenuator at a lower stage in the fridge but

\* We also remain suspicious of hand-formable coaxial cables (such as from rfcoax.com), whose mesh outer conductor may allow infrared light to enter the coax.

with finite temperature will eliminate much of the photon power which continues toward the sample; the remainder is added with its own contribution.

At high temperatures with  $k_B T > \hbar\omega$  summing the different  $\bar{n}$  is equivalent to adding effective temperatures, however, once we reach the cryogenic regime this is no longer true. We are concerned with the final average photon number in our cavities; assuming only thermalized sources and an overcoupled cavity, this number is

$$\bar{n}_{\text{eff}} = \bar{n}_{\text{base}} + A_{\text{base}} \cdot (\bar{n}_{4K} + A_{4K} \cdot (\bar{n}_{300K})) \quad (4.1)$$

$$= P_{BE}(T_{\text{eff}}) \quad (4.2)$$

where  $P_{BE}(T)$  is the Bose-Einstein distribution,  $A_{4K}$  and  $A_{\text{base}}$  are the attenuation at the 4 K stage and at the base plate, and  $T_{\text{eff}}$  is the effective temperature, and obeys a simple scaled addition like Eqn. 4.1 with  $T \sim \bar{n}$  only for temperatures much larger than  $\hbar\omega/k_b$ . To determine the steady state photon number actually inside the cavity, we calculate instead the temperature of the mode just outside the coupler (by neglecting  $\bar{n}_{\text{base}}$ ) and use Eqn. 3.109. Reducing the expression to the contribution from only the input side of the cavity and to

$$\bar{n}_{\text{eff}} = A_{\text{base}} P_{BE}(T_{4K}) \frac{\kappa}{\kappa_c} \quad (4.3)$$

In particular, for the standard attenuation setup of 20 dB at 4K, 30 dB at the base plate, and an extra 10 dB of loss in the long coaxial cables at the top of the fridge, we can expect  $\bar{n}_{\text{eff}} = (0.008 + 0.01 + \bar{n}_{\text{base}})$  at 8 GHz, outside the couplers. An additional 10 dB at the base plate would reduce this to a total of 0.001, an effective temperature of 55 mK.

One way to supplement the reflective attenuation with finite bandwidth from the previous section is to include wideband absorption, such as the eccosorb filter developed by Daniel Santavicca [58] and based on the humble properties of iron particles. The filter is constructed from a large copper cold-finger (see Fig. 4.5a) capped with two SMA jacks, and is filled with Eccosorb CR-110 epoxy from Emerson-Cuming, which has a typical attenuation of 2 dB/cm at 10 GHz which increases at higher frequencies (see Fig. 4.5b). While it has not been measured above 18 GHz, it has already improved the thermalization of our 3D transmon devices (see Sect. 8.4) and enabled our best qubit coherence times.

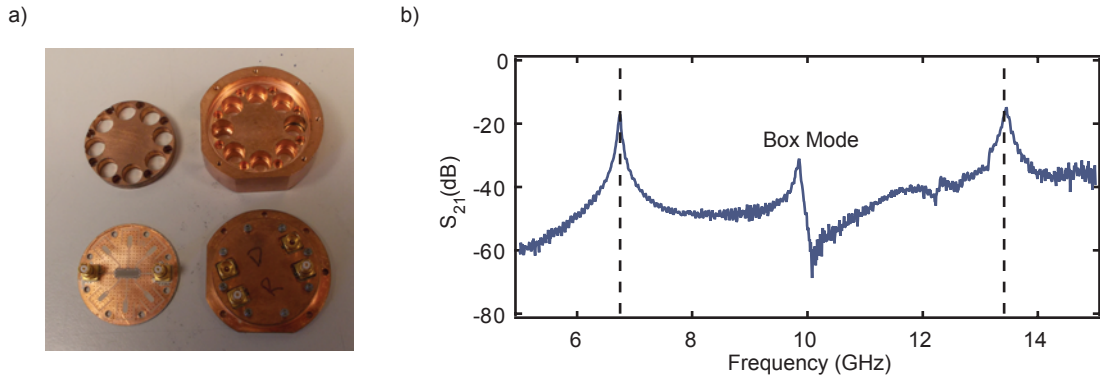


**Figure 4.6:** a) Octobox sample holder and parts (clockwise from top right: octobox, pcb with flipchip, pcb, and machined shim. b) Cleaned up spectrum transmission spectrum (reproduced from [40]). Dashed lines show  $\lambda/2$  and  $\lambda$  resonances of the coplanar waveguide cavity.

### 4.3 Sample Holder and 3D Cavity

Experiments were typically enclosed in either an OFHC in order to allow magnetic field, or in superconducting aluminum.

#### 4.3.1 Octobox

The sample holder for coplanar waveguide experiments is a piece of OFHC copper called the “octobox” after its eight microwave ports. Each allowed for a Rosenberger connector, which is particularly tolerant of blind mating. Although not used for these experiments, glass bead feedthroughs along with an indium wire seal can make the holder hermetic, sealed even to superfluid helium.

Spurious modes have always been a concern with coplanar waveguide, where  $\lambda$  or  $3\lambda/4$  (for  $\lambda/2$  or  $\lambda/4$  resonators) harmonics are not so far detuned from the cavity fundamental that they can be ignored. In fact, the Purcell effect from harmonics clearly limits planar transmons tuned above the cavity [50]. The slotline mode has also been noted [40], and capacitance to the opposite ground plane is included in network calculations for the charging capacitance  $C_\Sigma$  of planar transmon; this is the basis for several speculative “balanced” transmon designs [49].

But box modes of the sample holder too can interfere with qubit coherence, and are clearly seen in transmission spectra of our planar cavities (see Fig. 4.6b). These can be squeezed into a higher frequency range by filling them with conductor; as a stopgap solution I machined some additions for the sample holder, including a “flip chip” made from an

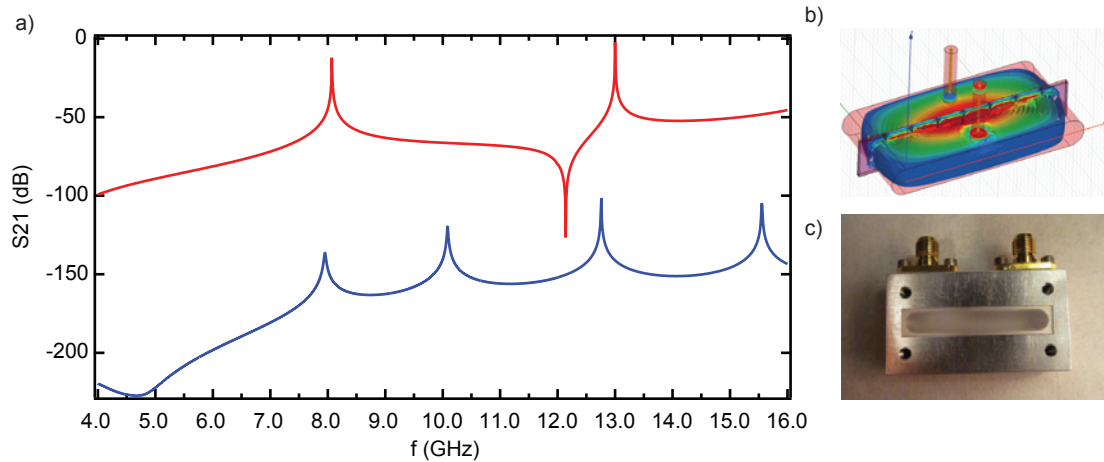


**Figure 4.7:** a) Simulated transmission through the original ( $V_1$ , below), and a slight evolution ( $V_2$ , above) of the rectangular waveguide cavity used for the 3D transmon experiments. The move to symmetric couplers suppresses of transmission through the  $TE_{102}$  mode. b) HFSS model of  $V_2$  cavity and its coupling to  $TE_{101}$  electric field c) Photograph of  $V_1$  cavity with both SMA couplers on a single cavity piece.

overturned spare pcb, and a metal shim that filled the remaining vacuum of the box (see Fig. 4.6a). This, along with extra wirebonds connecting the CPW ground planes, cleaned up the transmission spectrum significantly (with the expectation that extra coupling of the qubit may be suppressed as well). These lessons provided part of the inspiration for using a simplified 3D cavity with clear resonator mode structure for the 3D transmon.

### 4.3.2 Rectangular waveguide cavity

The rectangular waveguide (“3D”) cavity we used for transmon experiments is particularly simple, and deviates slightly from a rectangular design by having rounded sides only out of machining necessity. The cavity is split in half to allow insertion of a substrate with the qubit, and we originally chose to place the couplers on a single half of the cavity. Out of an abundance of caution, later versions of rectangular cavities moved the coupling pins to be in the center, substantially nulling transmission through the  $TE_{102}$  and other even modes. This is seen in Fig. 4.7 where simulations indicate that transmission no longer occurs from pin to pin at  $\sim 10$  GHz, however the change has not been shown to have a significant effect on qubit coherence or decay. Practically, this decouples the even modes from the output coaxial mode, such that their  $Q$  is set by the internal quality factor and the mode is populated at the internal temperature.

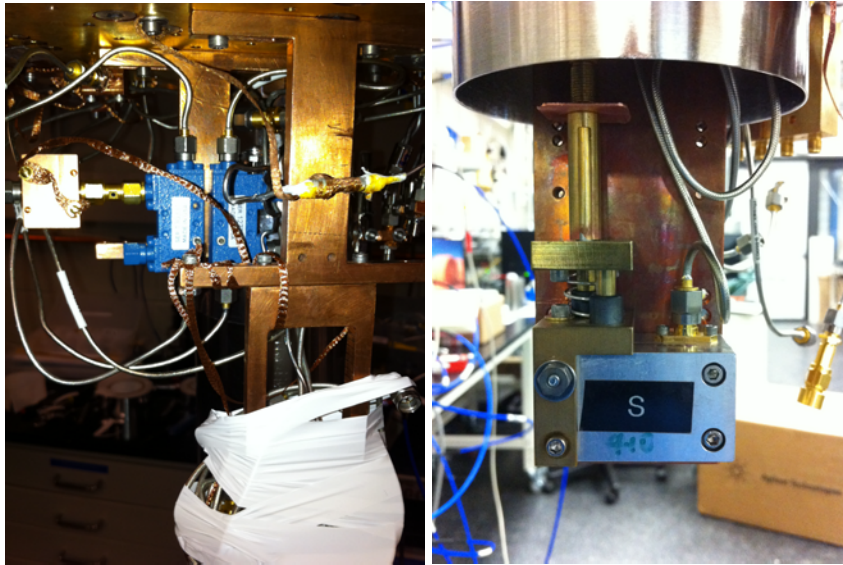


**Figure 4.8:** Base plate configuration. Left: directional coupler leads to eccosorb filter and XMA attenuator at base plate. Shown with cryoperm magnetic shield completely removed. Right: variable coupler in brass for experiment with qubit J<sub>3</sub> in aluminum cavity, with half of shield installed.

The coupler pins of a 3D cavity and the finger capacitors of a planar resonator may reject incoming photons by providing an impedance mismatch; power that reaches an undercoupled cavity is mostly reflected. Amazingly, the coupling quality factor for the 3D cavities can be adjusted *in situ* using a variable coupler developed by Andrei Petrenko and shown in Fig. 4.8. In practice, the cavity coupling rate varies by much more than the quality factor itself, which reaches an internal  $Q$  limit, and can be between 500,000 – 2,000,000 for cavities with a full sapphire chip inside; our stock rectangular waveguide cavity achieves  $Q_{\text{int}}$  up to a factor of 10 higher with a specialized chemical etch [?] or perhaps 50 after removing the sapphire. The coupling quality factor increases exponentially as less and less power escapes evanescently into a withdrawn SMA pin; the scaling of this effect agrees well with theory for superconducting and normal cavities, with and without sapphire substrates, and has been measured for both 2.33 mm and 5 mm diameter holes. There is some concern that having a physical hole opening in the cavity allows infrared light to produce quasiparticles in the junction, reducing qubit coherence, prompting us to cover it with something impenetrable yet flexible\*.

---

\* This is an interesting conjecture but it has not been proven using a control experiment. For comparison, a former colleague has qubits in “open space”, and places them on top of coplanar waveguide using a mechanical

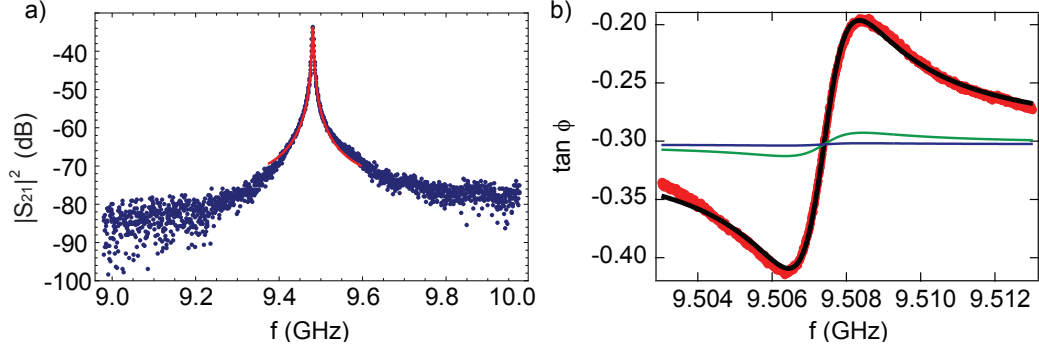


**Figure 4.9:** a) Insertion loss measurement of  $Q_c$  for an undercoupled resonator b)  $Q_c$  measurement in reflection for  $g \approx 10$  (red, with theory in black). For undercoupled ports (green,  $g = 100$  and blue  $g = 1000$ , the phase measurement is progressively more difficult.

### Phase Measurement of $Q_c$

We use two methods to extract  $Q_c$  from  $Q$  the total quality factor, in preparation of a new experiment. The first involves the phase shift of the reflected signal  $S_{11}$ . The admittance of a parallel resonator near resonance is:

$$Y = G_{\text{int}}(1 - 2i\delta Q_i) \quad (4.4)$$

and so its reflection coefficient is:

$$\Gamma = \frac{Y_{\text{out}} - Y_{\text{res}}}{Y_{\text{out}} + Y_{\text{res}}} \quad (4.5)$$

$$= \frac{1 - g(1 - 2i\delta Q_i)}{1 + g(1 - 2i\delta Q_i)} \quad (4.6)$$

for  $g = Q_c/Q_i$ . This gives us on resonance a reflection  $\Gamma = \frac{1-g}{1+g}$  and nearby a phase difference:

$$\tan \phi = \Im[\Gamma]/\Re[\Gamma] \quad (4.7)$$

$$= \tan \phi = \tan \phi_0 + \frac{-4Q\delta}{(1-g) - 4(Q\delta)^2(1+g)} \quad (4.8)$$

where  $g = Q_{\text{ext}}/Q_{\text{int}}$ , with which we may fit the  $S_{11}$  of our cavity. This method is only useful for overcoupled to slightly-undercoupled cavities  $g \sim 1$ , otherwise calibration errors make the reflection traces unusable (see Fig. 4.9b)

---

stage [59], however their coherence times do not reach those of the 3D transmon. Alternatively, there is some evidence from the Devoret lab that a hermetically sealed “light-tight” cavity improves qubit coherence

### Magnitude of Insertion Loss

Alternatively, the insertion loss for a coupled resonator depends upon the internal and coupling quality factors  $Q_i$ ,  $Q_{in}$ , and  $Q_{out}$  (see Fig. 4.9a). Transmission through the device is given by:

$$S_{|21|}^2 = \frac{IL}{1 + 4Q^2\delta x^2} \quad (4.9)$$

where  $\delta x = (\omega - \omega_0)/\omega_0$  and the insertion loss is [27]

$$IL = \frac{4Q^2}{Q_{in}Q_{out}} \quad (4.10)$$

for negligible internal loss. We can use this to estimate the  $Q_c$  of two identical couplers, even when room-temperature prevents  $Q_i$  from reaching superconducting values.

All qubit experiments include a Cryoperm shield around the sample that expels magnetic field as the fridge cools; there is some evidence that magnetic shielding is necessary for resonator quality factor measurements [56] and that many experiments naturally have a small magnetic field nearby [60]. Better shielding of cavities and local field nulling is a work in progress.

## 4.4 Pulse Generation

Pulses were generated by mixing a shaping envelope from an arbitrary waveform generator (AWG) with a center local oscillator (LO) tone; a Tektronix AWG5014 provides this IF waveform at 1 GS/s, allowing single sideband mixing (SSB) up to  $\approx 100$  MHz from the carrier frequency. Because its internal trigger is unreliable, in qubit experiments this equipment is triggered every 2 ms or less often, permitting cavity and qubit to return to a cold equilibrium state. We use a Tektronix AWG520 (which does not have this problem) or an Agilent 33250A function generator as master triggers, and the AWG5014. All equipment gets its phase reference from an SRS FS725 rubidium clock source. The steady LO tone is generated by Agilent E8267D and MXG N5183A family generators, powering low-power Marki Microwave IQ0618LXP IQ mixers. These mixers naturally have some leakage of the LO tone which is dependent upon the offset voltage for the diodes on each arm; it must be nulled using the AWG5014 channel offsets and has different optimal settings as the LO frequency changes. The quality factor of cavities in early 3D transmon experiments was 1000x larger than typical

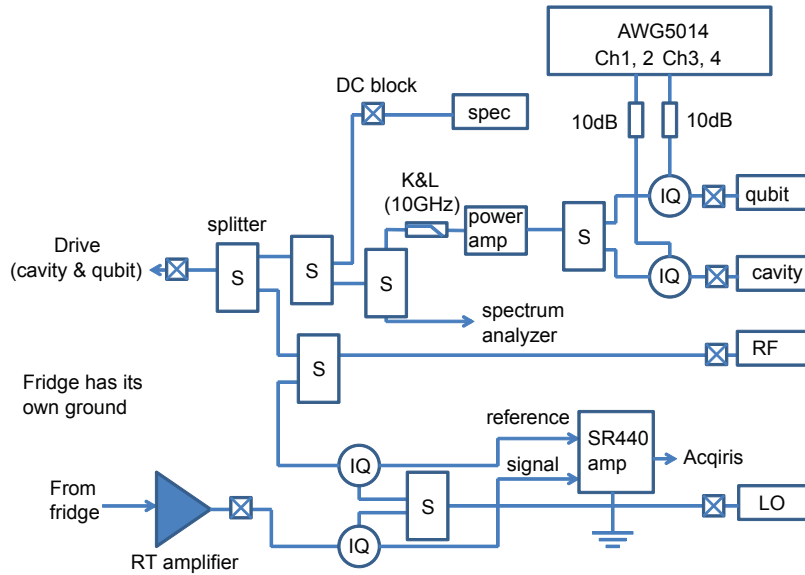


**Figure 4.10:** Microwave drive and readout diagram: Pulse generation and measurement.

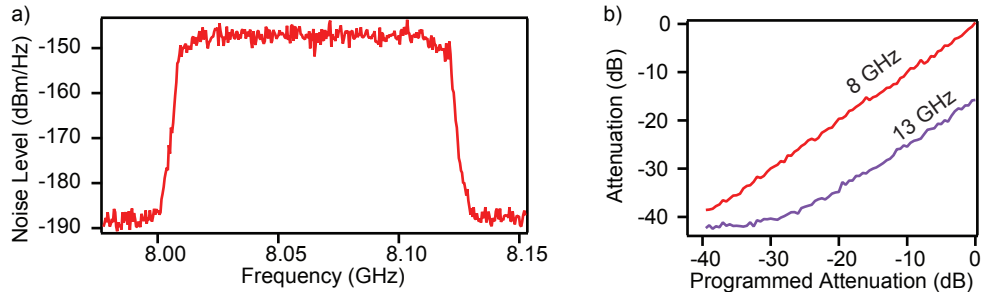


**Figure 4.11:** a) Noise generated to address the cavity transition frequency  $\omega_c$  over a 100 MHz bandwidth. A programmable Labbrick attenuator lowered the noise power. Actual versus programmed correction factors are given by the slope: 0.996 at 8 GHz and 0.929 at 13 GHz. Rolloff at high attenuation is an artifact of the measurement, from the spectrum analyzer noise floor.

experiments in traditional circuit QED, and excessive caution meant that they may have been undercoupled as well. So early on we discovered the necessity of a high-power amplifier such as the Minicircuits ZVE-3W-183+ for driving fast qubit pulses.

A Micronetics NOD-5200 1 GHz RF noise source was used along with a Labbrick programmable attenuator in Ch. 8 to automate the production of microwave noise with narrow bandwidth. Performance of the attenuator varied with frequency, especially above its rated specifications (see Fig. 4.11). An IQ mixer mixed a large spectrum of noise up to the cavity

transition frequency, while several low-pass filters ensured that power at the qubit frequency had been excluded before sending it into the fridge.

## 4.5 Measurement

Measurement was performed using a heterodyne scheme with two arms, one of which was a reference for the phase. This allows the measurement of phase shifts, for example as a function of generator frequency when the relative phase between two experiments might be scrambled and in addition removes the potential for several intrinsic types of phase drift (such as between an LO and RF generator). This configuration is a best-practice for dispersive qubit readout in which the qubit state is encoded in the phase of tone transmitted through the cavity, and when measurements are not heavily averaged (averaging on the acquisition card prevents us from more intelligently combining the phase measurements from further software processing). An IQ mixer produces a signal which is multiplied by a sine wave at the IF frequency of 10 MHz in software (digital homodyne) before being integrated to produce the phase and amplitude of the signal.

Signal from the cavity first went through several circulators and then a Caltech HEMT cryogenic amplifier with gain  $G > 30$  dB and a noise temperature  $T_N \approx 4$  K, before being input into two Miteq low-noise amplifiers (typically AFS4-08001200-10-10P-4 and AFS3-00101200-35-ULN). The microwave signal from the fridge was mixed down to 10 MHz with the reference arm signal, and amplified using an Stanford Research SR445A pre-amplifier before entering a two-channel Agilent Acqiris AP240 digitization card along with another copy of the reference arm. More recently, use of the Alazaar card (ATS-9870) has enabled shot-by-shot analysis of cavity transmitted phase and amplitude, allowing histograms and application of thresholds to the readout signal. The room-temperature control configuration is displayed in Fig. 4.10. To prevent ground loops that can disrupt thermometry and other sensitive measurements, all cables to the fridge are interrupted by an Inmet 8309 DC block (a DC open on both inner and outer conductors). Wideband measurements on the spins used an Agilent E5071C Network Analyzer because of its superior power-leveling and broadband calibration for long measurements.

## CHAPTER 5

---

### Spins

---

THERE are many approaches to the construction of a solid-state quantum computer, which might ultimately be composed of a variety of physical systems, specialized for different tasks. Among the possible approaches, spin-based quantum information processing has enjoyed a large amount of research in recent years [25, 61–64]. In particular, ensembles of electron spins in crystals have been well-studied and complement superconducting spins particularly well. As was mentioned in Chapter 3, the collective moment of many spins can interact with the electromagnetic field of a resonant cavity to form an effective harmonic oscillator, featuring similar transition frequencies to our qubits. They need not be actively trapped, may be densely packed in space, and may even be utilized in momentum-space [65] for the storage of multiple bits of information as spin-waves. Our requirements for suitable spins are similar to those for the implementation of useful qubits: they must have a large coupling to other systems so that quantum operations can be performed quickly, yet they must be protected from decay into the environment and isolated from sources of decoherence.

The study of spins through the use of microwave probes is the field of Electron Spin Resonance (ESR) or Electron Paramagnetic Resonance [36]. Where dielectrics and even metal surfaces may be rough and disordered, crystals provide a very ordered and predictable environment with excellent materials properties, and the disturbance by small numbers of defects can lead to consistent results. Dopants in silicon and diamond are common, for

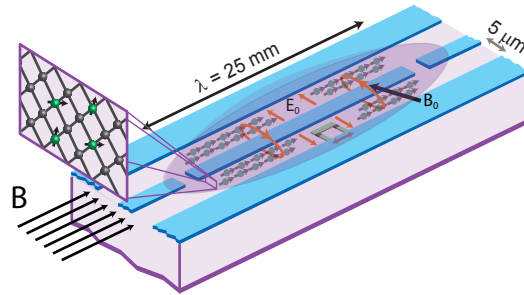


**Figure 5.1:** Defects and dopants in the crystal substrate provide electron spins to be biased by a magnetic field  $B$  and controlled using the microwave signal in a resonator.

example phosphorus substitutions in silicon [66, 67] in a crystal lattice, have been studied and shown to have particularly long  $T_2$  (with echo) of seconds and  $T_1$  of hours at liquid helium temperatures. Impurities in diamond have not only microwave but optical transitions [61].

For the most part, ESR experiments have been performed at room temperature with macroscopic samples in solution or powder form, or occasionally at  $\text{LN}_2$  or liquid helium temperatures. The field has a long history, with an especially fruitful examination of the substitutions, vacancies, and defects of crystals like diamond and sapphire. Early samples were often procured from natural lodes in South Africa, however recently crystal growing technology has improved to become commercially viable for a variety of industrial and consumer purposes.

## Chapter Organization

In this chapter, we report on experiments [68] that perform ESR at millikelvin temperatures on a platform that could integrate with our other circuit QED experiments. Circuit QED allows for many optimizations that might enhance the maximum sensitivity to spins in ESR experiments and in fact the traditional coplanar waveguide (CPW) cavities are in many ways excellent for the design of an ESR spectrometer which detects extremely small numbers of spins. At the same time, the exquisite sensitivity may be put to use by engineering stronger interactions in the support of the rest of our quantum computing effort. So in developing ESR techniques in our devices, we hope to understand what makes a spin suitable for use as a quantum memory and what limitations spins might place on future cavity QED experiments.

In the next section of this chapter we derive the limits of operation for ESR using our

platform, describing its extreme sensitivity in familiar terms of cavity QED. In subsequent sections we perform some proof of principle experiments integrating CPW cavities via several preparation methods with spins of increasing coherence properties. Beginning with DPPH, a very well-characterized ESR standard, we see that our devices permit spectrometry over a wide bandwidth when applied topically to the planar chips. Then we detail attempts to couple simple paramagnetic spin ensembles of P1 nitrogen substitutional defects in diamond, and observe the the anisotropic hyperfine splitting from  $^{14}\text{N}$  nuclei. Finally we use ruby to demonstrate the utility of a finite Crystal Field Splitting (CFS) in a spin species, reducing the degradation of our superconducting resonators which occurs in a strong magnetic field. We find that by densely filling the mode volume with spins, we achieve a type of strong coupling between spin ensembles and resonators and consider the prospects of spin ensembles for use as a quantum memory.

## 5.1 Sensitivity

In conventional ESR we couple microwave power into a resonant cavity to be dissipated by a spin sample. The amount of power coupled is limited by the magnetic participation of the spins, and the absorption of incident power is typically viewed in reflection. When the spins have been tuned into resonance with the cavity, the reflected power has a Lorentzian profile as impedance matching limits power transfer off-resonance, similar to the dip in transmission of our shunt resonators. In commercial spectrometers, typically a lock-in oscillating magnetic field is applied as well, such that the final signal appears to be the derivative of transmission vs frequency.

A single electron spin has a magnetic dipole moment  $m_0$  whose coupling to free space  $g_0 \sim 1$  Hz, determined by the weak power radiated by a magnetic spin (see Sect. 3.2.3 and Eqn. 3.30) is difficult to detect alone. In fact, even placing it inside a resonant cavity to enhance its emission through the Purcell effect only results in  $g_s \sim 20$  Hz.

While the presence of a single spin or defect may be too little to detect, this collection of  $M$  spins has a coupling  $g_s\sqrt{M}$  which can be many MHz. When in resonance, this leads to a hybridization and vacuum Rabi splitting. The frequency dispersion is often disregarded in classic ESR; feedback systems automatically compensate to track the repulsion and fixate on the frequency of maximum absorption. This is effectively an anachronism due to historical frequency instability of klystron microwave generators.

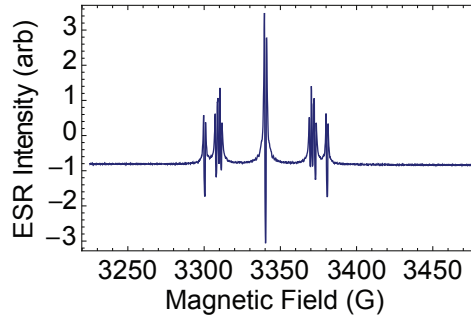


**Figure 5.2:** An ESR spectrum taken of synthetic, single crystal diamond using the Bruker machine in the Sterling Chemistry Laboratory at Yale. The trace is the derivative (with respect to magnetic field) of the absorption spectrum at different bias fields. The center transition is that of a nearly-free  $^{14}\text{N}$  electron spin conserving  $m_I = 0$ , while the satellites show different sub-populations of  $m_I = -1$  and  $m_I = 1$  spins.

### Small volumes

The great advantage of using coplanar waveguide resonators for the purpose of ESR is their large filling factor  $\nu$ , and the opportunity to maximize the amount of our chosen material that interacts with the magnetic field energy, thereby increasing our sensitivity to the resonance or damping of our microwave fields. This sensitivity is dependent upon both the participation ratio of the magnetic energy in the sample and in part upon the orientation of the  $B_0$  fields, and we may define:

$$\nu = \frac{\int |\vec{B}_0(r) \times \hat{S}| dV_{\text{sample}}}{\int |\vec{B}_0|^2 dV} \quad (5.1)$$

where  $B_0$  is the zero-point magnetic field and  $\hat{S}$  is the spin quantization axis. Inside the mode volume, this coupling has strength  $g_s = \hbar m_0 B_0$  for a single spin, where  $m_0$  is the transition magnetic dipole moment of the spin. The value  $\nu$  for spins contained in coplanar waveguide is  $\approx 0.25$ : with  $1/2$  to begin with because sample fills less than a half-plane, and another factor of  $1/2$  due to the non-orthogonality of the spins axes to  $B_0$ . Placing  $\sim 10^{12}$  spins to achieve a many-MHz coupling, creates what is effectively a harmonic oscillator which may exchange energy within an interaction time comparable to coherence times of a superconducting qubit or resonators. Amazingly, because  $B_0 \sim \sqrt{V}^{-1}$  and  $g_{\text{eff}} \sim \sqrt{V}$ , the total coupling  $g_{\text{eff}}$  depends

on the filling factor in a volume-independent way:

$$g_{\text{eff}} = \frac{m_0}{\hbar} \sqrt{\mu_0 \hbar \omega_c \rho v / 4} \quad (5.2)$$

where  $\omega_c$  is the cavity frequency, and  $\rho$  is the spin density. As we can see, the coupling is independent of volume, and more strongly dependent upon  $\rho$ , the density.

### Ultimate limits

Weil gives the general sensitivity for an ESR spectrometer as [69]:

$$N_{\text{min}} = \frac{6\pi V_c k_b T_s}{\mu_0 g^2 \beta_e^2 S(S+1) Q_u} \frac{\Delta B}{B_r} \left( \frac{F k_b T_d b}{P_0} \right)^{1/2} \quad (5.3)$$

where  $V_c$  is the volume of the cavity,  $k_b$  is Boltzmann's constant,  $T_s$  is the temperature of the sample,  $\Delta B$  is the FWHM of the absorption line in gauss,  $B_r$  is the bias field,  $Q_u$  is the unloaded quality factor,  $T_d$  the noise temperature of our amplifier,  $b$  the bandwidth of the detection scheme,  $F$  is a dimensionless efficiency factor, and  $P_0$  the incident microwave power.

This derives from a model in which a linear voltage detector observes the absorption of power by the sample as it is tuned into resonance with the cavity. The quality factor  $Q$  of the cavity is (following [36]):

$$1/Q = 1/Q_u + 1/Q_\chi \quad (5.4)$$

where

$$Q_\chi = \frac{\int_{\text{cavity}} H_1^2 dV}{\chi'' \int_{\text{sample}} H_1^2 dV} \quad (5.5)$$

$$= \frac{1}{\chi'' \eta} \quad (5.6)$$

On resonance the change in quality factor is

$$\Delta Q = \chi'' \eta Q_u^2 \quad (5.7)$$

and for a critically coupled cavity in which the maximum power is dissipated in the sample,

Description	ESR Term	Equivalent cQED Term
Cavity and spin energy	$g\mu_B B_r$	$\hbar\omega_c$
Vacuum magnetic energy	$\frac{1}{2} \frac{B_0^2}{\mu_0} V_c$	$\frac{1}{4} \hbar\omega_c$
Saturation power	$P_0$	$\frac{\hbar\omega\gamma_2^* \kappa}{2g_s^2}$
Amplifier photon noise	$\frac{Fk_b T_d}{\hbar\omega_c}$	$N_{\text{amp}}$
Spin linewidth	$g\mu_B \Delta B/\hbar$	$\gamma_2^*$

**Table 5.1:** Equivalent terms of substitution for Weil's sensitivity equation

the fractional size of the detected voltage signal in transmission is

$$\Delta E_l = \frac{1}{8} \chi'' \eta Q_u E \quad (5.8)$$

where the drive power  $P_0 = \frac{E^2}{4R_0}$  is described by the incident voltage  $E$ , and we note that in the reflection scheme used by Weil, this is increased by a factor of 4. The sensitivity of the spectrometer is determined by the minimum resolvable absorption  $\chi''$ , limited by the noise temperature of the amplifier chain which produces

$$\Delta E_r = \sqrt{4RkT_d b} \quad (5.9)$$

after integration with bandwidth  $b$ . Finally, making several substitutions we find a suitable expression for circuit QED:

$$N_{\min} = \frac{6\pi}{s(s+1)} \left[ \tanh\left(\frac{\hbar\omega}{k_b T_s}\right) \right]^{-1} \left[ \frac{\sqrt{2\gamma_2^*}}{\gamma} \frac{1}{\sqrt{\frac{g_s^2}{\kappa} \tau}} \right] \sqrt{N_{\text{amp}}} \quad (5.10)$$

which, respectively, has terms for: the geometric multiplicity of the spin, the inverse spin polarization (expanded from the high-temperature approximation) affecting the contrast, the number of scattered photons in the integration time ( $\tau = 1/b$ ) due to the Purcell enhanced spin decay of a single spin, the fraction of the spin linewidth which is excited by the the drive and the number of photons  $N_{\text{amp}} = k_B T_d/\hbar\omega$  which must be scattered to achieve unity SNR.

Conventional ESR instruments have  $Q = 10^4$ ,  $g_s/2\pi \sim 0.02$  Hz with  $V_c = 10$   $\mu$ L) and  $T_K = 30,000$  K. With a limiting saturation power of  $P_s \sim 100$  mW, they are regularly operated down to temperatures of 1 K and can detect  $N_{\min} \sim 10^9 \sqrt{\text{Hz}}$ . With our current devices, we may reasonably achieve  $Q = 5000$ ,  $g_s/2\pi = 20$  Hz with  $V_c = 10$  nL, and  $T_N \sim 10$  K at

temperatures from 4 K to 20 mK. Depending upon the spin linewidths, this currently allows  $N_{\min} \sim 10^4 \sqrt{Hz}$ , and with further development (including the application of standard ESR techniques such as field modulation), it should be possible to detect a single spin after a reasonable integration time.

Although the detection of a single spin is an admirable goal, in quantum information processing we must be able to perform operations at the speed of our slowest component. Superconducting qubits typically have a coherence time of 1 – 100  $\mu$ s, and swap operations between a spin and a resonator occur at the rate  $g_{\text{eff}}$ , necessitating a coupling of many MHz. In the remainder of the chapter we utilize the extreme sensitivity of our devices to instead study larger ensembles of approximately  $\sim 10^{12}$  spins at large coupling rates more suitable for future use.

## 5.2 ESR of DPPH

We first discuss DPPH, or diphenyl-picryl-hydrazyl an organic radical with a simple Hamiltonian:

$$H_d = -m_0 \vec{B} \cdot \vec{S} \quad (5.11)$$

Every molecule of DPPH comprises a bound paramagnetic spin, with a  $g$  factor slightly modified to be 2.0036 at room temperature. This gives a Zeeman splitting equal to  $\hbar\omega = g\mu_B B$  increasing at approximately 2.9 MHz / gauss and  $\mu_B$  the Bohr magneton. Hence, for a magnetic field of around 2 kG, we expect it to be absorptive at microwave frequencies. Its natural linewidth is a few gauss (4-14 MHz) depending on the solvent it crystalizes from and it is a superb standard for many assays in ESR. It is typically prepared in successively diluted solutions in order to be used for magnetic field and spin number calibration.

We cooled down a sample of DPPH on chip J2 first in a Cryoconcept Dilution Fridge to 10 mK, on resonators previously known to have high internal quality factor (See Figure 5.16). By tracking its resonance dip in the feedline transmission, we were able to detect the approximate magnetic field to current ratio at the sample (see Figure 5.3).

## Power Absorption

We begin to saturate a single spin when the drive Rabi frequency equals the natural spin linewidth,  $\Omega_r = \gamma$ , with:

$$\Omega_r = 2g_s \sqrt{\frac{2P}{\omega \hbar \omega}} \quad (5.12)$$

where  $\gamma = \sqrt{2\gamma_1\gamma_2^*}$ ,  $\gamma_1$  the spin energy relaxation rate and  $\gamma_2^*$  the dephasing rate. A sufficient power to eliminate spin polarization is then:

$$P_{\text{sat}} = \frac{\gamma_1\gamma_2^*\omega^2\hbar}{4g_s^2} \quad (5.13)$$

and for spin resonances as wide as 100 MHz requires a watt, which is unreasonable in cryogenic experiments. A more modest nanowatt would saturate a 6 kHz linewidth transition, exciting only  $\Omega_r^2/\gamma^2 = 10^{-9}$ , or one part in a billion of the more incoherent spin. Inside a cavity, we have instead a finite  $\kappa$ , which significantly limits the necessary power after enhancing the Rabi rate by a factor of  $\sqrt{Q}$ .

An ensemble of spins interacts with the field with the enhanced coupling  $g_{\text{eff}} = g_s\sqrt{M}$ , giving a dip in feedline power transmission from which we can estimate the number of spins:

$$P_{\text{in}}(1 - S_{21}^{\text{min}}) = \frac{\Omega_r^2}{\gamma^2} \hbar \omega \gamma_1 \quad (5.14)$$

$$= \frac{(2g)^2 \left(\frac{2P}{\omega \hbar \omega}\right)}{2\gamma_1\gamma_2} M \hbar \omega \gamma_1 \quad (5.15)$$

$$(5.16)$$

By fitting the frequency linecuts as a pseudo shunt resonator, where on resonance (see Ch 2):

$$Q_c = \frac{Q}{1 - S_{21}^{\text{min}}} \quad (5.17)$$

$$Q_i = \frac{Q}{S_{21}^{\text{min}}} \quad (5.18)$$

We can retrieve the number of spins by equating with the Purcell enhanced rate of energy

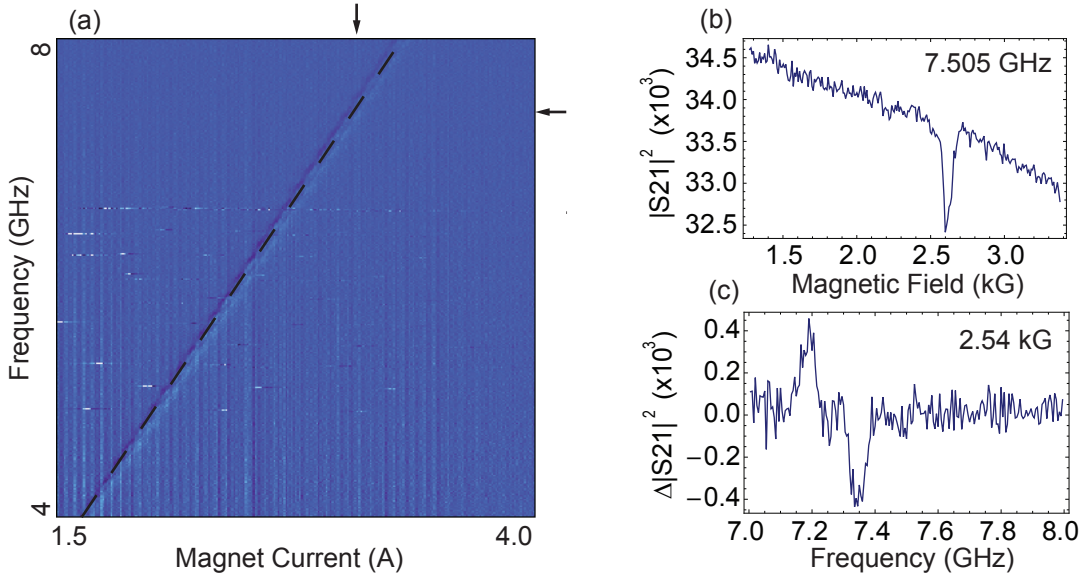


**Figure 5.3:** (a) Microwave transmission through a coplanar device covered with DPPH. The spins absorb power when tuned into resonance via the bias magnetic field. The slope of the absorption line gives our conversion from current in our persisting superconducting magnet of 0.844 kG / Ampere for the Kelvinox and 0.330 kG / Ampere in the Cryoconcept. (b) a linecut at 7.5 GHz, where there is a dip of  $\sim 1\%$  in transmission. There are approximately  $10^{13}$  spins, with a FWHM of 150 MHz. (c) A linecut at constant magnetic field of 2.54 kG, with the subtraction of a nearby trace.

loss  $\frac{g^2}{\gamma}$ :

$$M \approx \frac{\omega^2}{g^2 Q_c} \quad (5.19)$$

$$\gamma = \omega / Q_i \quad (5.20)$$

The strength of the absorption suggested a number of spins  $\sim 3 \times 10^{12}$ , consistent with the deposited density. This number of spins  $\sim 10^{13}$  over a mode volume of  $1\text{mm} \times 10\mu\text{m}^2$  yields a density of  $10^{21} \text{cm}^{-3}$ , on the high end of commonly found substrate doping rates. While well-behaved at room temperature, DPPH undergoes a phase transition at cryogenic temperatures and becomes antiferromagnetic [70], with a linewidth that can be hundreds of MHz wide. We measured a total linewidth of around 180 MHz, with precision limited by experimental details of the fridge and wiring, such as reflections and the long experiment duration.

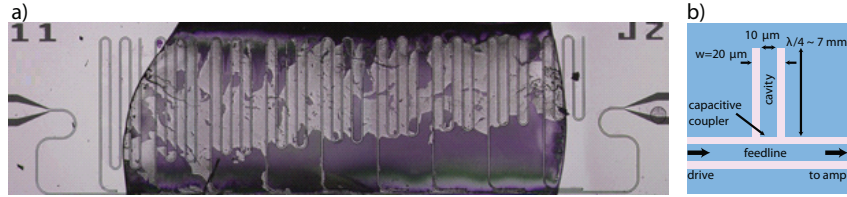


**Figure 5.4:** a) Optical picture of DPPH chip. We used toluene to dissolve 38 g of DPPH into 10 ml of solvent, then placed 2 drops (approximately 0.2 ml) on the chip. At an area of  $10\mu\text{m} \times 10\mu\text{m} \times 1\text{cm}$ , we estimate a spin density of  $\approx 10^{19}/\text{cm}^2$  within the actual mode volume. b) Diagram of shunt resonator, including a  $\lambda/4$  resonator terminated by a superconducting short. The capacitive coupler sets the coupling Q of the resonator.

## Resonant Interaction

In addition to a feedline interaction, the DPPH covered several CPW resonators, leading to a resonant interaction and hybridization that allowed power to be transferred into the spin ensemble at a large rate. In the accompanying Fig. 5.5, we see transmission through the feedline in a window about the few lowest frequency CPW resonators. Because of the large spin coupling  $g_{\text{eff}}$  and damping rate  $\gamma$ , the quality factor of the CPW resonators is depressed off-resonance, while there is a splitting of  $2g$  in the frequency of the two hybridized oscillators, at resonance. At a field of 2 kG, the resonator Q has begun to diminish, therefore here we fit only the frequency repulsion, using the equations for hybridization discussed in Ch. 3, where the two resonant frequencies are:

$$f_{\pm}[B] = \frac{1}{2}f_r[B] + f_{DPPH}[B] \pm \sqrt{(f_r[B] - f_{DPPH}[B])^2 + 4g^2} \quad (5.21)$$

and allowing for the reduction of resonator frequency due to kinetic inductance.

Using our estimated  $g_s = 20$  Hz/spin, this gives  $M \sim 10^{12}$ , on the same order as the number in the feedline. Our experiments with DPPH were a first proof of principle: using an EPR standard, we could apply sufficient magnetic field to our devices to tune spins into resonance with our superconducting cavities, and approach a high enough  $g$  to make qubit operations feasible. In addition, they demonstrate the viability of depositing small samples on top of our CPW resonators for ESR detection and investigation.

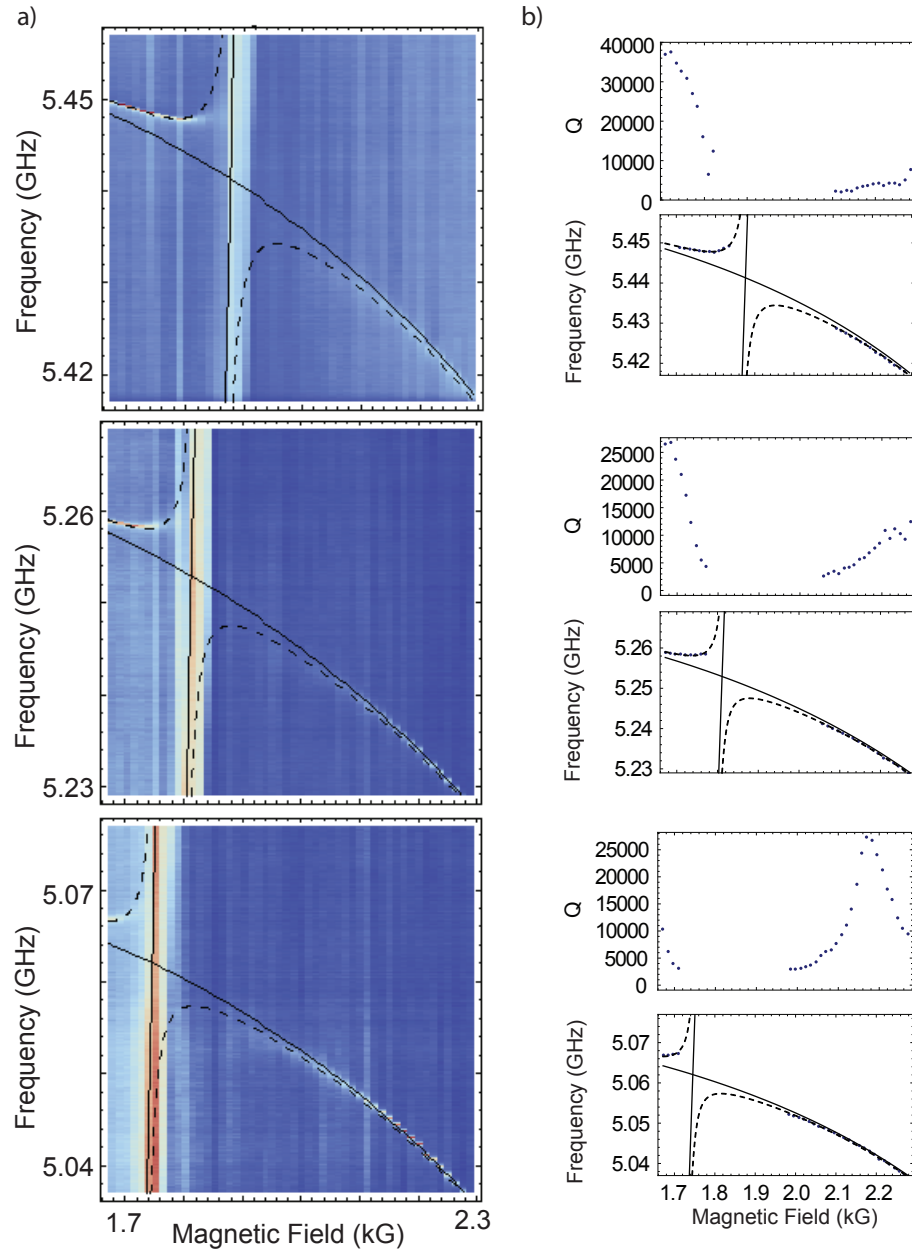


**Figure 5.5:** (a) Resonances with 3 shunt resonators, shown in transmission amplitude. The resonator can be seen in a curved arc induced by the extra kinetic inductance which is provided by a larger parallel bias field; the dark red dip is not repelled, and represents a distinct ensemble of spins in the feedline which does not interact with the superconducting resonator, while a similar sized ensemble hybridizes with the superconducting resonator. (b) Frequency and quality factor of the resonators, along with theory curves.

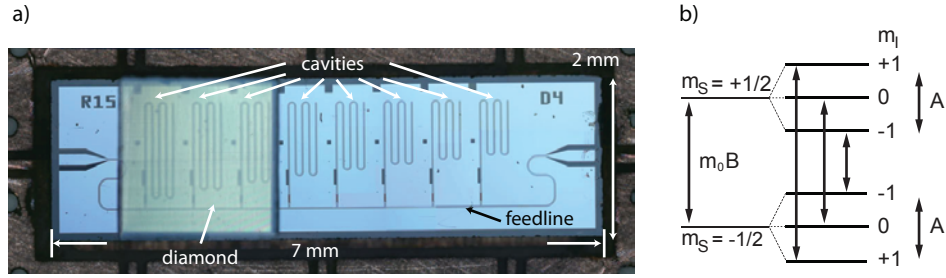


**Figure 5.6:** a) An image of a diamond chip on a sapphire chip fabricated with 8 coplanar waveguide resonators. b) the diamond P1 center energy levels

### 5.3 ESR of Diamond

As another approach we used well-studied nitrogen substitution defects in a diamond crystal lattice. These P1 centers have a Hamiltonian, detailed in Fig. 5.6b:

$$H_d = -m_{0,d}\vec{B} \cdot \vec{S} + A\vec{S} \cdot \vec{I} \quad (5.22)$$

with a hyperfine coupling tensor  $A/2\pi = (81.33, 81.33, 114.03)$  MHz and  $m_{0,d}/2\pi = 2.804$  MHz/gauss. Here the  $\hat{z}$  direction corresponds to the diamond  $\langle 111 \rangle$  axis,  $\vec{S}$  is the electron spin-1/2 operator and  $\vec{I}$  is the spin-1 operator for the nucleus.

The spins in diamond act as several different ensembles of nearly-free electron spins, with the addition of the hyperfine splitting, and thus requires magnetic fields on the order of  $\sim 2$  kG to reach a transition frequency of  $\sim 6$  GHz. It is distinguished from DPPH in the sense that its defects or spins are organized in a rigid lattice, and has been of great historical interest in ESR [71]. We studied two samples with nitrogen substitutions, or P1 centers\*, both mounted on top of a sapphire chip with lithographically fabricated niobium CPW resonators.

The first sample of diamond was synthetically grown in a high-pressure nitrogen atmosphere and was acquired from the Awschalom group at UCSB. Feedline absorption of  $\sim 3\%$  and  $\gamma = 20$  MHz suggested an ensemble of  $1.9 \times 10^{12}$  spins, confirming a density of  $\approx 10^{19} - 10^{20}/\text{cm}^3$  nitrogen substitution P1 centers, and featured three clear absorption lines corresponding to the hyperfine splitting, observable in Fig. 5.8 for example.

We tune spins into resonance with cavity to observe the hyperfine splitting in Fig. 5.7. Because there are in fact different spin ensembles which hybridize separately with the resonator

\* “Color” centers in diamond were originally named after the first letter of the laboratory where they were discovered, followed by the order of identification.

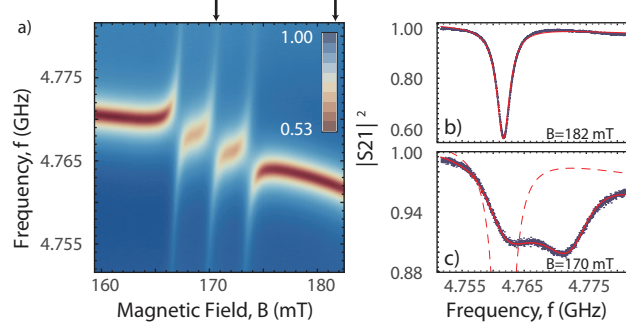


**Figure 5.7:** a) Diamond P1 spins in resonance with a hanger, measured through transmission of our waveguide chips. b) a linecut with constant bias field, far from resonance c) a linecut at constant bias field at the point of  $m_I = 0$  hybridization with the cavity.

Line	$f$ (GHz)	$g/2\pi$ (MHz)	$\gamma/2\pi$ (MHz)
$m_I = -1$	5.121	7.5	21.5
$m_I = 0$	5.325	8.2	20.0
$m_I = 1$	5.509	9.8	22.2

**Table 5.2:** Coupling strengths  $g$  for ensembles with different  $m_I$  in Fig. 5.7

(differentiated by the nuclear spin and orientation), the total microwave probe transmission is described by using the input-output theory (see Appendix):

$$|S_{21}|^2 = \left[ 1 + \kappa_c \left( \frac{1}{i\Delta_c - (\kappa_c + \kappa_i) + \sum_I \frac{|g_I|^2}{i\Delta_I - \gamma/2}} \right) \right]^2 \quad (5.23)$$

where  $\Delta_c = \omega - \omega_c$  the frequency detuning between the probe and bare cavity frequency,  $\kappa_i$  and  $\kappa_c$  are the internal and coupled cavity decay rates,  $\gamma$  is the spin linewidth, and  $\Delta_I = \omega - \omega_{m_I}$ , is the probe detuning from the  $m_I$  hyperfine transition. For saturation and transmission measurements, we neglect the inhomogeneity of  $g_s$ , which is more important for pulsed experiments.

For our sample however, because  $g/A \sim 1$  the full equation is of limited use. From a global fit we find  $g_{\text{eff}}/2\pi \sim 8$  MHz and  $\gamma_2^*/2\pi \sim 20$  MHz listed in Table 5.2 using the approximation that only a single ensemble at a time interacts with the resonator. This gives the spin-ensemble a cooperativity of  $C = 1.6$ , limited here by dipolar broadening (see Section 5.5).

In Fig. 5.8, it is clear we have allowed only one or two resonators to interact with the spins.

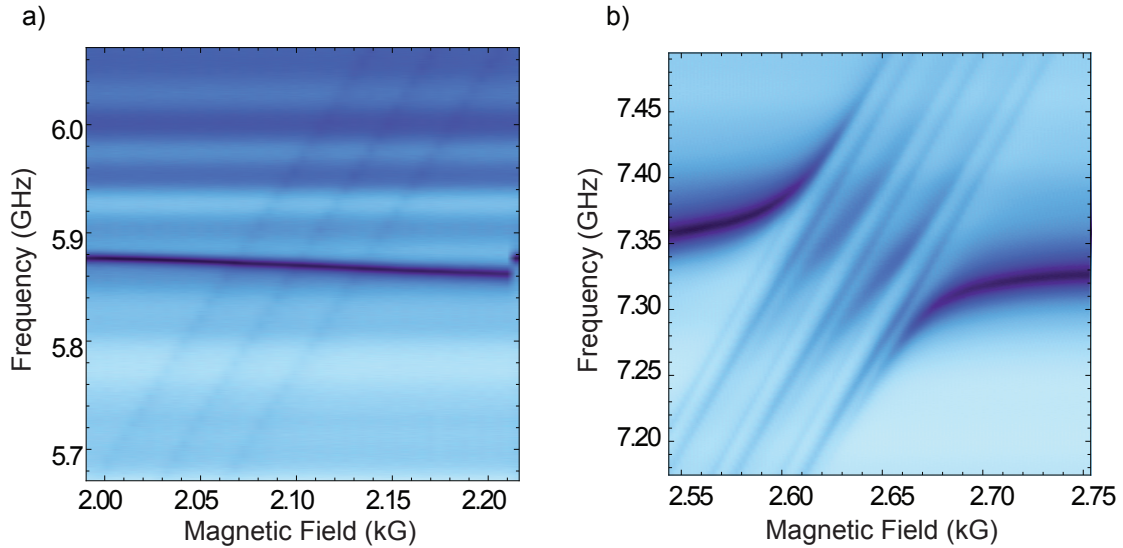


**Figure 5.8:** a) A superconducting CPW resonator whose mode volume does not intersect with the diamond, superimposed upon the feedline absorption of all three hyperfine ensembles. b) The anti-crossing of a box mode of the sample holder with a large number of bulk diamond P1 spins, also superimposed upon the feedline absorption.

This is observed as the spin resonant frequency crosses that of a CPW resonator (uncovered by the diamond chip) without any size anti-crossing or hybridization. Coplanar waveguide localizes the excitation field to within 10's of microns from the chip surface, but box modes of the sample holder involve a much larger volume and may confound this!

### Saturation experiments

We used an alternate sample obtained from Apollo Diamond to investigate the energy decay and dissipation properties of P1 centers.

Although typically when  $10^{12}$  spins are used for collective coupling as a harmonic oscillator only a small fraction are excited, we examined this sample's saturation power and its characteristic return to polarization afterwards. In the figure above, we saturated the middle transition, probing the  $m_I = 0$  transition after placing it in resonance with the cavity. An exponential fit gave a time constant  $\tau \sim 4$  s for the return of polarization to the spin ensemble. A followup experiment might have saturated the spins using one resonator while probing another, or measured one of the satellite peaks which is distinct in frequency from nearby spin defects with  $g \approx 2$ .

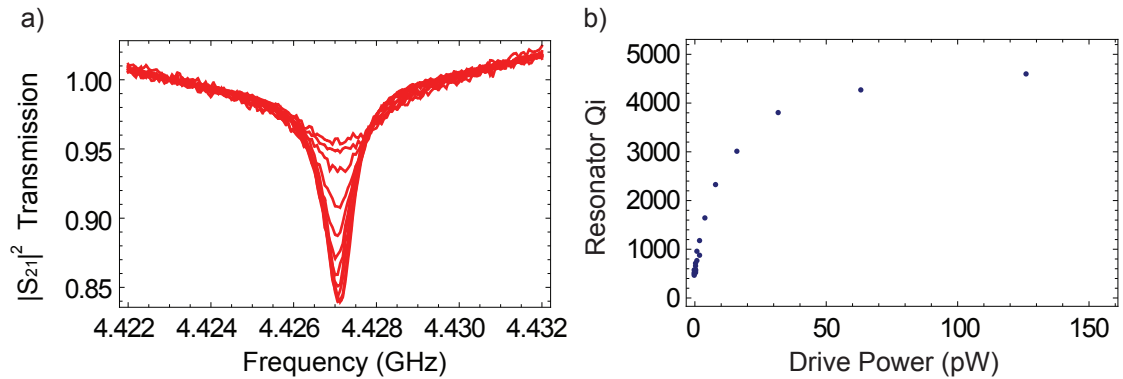


**Figure 5.9:** a) When driven, spins on resonance with the cavity become polarized and cease damping the cavity internal quality. b) The power required for spin saturation is consistent with a  $1/\gamma_1 \sim 1$  s and our time domain measurement of P1 center energy relaxation.

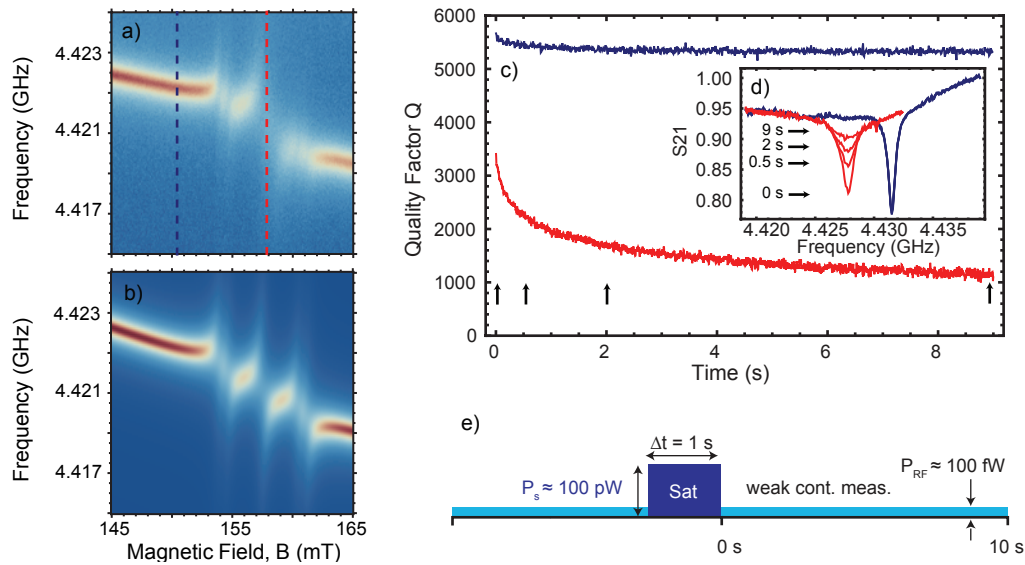


**Figure 5.10:** a) This device was mounted with the bias field tilted from the [111] axis, and its hyperfine splitting demonstrates the anisotropic properties the diamond Hamiltonian. Although difficult to fit analytically, the data is consistent with  $g$  for satellite peaks of 3.5 MHz, 5 MHz for the central peak, and 30 MHz linewidths. b) Theory simulation to match the estimated parameters. c) we apply a large saturation pulse, and then probe the cavity with which it is in resonance. At a time  $\tau$  after the saturation, we see that the  $Q$  of the cavity is damped due to the return of spin polarization. The recovery time is several seconds, even at the enhanced Purcell rate. This time constant matches approximately the spin  $\gamma_1$  obtained from cw saturation of the spins.

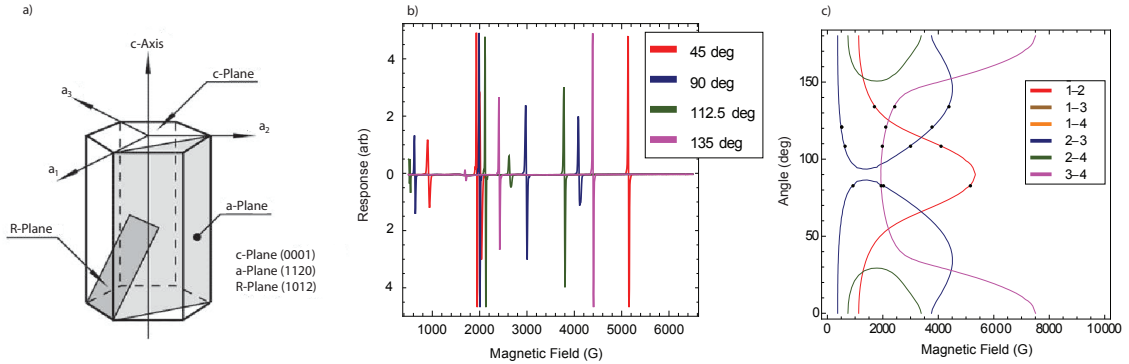


**Figure 5.11:** a) The crystal structure of sapphire allows three different cleaving planes, which produces an anisotropic dielectric constant. Each vertex in the lattice is occupied by an aluminum atom, which has a nuclear spin  $I=5/2$ . The angle of  $B_{\text{bias}}$  from the  $\hat{c}$  axis defines the energy levels. b) An ESR spectrum of our ruby wafers, done by collaborators at Oxford University. c) An iso-frequency plot of the resonances of ruby, matching the resonances in the ESR scan.

Saturation experiments can tell us about the  $\gamma_1$  or energy relaxation of the spins according to Eqn. 5.2, which is not necessarily related to the  $\gamma_2^*$  linewidth. In fact subsequent work by former colleagues [?] has validated these values, using a dispersive technique. In these experiments, the spins are pumped while off-resonant from the cavity, whose frequency is repelled as the polarization returns.

## 5.4 ESR of Ruby

Ruby is sapphire doped with  $\text{Cr}^{3+}$  ions, leading to a crystal with effective spin-3/2 magnetic spins within its matrix. In addition, the substrate creates a finite crystal field, such that even with no applied magnetic field the spins have energy levels separated by  $\hbar\omega$  in the microwave regime. The Hamiltonian is:

$$H_r = -m_{0,r}B \cdot \hat{S} - D(\hat{S}_z^2 - 5/4) \quad (5.24)$$

where  $m_0/2\pi = 2.7811$  MHz/gauss,  $\hat{S}$  is the spin-3/2 operator,  $z$  is defined along the  $\hat{c}$  crystal axis, and  $2D/2\pi = 11.46$  GHz is the crystal field splitting that separates  $S_z = \pm 3/2$  levels from  $S_z = \pm 1/2$  even with no external field  $B$  applied.

We obtained a sample with high doping  $\sim 10^{19-20} \text{cm}^{-3}$ , and fabricated resonators on top in our standard sapphire process. Applying  $B_{\text{bias}}$  we spectroscopically measured Hamiltonian

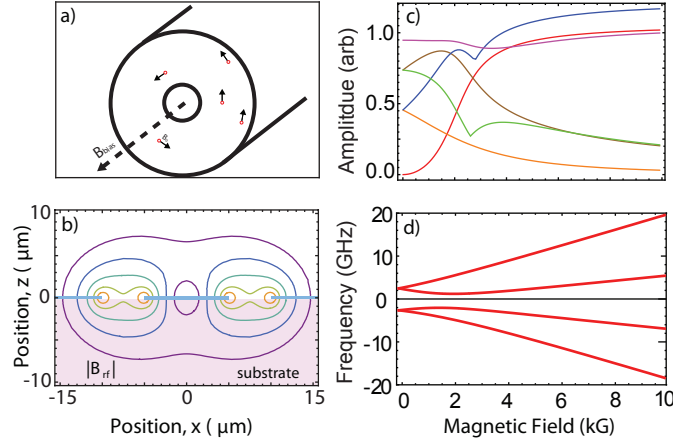


**Figure 5.12:** a) In a coax,  $B_0$  is always perpendicular to an axial  $B_{\text{bias}}$ . However, the strength of the zero-point field  $B_0$  varies with distance from the center-pin. b) Coplanar waveguide, while similar to coax does not have the same symmetric geometry, and  $B_0$ ,  $B_{\text{bias}}$  are often non-orthogonal. c) The rough transition strength proportions for ruby at  $\theta = 45$  deg, proportional to  $|\langle \psi_f | S_x^2 + S_y^2 + S_z^2 | \psi_i \rangle|^2$  d) The energy levels of ruby at  $\theta = 67$  deg, showing hybridization of the  $|J = 3/2\rangle$  (lower) and  $|J = 1/2\rangle$  (upper) levels.

transition lines due solely to their absorption in the feedline of the coplanar waveguide chips, using a standard network analyzer. Power absorption of about 5%, indicated approximately  $10^{13}$  spins interacting with the feedline for a concentration of  $\approx 10^{20}/\text{cm}^3$ . Having such a high concentration maximizes  $g_{\text{eff}}$ , but also increases the dipolar energy of the nearest neighbor, causing a broader linewidth (see Sect. 5.5).

For a magnetic field applied at an angle with respect to  $\hat{c}$ , the levels mix and allow transitions between the  $|J = 3/2\rangle$  and  $|J = 1/2\rangle$  spin states. From the Figure above, we see the transmission in a ruby chip, which shows an array of spin transitions over a wide band of frequency and bias field, with an angle  $\theta = 67$  deg from  $\hat{c}$ .

Transition strength varies, reflecting a small contrast due to either a smaller population difference or diminished transition rates due to selection rules. For a thermalized ruby crystal, the population difference between two levels  $i, j$  is:

$$\Delta_{ij}(T) = \frac{\exp(-\hbar\omega_i/k_b T) - \exp(-\hbar\omega_j/k_b T)}{\sum_k \exp(-\hbar\omega_k/k_b T)}. \quad (5.25)$$

Because of the meanders of the CPW resonator and the non-uniform direction of  $B_0$ , we might approximate the absorption amplitude to be proportional to the average of matrix element

transition rates though the exact absorption could be calculated numerically. The variation of local  $g_s$  complicates the usage of the ensemble beyond the low-excitation limit, such as with a Hahn echo, as the effective  $g$  changes according to the location of each individual spin.

In early experiments with a ruby chip it was difficult to determine the crystal orientation of the sample by using multiple transitions as reference points. Additional data including those shown in Fig. 5.13 improved with evolving microwave equipment (a high-end VNA) which contributed to the better visibility of transitions. Within the broadband scan are resonances with the  $\lambda/4$  and  $3\lambda/4$  modes of the superconducting waveguide cavities (the thin lines shown in the Figure). In addition, we observe large resonances with bulk spin collections in the box modes of the cavity.

In Fig. 5.13, we observe the 1 – 4 transition as it interacts with the second mode of a superconducting shunt resonator at 14.35 GHz. According to the hybridization equations from Ch. 3, the resonator  $Q$  is:

$$Q = \frac{\Delta^2 + \gamma_2^2}{2g_{s,\text{eff}}^2\gamma_2 + \kappa(\Delta^2 + \gamma_2^2)} \quad (5.26)$$

from which we extract an effective coupling rate for spin  $g_{s,\text{eff}} = 38$  MHz, with linewidth  $\gamma_2/2\pi = 96$  MHz primarily due to hyperfine interactions with  $^{27}\text{Al}$  nuclear spins in the sapphire substrate. Like the diamond sample, the ruby experiences dipolar broadening as well, except that in this case it can be substantially from the  $^{27}\text{Al}$  nuclear spins which comprise the substrate, instead of the Cr dopants. The ruby broadening paper gives a linewidth of 10-12 G.

The largest cooperativity is achieved (see Fig. 5.13b) with a harmonic of one of the coplanar waveguide resonators, with a cavity linewidth of  $\kappa = 1.3$  MHz, giving

$$C = g^2/\kappa\gamma_2^* \approx 11.5 \quad (5.27)$$

As a measure of measure of the coupling strength between two oscillators in cavity QED, a  $C > 1$  indicates the spins have reached the threshold of utility in cavity QED. The coupling here is strong in the sense that nearly every photon entering the cavity is coherently transferred into the spins. Unfortunately, because of the the large spin linewidth, it is too difficult to retrieve the excitation before it decays, and future work must focus on preparing a substrate that itself does not induce broadened transitions due to the excessive or random influence of nuclear spins.

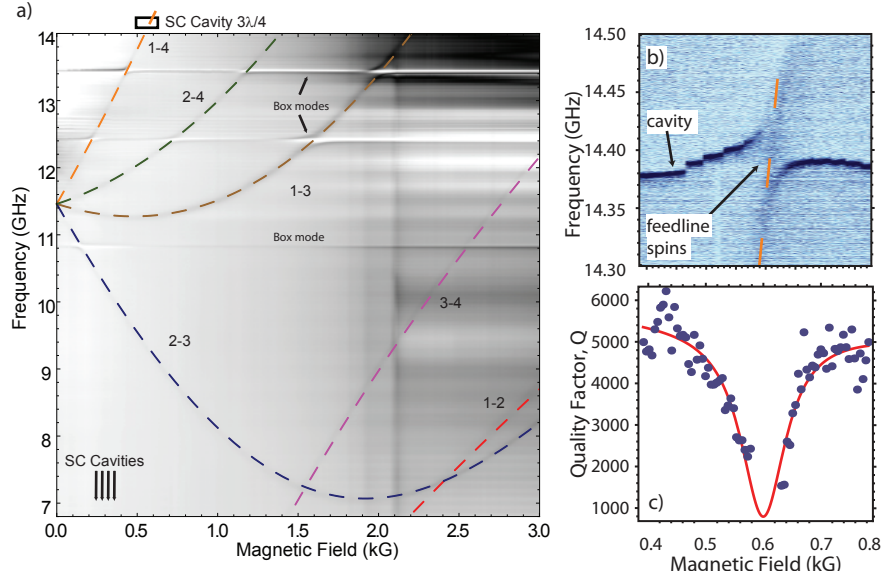


**Figure 5.13:** a) The broadband transitions of ruby, measured through transmission of our coplanar waveguide on a ruby chip. b) a closeup of the anti-crossing of the spins with the  $3\lambda/4$  mode of one of our superconducting resonators. c) the quality factor as it is damped by the resonant spins.

## 5.5 Considerations for Future Work

### Dipolar Broadening

There are two possible goals for future work with spins in cQED systems. First is the engineering of suitable spin species to rival the coherence times of electromagnetic cavities, for integration with our qubit experiments. This will require a precise control over the substrate and its impurities, as well as the introduction of the spins themselves.

The random distribution of spins in the crystal leads to a natural broadening of the Larmor transition frequency. Following Kittel and Van Vleck [72], the second moment from summing over every possible defect vertex  $k$  of the crystal from an occupied site  $j$  separated by  $\vec{r}_{jk}$  is:

$$\langle \Delta\nu^2 \rangle = [S(S+1)/3h^2]f \sum_k B_{jk}^2 \quad (5.28)$$

$$B_{jk} = -3g^2\mu_B^2r_{jk}^{-3} \left[ \frac{3}{2} \cos(\theta_{jk})^2 - \frac{1}{2} \right] \quad (5.29)$$

where  $\theta_{jk}$  is the angle between  $\vec{r}_{jk}$  and the bias field,  $g$  is the spin's g-factor,  $\mu_B$  is the Bohr

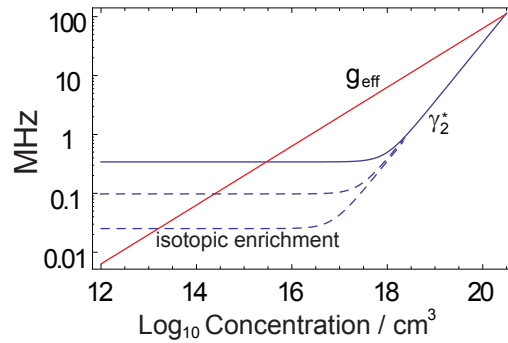


**Figure 5.14:** (a) Calculate  $g$  and  $\gamma$  for P1 centers in diamond, for the nominal mode volume of a coplanar waveguide  $10\mu\text{m} \times 10\mu\text{m} \times 1\text{cm}$  for a diamond powder (disregarding crystal angle). (b) The maximum  $g_{\text{eff}}/\gamma$  depends on the limitations of residual nuclear spins.

magneton,  $h$  is Planck's constant,  $f$  is the probability of a lattice site being occupied, and we sum over all lattice sites.

For single crystal diamond there is a term of order one with respect to the average angle between occupied lattice points and the bias magnetic field, and in all cases  $f < 0.1$  the lineshape is Lorentzian with width proportional to concentration. In addition, a contribution from  $^{13}\text{C}$  nuclei whose natural abundance of 1.1% limits the floor of  $\gamma_2^*$  due to dipolar broadening from the random nuclear spin environment. When the nuclei are removed from consideration (see Figure 5.14), the maximum  $g/\gamma$  is of course obtained for a single spin, otherwise this background determines the maximum ratio. For diamond P1 centers, the optimum without isotopic enrichment is on the order of  $N_e = 10^{18}/\text{cm}^3$ .

Many articles report coherence times for spin samples that can be many milliseconds. However these reports primarily measure  $T_{2E} = 1/\gamma_2$ , the decoherence time with a Hahn echo pulse, where nuclear spin effects are nullified. Researchers looking for a useful species must be careful when sifting through the literature. A Hahn echo pulse no longer draws from the collective enhancement of  $g$  for spins. Thus, instead of relying on  $10^{12}$  spins for a  $10^6$  enhancement of the Rabi rate, we must use an extra  $10^{12}$  photons, which is often an unreasonable amount of power in cryogenic experiments (although it has been done [73]).

### Field inhomogeneity

Because most of our spin systems were limited by dipolar broadening, we can only put an upper limit on the field homogeneity in the vicinity of the spin ensembles. Typically there

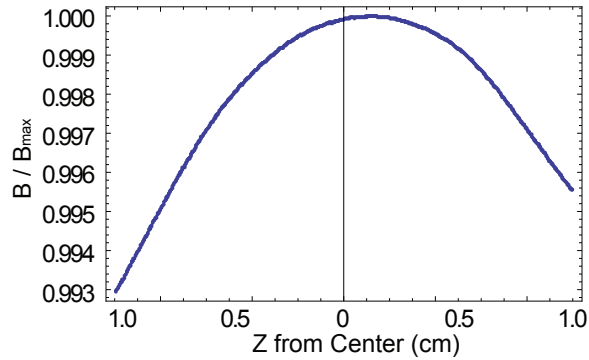


**Figure 5.15:** Field homogeneity near the sweet spot of the superconducting magnet in our Kelvinox fridge, from original documentation.

are concerns that, due to the partial Meissner effect of thin-film superconductors or the presence of a cancellation coil in our persistent magnet, there might be a gradient  $\Delta B$  which smears the spin across some linewidth  $\gamma_B$ . As the smallest linewidth we have measured would limit inhomogeneity to  $\Delta B = 5.5$  G across a distance 1 cm, however, there is no reason yet to suspect that this is occurring. With the present magnets field profiles, we expect a worst case spread of  $\approx 0.4\%$ , for the feedline chip oriented along the bias field, reduced by an order of magnitude for a shunt resonator, and perhaps another if we abandon meanders used to shorten resonators. This would begin to limit experiments with  $g = 2$  spins and the current magnet to linewidths of a few hundred kilohertz. In addition, the superconducting film of our resonators could distort the bias magnetic field through the Meissner effect; this is not too troubling, because it produces only a static difference in bias field, or an inhomogeneous line broadening that can be corrected with an echo pulse.

## Resonator Quality

Our coplanar waveguide resonators are made of thin-film superconducting niobium. This has the advantage of allowing quality factors up to  $10^6$  at high powers. It has the disadvantage of distorting the magnetic field due to the Meissner effect, and being sensitive to the applied bias magnetic field. However, as a thin film, its sensitivity to field applied in-plane is reduced, and the major effect is a downward pull in frequency due to increased kinetic inductance, seen in Fig 5.16.

The magnetic field applied to our CPW resonators increases the energy stored in the supercurrents of the resonators by increasing the penetration depth  $\lambda$  and increasing the supercurrent density. This leads to a change in frequency proportional to  $\alpha$  the kinetic

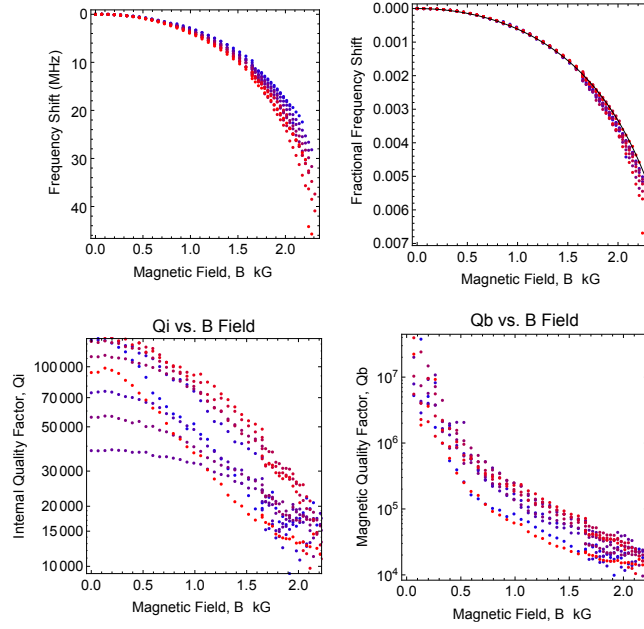


**Figure 5.16:** (a) Behavior of niobium coplanar waveguide resonators in the presence of an applied magnetic field. a) Frequency shift, in MHz for a typical array of  $\lambda/4$  shunt resonators. b) Fractional frequency shift, demonstrating the magnitude of the kinetic inductance fraction  $\alpha = (1.2 \pm 0.3) \times 10^{-3}$  and  $B_c = 3.2 \pm 0.3$  kG c) Internal quality factors. Without extreme measures or a vector-axis magnet, our resonators still retain  $Q_i > 10000$  in 2 kG field. d) The extracted quality factor  $Q_b$  due to magnetic losses.

inductance fraction:

$$f_r[B] = f_0 \left( 1 - \alpha \frac{1}{1 - \left(\frac{B}{B_c}\right)^2} \right) \quad (5.30)$$

where  $f_0$  is the zero-field frequency, and  $L_k \approx L_i$  for some  $B_c$  field amount. For low values of magnetic field our resonators have constant frequency but they acquire a quadratic pull at higher fields as seen in the Figure 5.5 anti-crossings.

Other groups have studied the use of different films for the purpose of limiting loss in low magnetic field, and in our specific application of high parallel field [? ].

## 5.6 Outlook

We have demonstrated the coupling of several different spin species, fabricated in distinct ways, showing the robustness of our coplanar waveguide cavities as a platform for broadband

Element	Spinless Isotope	N.A.	Contaminants
Helium	$^4\text{He}$	> 99%	$^3\text{He}$ (trace)
Carbon	$^{12}\text{C}$	99%	$^{13}\text{C}$ (1%)
Neon	$^{20}\text{Ne}, ^{22}\text{Ne}$	> 99%	$^{21}\text{Ne}$ (0.3%)
Silicon	$^{28}\text{Si}, ^{30}\text{Si}$	95%	$^{29}\text{Si}$ (5%)
Argon	$^{40}\text{Ar}$	> 99%	$^{39}\text{Ar}$ (trace)
Uranium	$^{238}\text{U}$	99%	$^{235}\text{U}$ (< 1%)

**Table 5.3:** A table of the isotopes of select elements which are naturally uncontaminated with nuclear spins (or with potential for enrichment) and their natural abundances.

ESR of picoliter samples, at millikelvin temperatures and attowatt powers. The coupling is strong enough to exceed all qubit and cavity decay rates, leaving open to possibility for future use in a quantum memory.

ESR at millikelvin temperatures is extraordinarily promising, perhaps even too good to be true – some spins have inconveniently long  $T_1$  times requiring infinitesimal excitation powers to avoid saturating them (or optical pumping to reset). While inhomogeneous broadening from nuclear spins threatens to disrupt any coherence advantage that may have been conferred by the crystal structure, isotopic enrichment is being employed more regularly in industry, increasing availability for researchers. Although the possibility of correcting inhomogeneous broadening by Hahn echo is tantalizing (nuclear spin relaxation rates at millikelvin temperatures may be immeasurably long), it would require pulses with an extremely large amount of energy, a factor of  $\sim 10^{12}$  larger than similar pulses on a superconducting qubit. With careful attention to blanking and repetition rates, these might be viable in a special dilution fridge, but a more tractable first approach is simply to isotopically enrich the substrate material to ensure there are no nuclear spins. In fact this plan is being executed in the leading room-temperature spin experiments, has been enacted in the past using the naturally spin-free noble gasses [74], and experiments in progress benefit from the absence of  $^3\text{He}$  in experiments with electrons on superfluid Helium. See Table 5.3 for a summary of specific elements with a natural abundances (N.A.) of isotopes lacking nuclear spin.

The pace of research in diamond in particular has been particularly impressive, with single spins at room temperature having extraordinary coherence times, especially when removed from the influence of  $^{13}\text{C}$  nuclear spins. Several groups [16, 75–77] have been investigating spins optically at room temperature and more recently at convenient liquid nitrogen temperatures, where individual electron and nuclear spins have been manipulated.

In addition our collaborators, at Oxford, have continued to push the boundaries of

coherent ensembles without superconducting cavities, studying exotic species like N@C<sub>60</sub> [78] as well as rare-earth ions and Bismuth. Several groups have employed isotopically enriched substrates, obtaining nearly inconveniently long coherence times for simple phosphorus doped silicon [66]. Meanwhile, additional work (much by former colleagues) continues at other institutions to integrate special diamond defects like the Nitrogen Vacancy (NV) centers (which have a useful zero-field splitting), with cavity QED systems. Kubo et. al have begun to bridge the gap between ESR and cQED [23, 79], using a superconducting qubit for spin detection, doing swap operations between a superconducting qubit, cavity and the spin ensemble. The use of ensembles complicates pulse protocols [80], but the wealth of knowledge in related fields encourages creative application in this new frontier.

## CHAPTER 6

---

### 3D Transmon

---

THE transmon has had tremendous success in allowing the design and execution of quantum algorithm experiments [19, 81]. In Ch. 3 we saw its simple coupling to a cavity permits easy simulation and design of devices including the participation of many modes and their sharing of the Josephson junction-derived anharmonicity. The 3D transmon was created to exploit this simplicity, turning the sample holder itself into the resonant cavity and the input/output coaxial lines into probes. In Ch. 2 we examined the sources of dissipation which could influence the spontaneous decay of our transmon, and concluded that a rectangular waveguide cavity might offer several practical ways to limit dissipation and control coupling to the environment. The simplicity, combined with minimization of surface dissipation, narrowed the field of suspect components in modern superconducting qubits, and it instantly provided an increase in coherence over planar designs.

In this Chapter, we detail the implementation of the transmon in a 3D rectangular waveguide cavity [82]. We first report design considerations for the cavity and qubit, and then describe the experiments used to characterize qubit performance, including pulsed measurements of qubit and cavity excited state populations. Finally, we give an account of the first fabricated 3D transmon qubits and their properties. The electrode antenna length must be increased from the scale of  $10\ \mu\text{m}$  to 1 mm.

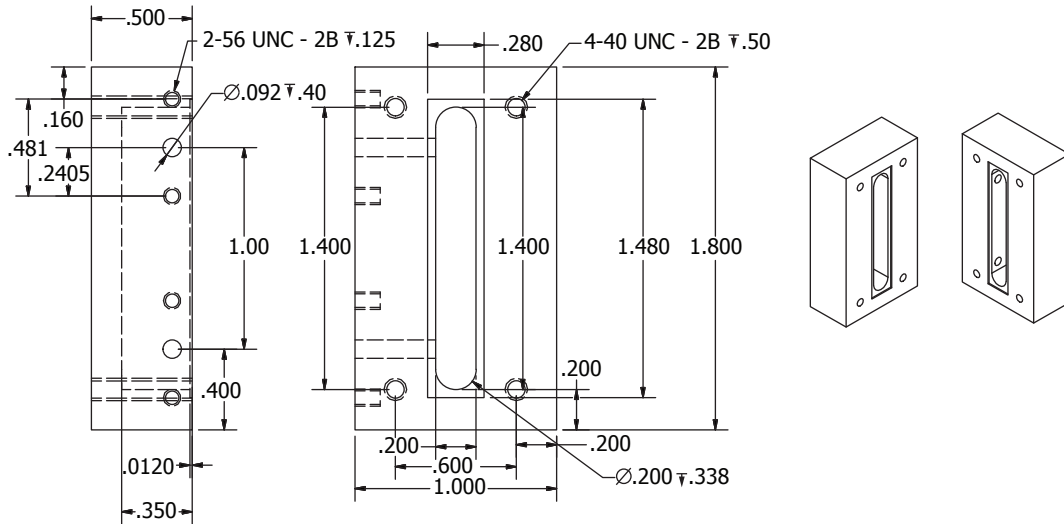


**Figure 6.1:** CAD drawing of the cavity (units are inches) with an isometric view of two cavity halves

## 6.1 Design

The transmon can be transplanted from the planar geometry to a 3D cavity with very few changes to the design. The Josephson junction itself is identical to that used in the planar qubit, and what remains is to design the cavity and qubit electrodes using classic design parameters such that the resonant frequencies, anharmonicities, and charge dispersion are acceptable for the experiment

### 6.1.1 Cavity

The cavity is a closed section of rectangular waveguide, with a recess for a dielectric substrate and a rounded edge for ease of machining. It is designed to have its fundamental frequency at 8 GHz, within the bandwidth of many of our cryogenic circulators and amplifiers. The first few  $TE_{10n}$  harmonics ( $n = 2$ : 10 GHz,  $n = 3$ : 13 GHz,  $n = 4$ : 15 GHz, and  $n = 5$ : 18 GHz), and  $TE_{201}$  ( $\sim 18$  GHz) should be observable with a vector network analyzer. Transverse Magnetic modes are far detuned from the cavity fundamental, and the lowest,  $TM_{110}$  is expected to be at  $\sim 30$  GHz. A transmon placed in the center of the cavity and oriented along the short  $y$ -axis by symmetry only couples weakly to the even- $n$   $TE_{10n}$  modes. Optimal frequency placement for harmonics by adjusting cavity sides has not been sufficiently studied. For suppression of

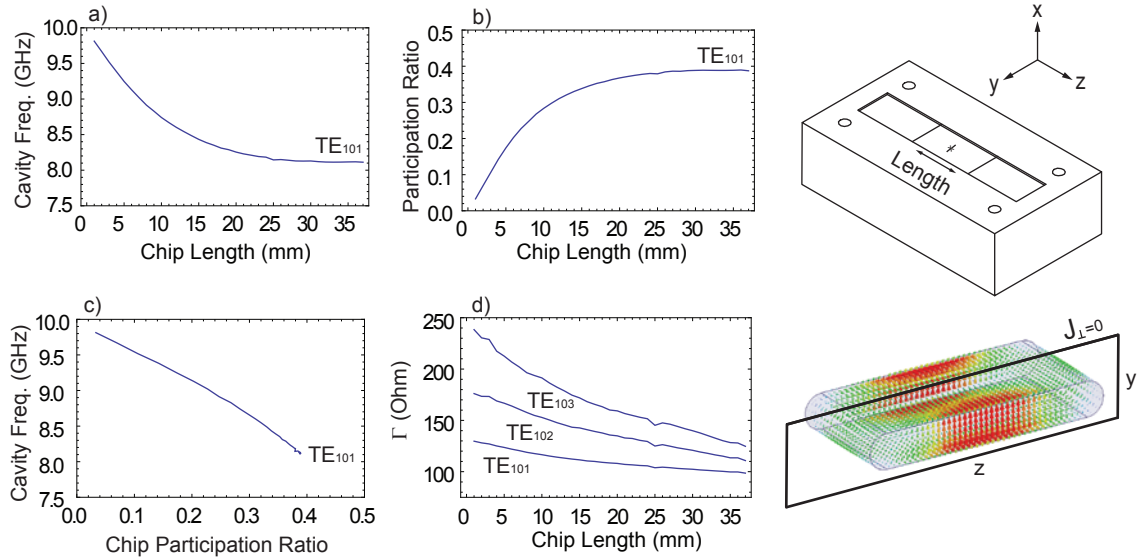


**Figure 6.2:** a) Cavity TE<sub>101</sub> frequency for sapphire chip length, with fixed width 7 mm  $\times$  37.6 mm  $\times$  500  $\mu$ m. b) Chip dielectric participation ratio for different lengths. c) Frequency dependence of TE<sub>101</sub> as a function of chip participation ratio d) Geometric factor  $\Gamma$  for first three cavity harmonics of our 3D cavity; Right: open cavity before assembly and TE<sub>101</sub> current density showing no  $J_{\perp}$  current flow across the two halves.

Purcell decay, it may be important to design the first odd- $n$  harmonic to be far detuned from TE<sub>101</sub>, before optimizing those which do not couple to the qubit. However, any further design strategy is complicated by the infinite mode structure of the cavity. Future work may need to be guided by study with a finite element simulator with confirmation from actual devices.

Two holes for SMA coupling probes deliver power to and from the cavity. Standard chassis SMA jacks with a soldered length of wire extend through the cavity body and form a coaxial transmission line. They may be retracted, forming a short length of cylindrical waveguide before the wire. Power from the TE<sub>101</sub> mode either couples directly to the coax or evanescently (see Sect. 2.3.4) through an effective circular waveguide with cutoff frequency  $\omega_c/2\pi \approx 50$  GHz. The designed hole diameter produces a 10x increase in  $Q_c$  for every 0.5 mm of waveguide.

Conductor loss in the cavity walls scales with the cavity surface resistance  $R_s$ . The geometric factor  $\Gamma$  describing the total surface inductance of a rectangular cavity with our nominal dimensions is 106  $\Omega$ , while HFSS simulations give similar results (see Fig. 6.2). Devices were measured in cavities machined from three types of metal: OFHC Copper, aircraft aluminum (Alloy 6061-T6), and high-purity 4N or 5N (99.99% or 99.995%) aluminum. Cavities were

typically kept covered, and rinsed with acetone, methanol, and IPA before assembly. Joining two cavity halves in the  $z$ - $y$  plane minimizes conductor loss at the cut as any  $TE_{101}$  magnetic field produces current parallel to but none across the cut; furthermore, the cavity is sealed with indium wire\* to minimize contact resistance for any residual cross-piece current.

The two cavity halves clamp a substrate on which the qubit is fabricated. For ease of construction using our normal process, initially a full slab of sapphire was used, stretching the length and width of the cavity. The substrate allows dissipation (see Fig. 6.2) in the bulk sapphire (where the loss tangent is small) or from in lossy materials on the surface (leftover resist, water molecules, or unknown contaminants; see Sect. 2.2.2). Later samples were fabricated with smaller lengths of substrate; there is some indication that use of a small sliver may improve qubit coherence. Although a partial sliver of substrate may disrupt the symmetry of the modes and increase current across the cut, but this is unlikely to limit its quality factor. The sensitivity to a small layer of wall dielectric is fairly small, with an average participation ratio of  $10^{-7}$ /nm of thickness on surfaces.

### 6.1.2 Qubit

The standard qubit design consists of a Josephson tunnel junction with antenna pads as seen in Fig. 6.3. The majority of the qubit mode energy is in the substrate. Its resonant frequency is primarily determined by the antenna pad charging energy  $E_C$  and the Josephson junction energy  $E_J$ , which is known through the junction room temperature resistance. The pad area determines the simple capacitance matrix [25, 49] which defines  $1/C_\Sigma = 1/C_{1c} + (1/(C_{12} + C_J) + 1/C_{2c})^{-1}$ , the charging energy of the pads, composed of the capacitance  $C_{12}$  between the each pad (with an allowance of  $\sim 5$  fF for the capacitance of the junction itself) or the capacitance  $C_{1c}$  or  $C_{2c}$  of either pad to the cavity walls. This description using DC capacitances has been superseded by the use of full-wave simulation (as described in Ch. 3), which leads to more accurate qubit transition frequencies<sup>†</sup>, especially for antenna pads whose inductance cannot be neglected.

In addition, the qubit effective dipole coupling  $\hbar g$  and cavity-qubit interaction  $\hbar \chi$  are strongly dependent on antennae length. For an effective dipole magnitude  $p_0 \approx 2el$  the two

---

\* The necessity of this step has never been proven. Complete hermetic sealing is an interesting idea in part because it might minimize transmission of IR light into the cavity

<sup>†</sup> For reasonable parameters, charge dispersion is suspected to be smaller in BBQ calculations than the classic charge dispersion for charging energy  $E_C$  and  $E_J$ . However, this is an open problem.

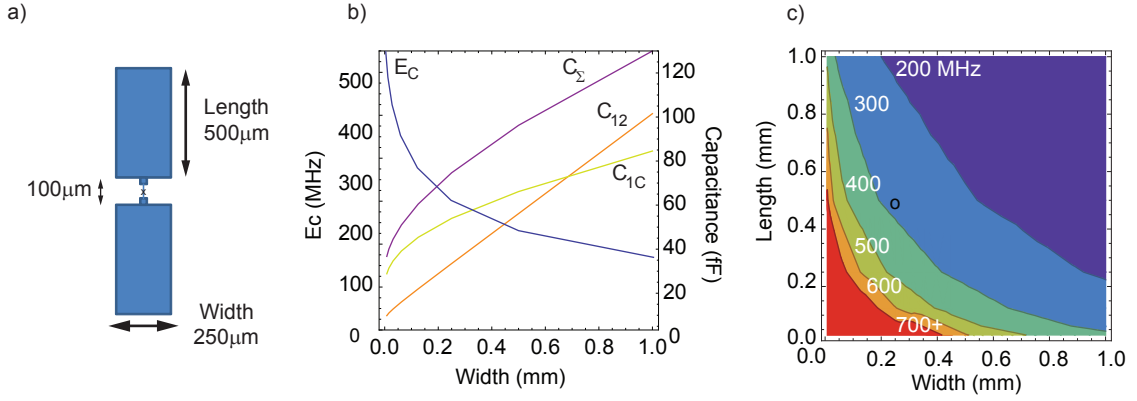


**Figure 6.3:** a) Qubit Diagram. With the exception of Qubit S (which had a slightly different pad structure), all qubits reported here had two  $500 \mu\text{m} \times 250 \mu\text{m}$  antenna pads, with a stepdown  $30 \mu\text{m} \times 30 \mu\text{m}$  pad, and a  $20 \mu\text{m} \times 1 \mu\text{m}$  line to the central junction. The Josephson junction in the center is typically  $(200 \text{ nm})^2$ . b) Simulated capacitances for pad length  $500 \mu\text{s}$  and varied width:  $C_{12}$  between pads (orange),  $C_{1c}$  between a pad and the cavity walls (yellow), and  $C_{\Sigma}$  total charging capacitance (purple) (including  $C_J = 5 \text{ fF}$  for the junction itself), as well as  $E_C$  the total charging energy (blue). c) Contour plot of charging energy  $E_C$  for different widths and lengths. The (o) indicates the typical pad configuration.

electrodes determine  $g/2\pi = \vec{d} \cdot \vec{E}_0 / \hbar$  through the voltage integral  $\int \vec{E} \cdot d\vec{l}$  across the junction. For our 3D cavities where  $E_0 \sim 10^{-4} \text{ V/m}$ , this gives  $g/2\pi \sim 100 \text{ MHz}$  for antennae with  $0.5 \text{ mm}$  length. The parameter  $g$  controls many effects including the Purcell decay rate, but also more subtle design goals such as the qubit-cavity frequency shift  $\chi$  (see Eqn. 3.94). For better accuracy the newer black-box framework and simulation in HFSS should be used as described in Ch. 3.

### Junction Resistance

Junctions are designed to have room-temperature resistance  $R_n$  of several  $\text{k}\Omega$  in order to reach the desired  $E_J$  at  $10 \text{ mK}$ . They are typically  $(200 \text{ nm})^2$  in area with a critical current of  $I_C \approx 40 \text{ nA}$ . Their characteristic energy  $E_J = \frac{\hbar I_C}{2e}$  depends on critical current through the relation:

$$I_c = \frac{\pi \Delta}{2e R_n'} \tanh \left[ \frac{\Delta}{2k_b T} \right] \quad (6.1)$$

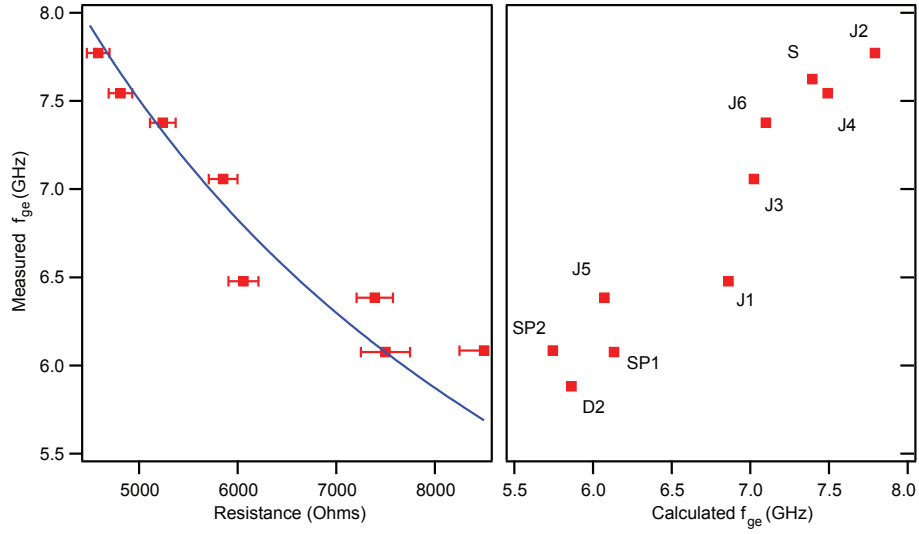


**Figure 6.4:** a) Qubit  $\omega_{ge}/2\pi$  vs room-temperature junction resistance. The fit, using typical  $E_C$  and gap  $\Delta$ , indicates a correction of room-temperature resistance by  $k = 0.86 \pm 0.04$  (see Eqn. 6.1) b) From the measured energy levels and the expanded Jaynes-Cummings Hamiltonian, we may fit the most likely  $E_J$  and  $E_C$ . The root-mean-squared frequency difference between measured values and predicted  $\omega_{ge}/2\pi$  is 3%, primarily determined by junction aging between fabrication and experiments.

where  $R'_n = R_n/0.87$  is the correction for resistance at 10 mK from room temperature measurements [83]. The small signal junction inductance  $L_J = \frac{\hbar}{2eI_c}$  and  $E_C/2\pi = \frac{e^2}{2\hbar C_\Sigma}$  determine the energy of the first transition of the qubit:

$$\hbar\omega_{ge} \sim \sqrt{8E_J E_C} - E_C \quad (6.2)$$

We design this to be below the  $TE_{101}$  cavity frequency to avoid complications from higher-order terms in the Hamiltonian such as the straddling regime [45].

## 6.2 Measurements

In this section, we recount the typical experiments done on each sample to characterize the cavity and qubit energy levels and coherence properties. They are presented approximately in the order in which they are performed upon cooldown. Actual results are presented in the next section, where a narrative of lessons learned accompanies each fabricated device.

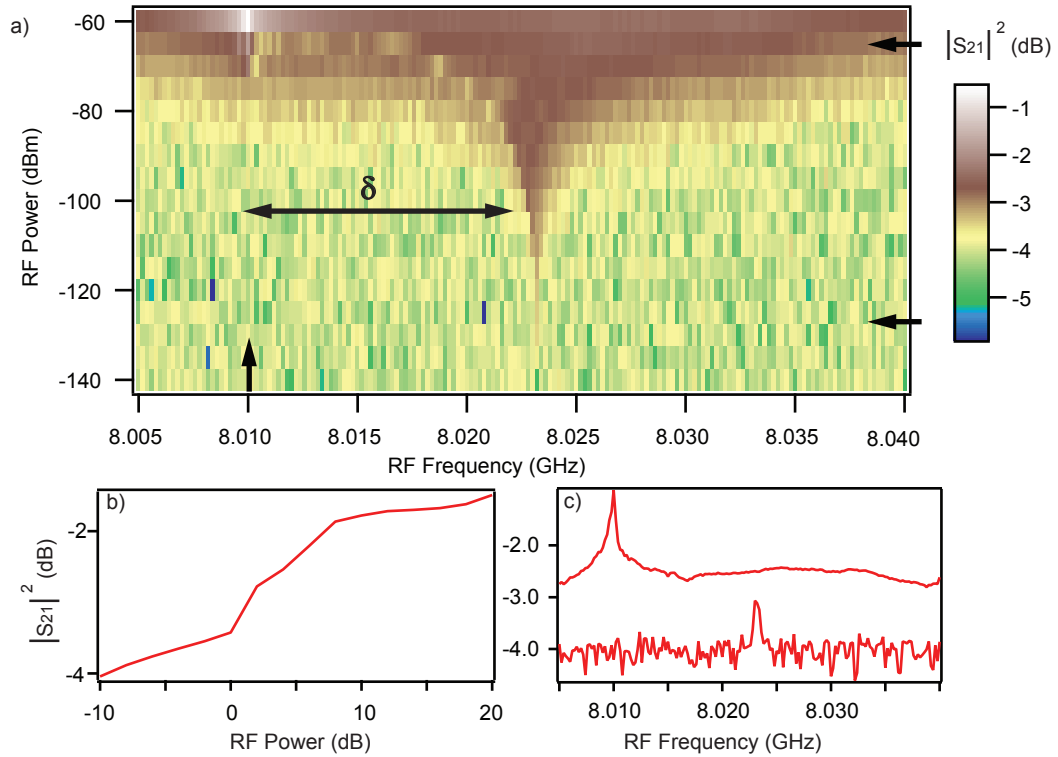


**Figure 6.5:** a) Cavity non-linearity due to the qubit, shown in transmission. With higher incident power the dispersive shift of the cavity is neutralized and transmission is greatest at the bare cavity frequency. Arrows indicate linecuts for inset b (vertical) and c (two horizontal). b) A similar pulsed transmission experiment at the indicated frequency shows an inflection which often indicates optimal readout power, at 0 dB RF Power. c) Cavity spectroscopy linecuts in frequency.

### 6.2.1 Cavity Nonlinearity

The first confirmation of qubit viability in transmon experiments is to observe its non-linear interaction with the cavity, as in Fig. 6.5. Driving at the bare cavity frequency, at high power there is a bifurcation in cavity transmission as the cavity transition frequency becomes the bare frequency. This is usually measured with a  $1 \mu\text{s}$  pulse, and we explain in the next section how integrating the transmission allows a very robust measurement of the qubit state. The difference  $\delta$  between the bare frequency and the low-power shifted frequency of the cavity indicates the approximate frequency detuning of the qubit  $\Delta = \omega_{ge} - \omega_c = g_{ge}^2/\delta$  (using Eqn. 3.51 and second order perturbation theory). In practice the power at which the cavity response is non-linear depends on cavity  $Q$ , however the process is robust even for overcoupled  $Q \sim 1000$  cavities.

### 6.2.2 Readout

Qubit readout is very robust, and is typically performed with a  $1 \mu\text{s}$  pulse at the bare cavity frequency. The resonant pulse will ring up in the cavity before decaying through the output coupler for homodyne signal integration; the shift of the cavity frequency by  $\chi$  with an excited qubit provides a striking contrast in readout voltage, visible on a single shot basis without averaging. This recently developed technique [84] works for planar geometry transmons as well, and often can have fidelity  $F > 90\%$  with appropriate tuning of pulses. The readout provides discrimination of qubit states without the need for significant averaging. For higher quality factor cavities, a longer pulse or integration time may increase fidelity (see Fig. 6.6c); the optimum in power also varies (see Fig. 6.6d). Because it is state destructive and dissipates in the cavity many orders of magnitude more power than the dispersive readout [85], some caution may be advised. A slower repetition rate can lower the thermal load on the sample.

### 6.2.3 Saturation spectroscopy

In first experiments, low-power saturation spectroscopy pulses (typically  $300 \mu\text{s}$  in length), show the dressed cavity transition frequency  $\omega_{01}^g/2\pi$  in transmission, and bring the cavity to a steady state probability of excitation; the same sequence with a readout pulse at the end performs spectroscopy on the qubit. The linewidth of the cavity at frequency  $\omega_{01}$  in transmission gives a reliable measurement of  $\kappa$  for sufficiently weak spectroscopy power.

Together, they allow measurement of the one-excitation manifold of the full Hamiltonian (see Eqn. 3.3.2:

$$H_{\text{eff}}/\hbar = \omega_c a^\dagger a + (\omega_q - \chi a^\dagger a) b^\dagger b - \frac{\alpha}{2} b^\dagger b^\dagger b b, \quad (6.3)$$

where the energy difference  $\chi = \omega_{\text{ge}}^0 - \omega_{\text{ge}}^1$  for qubit transitions with an additional cavity photon is the same as that for the cavity shift  $\omega_{01}^g - \omega_{01}^e$  with an excited qubit (see Fig. 6.7).

With a second tone (see Fig. 6.8, we can clearly see the energies beyond the first excited states. Spectroscopy also reveals sideband transitions of the cavity-qubit system with a change in the state of both, and virtual transition frequencies detuned an additional frequency  $\delta$ . Measurement of not only  $\omega_{\text{ge}}$  but  $\omega_{gf}/2$  aids in fitting of the classic Hamiltonian parameters  $E_C$  and  $g$  from energy levels in experiment.

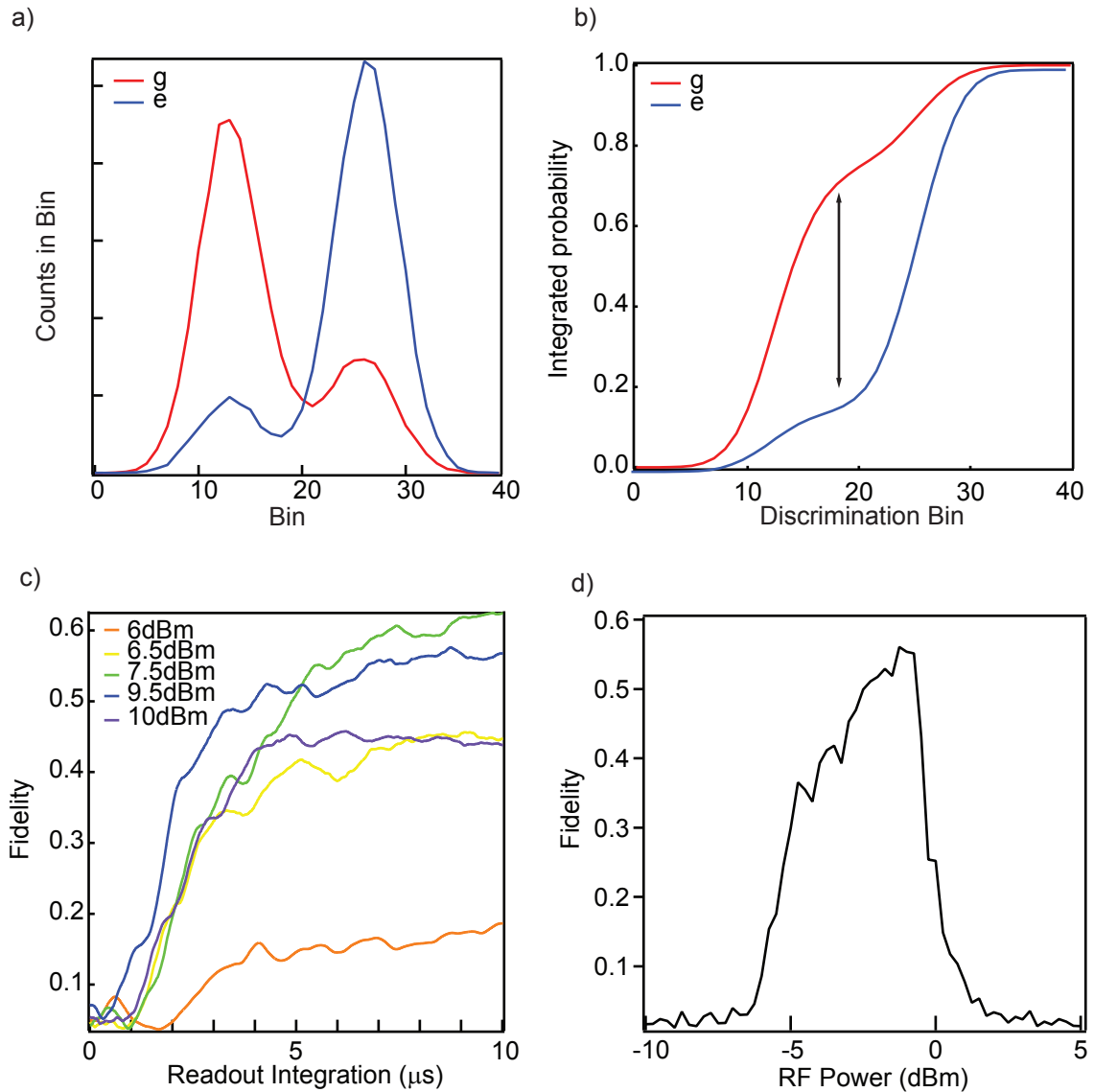


**Figure 6.6:** a) Histogram for voltage from integration of readout pulse, with preparation of  $g$  (red) by waiting or  $e$  (blue) through a  $\pi$ -pulse. The presence of smaller peaks gives loss of fidelity because of initial excited qubit population or imperfect  $\pi$ -pulses. b) Integrals of probability histogram. Optimal fidelity is achieved by choosing the point with largest probability difference. c) Incremental readout fidelity with integration time for a  $2 \mu\text{s}$  readout pulse and several different powers; the cavity ringdown allows for better discrimination than the first few microseconds, for high  $Q$  cavities. Pulse lengths may also be adjusted. d) Readout fidelity at constant integration time increases with power until a threshold is reached.

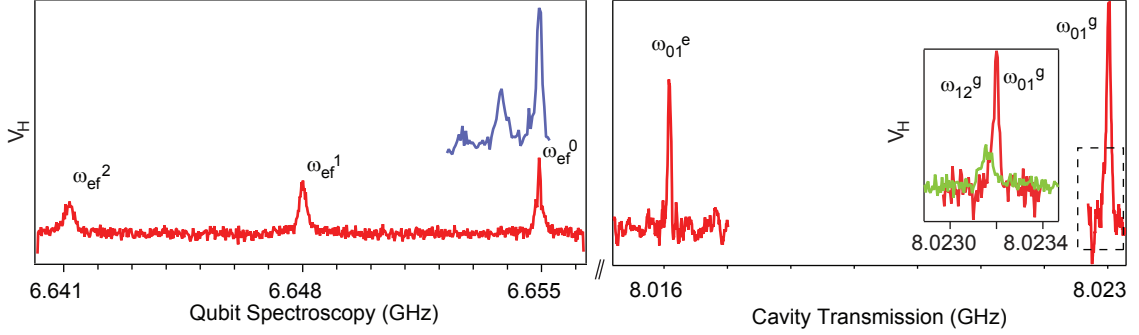


**Figure 6.7:** Cavity and qubit spectroscopy. Left: Photon number split peaks of the qubit are separated by  $\chi$  for thermal state population in a mode of the cavity (red:  $TE_{101}$ , blue:  $TE_{103}$ . b) Cavity transmission frequencies  $\omega_{01}^e$  and  $\omega_{01}^g$  are separated by  $\chi$  as well. This qubit ( $J_3$ ) is far detuned from the cavity, whose anharmonicity diminishes to 30 kHz, making it difficult to address the transition in pulsed experiments, but in other designs this may be as large as several MHz.

#### 6.2.4 Rabi Experiments

Transitions driven on resonance with increasing microwave power proportionally increases the Rabi rate of qubit Bloch vector rotation [86]; for sufficient drive power there is coherent excitation of the cavity or qubit on timescales  $t \ll \sqrt{T_1 T_2^*}$ . The Rabi rate is  $\Omega_R = 2g\sqrt{M}$  for  $M$  drive photons and in the regime  $\Omega_R > \gamma_2^*$  the qubit is power broadened; alternatively a long pulse spins the qubit or cavity vector until it dephases. Alternatively, we may sweep the power of a fixed-length pulse, in a “power Rabi” experiment. A Gaussian pulse with frequency width  $\sigma_f = 1/(2\pi\sigma_t)$ , and a pulse with detuning  $\sim 3\sigma_f$  excites the transition with miniscule amplitude. This can be exploited to perform a controlled-NOT (CNOT) [5] on the combined cavity-qubit system using pulses that selectively rotate the qubit Bloch vector for specific values  $N$  of photons in the cavity [49].

In fact, this allows a measurement of the cavity photon number by comparing the readout signal for power Rabi experiments on different photon peaks, using the amplitude of the  $\sin(\Omega_R t)$  oscillation as a lock-in reading of photon number  $N$  probability (see Fig. 6.9). By measuring to high enough  $N$ , we can estimate  $\alpha$  for a coherent state or  $T_{\text{eff}}$  for a thermal state of the cavity. Its accuracy is influenced by fluctuations in the readout fullscale and this measurement of the photon probability distribution  $P(N)$  is only effective for large dispersive shift  $\chi$  compared to  $\kappa, \gamma$  the cavity and qubit linewidth. Notably, this technique does not detect photons in modes with dispersive shifts smaller than  $\sigma_f$ ; in the limit of small

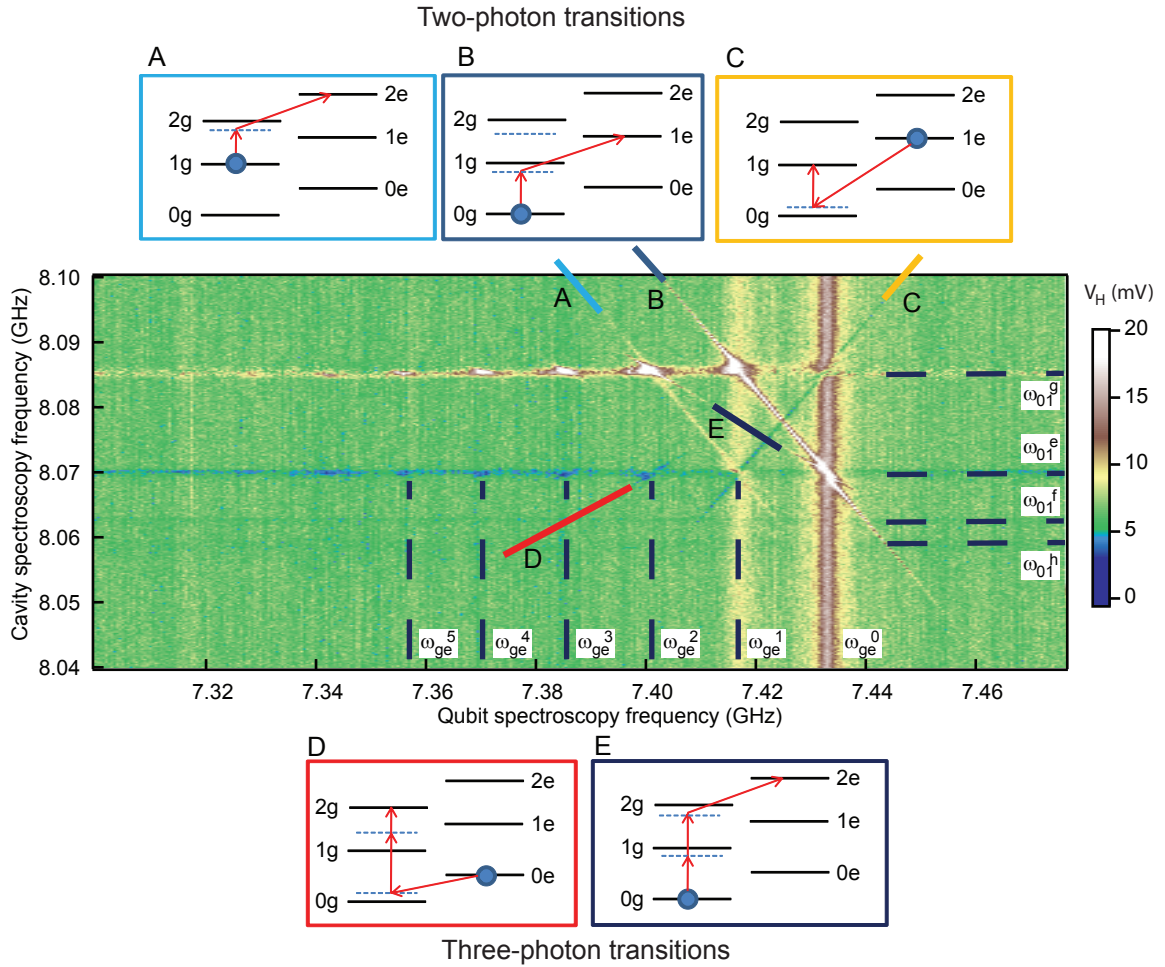


**Figure 6.8:** Two- and three-photon sideband transitions are observed, notably cooling the qubit (C, D)! Virtual transitions with detuning  $\delta$  produce diagonal spectroscopy lines, using energy in two or three photons to drive transitions using higher order terms in the Hamiltonian.

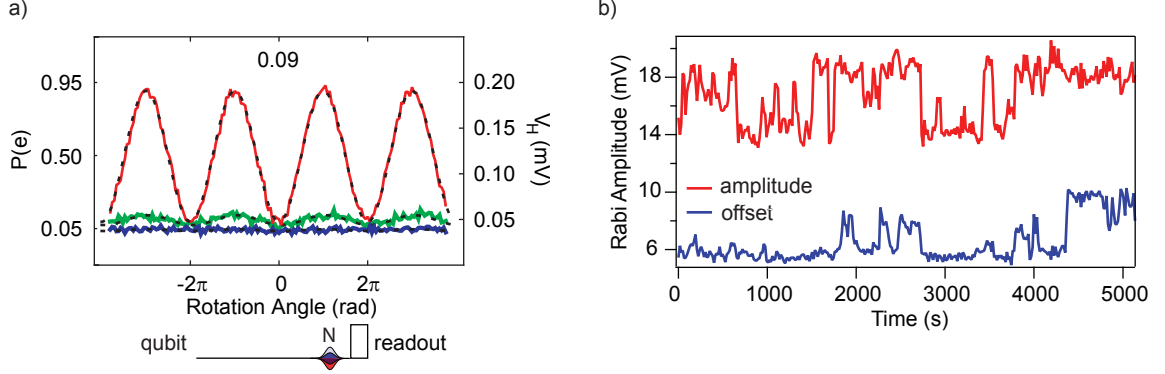


**Figure 6.9:** a) A Rabi experiment with swept power, on the photon number split transitions of the qubit. This protocol measures  $P(N)$ , the probability of  $N=1,2$ , or 3 photons (red, green, blue) from the relative amplitudes of the sine oscillations. b) Fluctuations in the readout and finite fidelity produce jitter in the readout fullscale (red) and offset (blue) which requires more averaging for precise measurements of  $P(N)$ . This is a consequence of finite cavity and qubit population, and individual shot analysis would may be necessary for measurements of less than a part per thousand.

bandwidth (with long weak pulses) we have recreated saturation spectroscopy, and the peak area integral is proportional to probability.

We may worry about driving transitions nearby our intended target using fast pulses, in which case the Rabi rate is often less important than the probability of excitation. We can calculate the driving of nearby photon peaks at  $\omega_n$  using a Dyson expansion. A pulse with center frequency  $\omega_0$  and slowly varying envelope  $A(t)$  evolves as

$$\dot{\psi}_n = -i \left( \omega_n \frac{\sigma_z}{2} + A(t) \cos(\omega_0 t) \sigma_x \right) \psi_n \quad (6.4)$$

Shifting to the rotating frame using

$$\phi_n = \exp(i\omega_0 \frac{\sigma_z}{2} t) \psi_n \quad (6.5)$$

we have

$$\dot{\phi}_n = -i \left[ \delta_n \frac{\sigma_z}{2} + \frac{A(t)}{2} \sigma_x \right] \phi_n \quad (6.6)$$

using  $\delta_n = \omega_n - \omega_0$ . Shifting once more using  $\xi_n(t) = \exp(i\delta_n \sigma_z / 2t) \phi_n(t)$

$$\dot{\xi}_n(t) = -\frac{iA(t)}{2} \left( e^{-i\delta_n \sigma_z / 2t} \cdot \sigma_x \cdot e^{i\delta_n \sigma_z / 2t} \right) \xi_n(t) \quad (6.7)$$

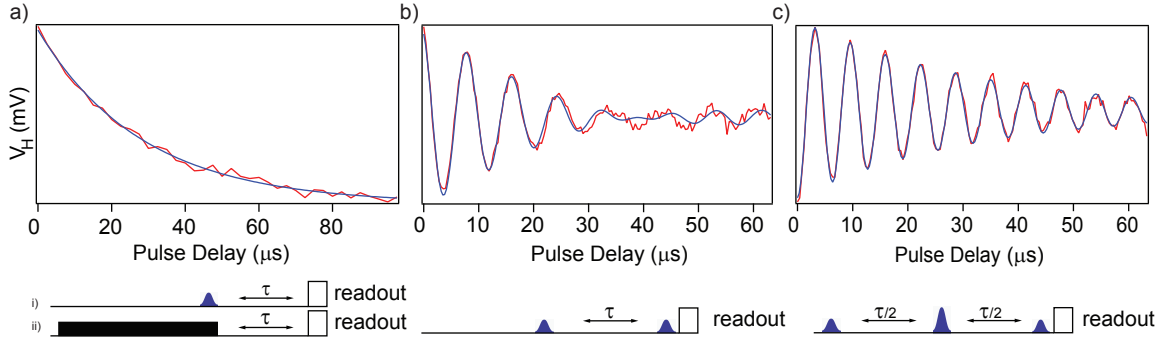


**Figure 6.10:** A suite of coherence time measurements. a) Saturation and pulsed  $T_1$  experiments measure the energy decay of the qubit. Here  $T_1 = 28 \mu\text{s}$  b) Ramsey experiment composed of two  $\pi/2$  pulses with a stepped delay between. This trace shows a beat frequency of 13 kHz in addition to the typical fringes from detuning, and exponential envelope with  $T_2^* = 26 \mu\text{s}$  c) A Ramsey experiment with Hahn echo cancels some fluctuations in qubit frequency. This measurement of  $T_{2E} = 32 \mu\text{s}$  improved further with the addition of low-pass filtering on the input and output lines (see Fig. 8.7).

and in the weak driving limit

$$\xi_n(t) = \xi_n(0) - i \int_0^t \frac{A(t')}{2} e^{-i\delta_n \sigma_z / 2t'} \sigma_x e^{i\delta_n \sigma_z / 2t'} \xi(0) dt' \quad (6.8)$$

$$= |g\rangle - i \left[ \int_0^t \frac{A(t')}{2} \exp(-i\delta_n t') \right] |e\rangle \quad (6.9)$$

giving an excitation of the detuned transition that is proportional to the Fourier component of the envelope at the detuning. It is important to be mindful of the imperfections of our pulses; they are not true Gaussians, but often have been truncated at  $4\sigma_t$  length, and SSB modulation further distorts the spectrum.

### 6.2.5 Coherence Measurements

We measure the decay of the qubit  $|e\rangle$  state and the frequency stability of the  $\omega_{ge}$  transition using  $T_1$  and Ramsey experiments described in Fig. 6.10. The characteristic energy decay time  $T_1$  can be measured through a saturation pulse or as a pulsed measurement. For pulsed measurements and Ramsey experiments in particular it is important to be conscious of the bandwidth  $\sigma_f$  of the pulse. Because often  $\gamma_2^*/\kappa \ll 1$  for the 3D transmon, a narrow qubit pulse may project the combined cavity-qubit state onto a fixed photon number subspace (see Sec. 6.2.4). The Ramsey with echo  $T_{2E}$  can additionally include a rotation about an axis

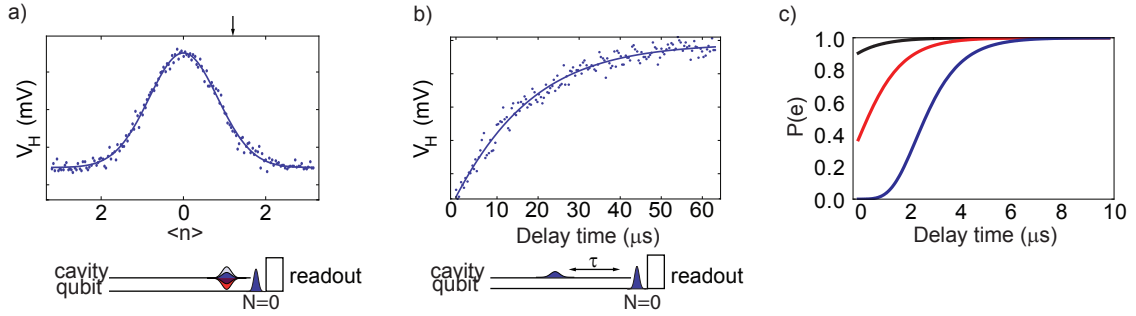


**Figure 6.11:** a) Rabi experiment with swept amplitude pulse on the cavity  $\omega_{01}$  transition, followed by a  $\pi$ -pulse on the qubit  $\omega_{\text{ge}}^0$ . The indicated pulse magnitude is used for the experiment in the next panel. b) Cavity decay experiment with which involves a single such pulse with a delay which is swept, before a  $\pi$ -pulse on the qubit  $\omega_{\text{ge}}^0$ . c) Simulated cavity decay experiment for  $|\alpha|^2 = 0.1$  (black),  $1$  (red), and  $10$  (blue), with  $1/\kappa = 1 \mu\text{s}$ . For small mean photon number, the exponential rise time constant is  $\tau = 1/\kappa$ , while it appears longer for increased  $|\alpha|^2$ , and yields a very different experimental trace when  $|\alpha|^2 \gg 1$ .

$\theta$  from the  $\hat{x}$ , where  $\theta$  is stepped for different time delays\*. A Hahn echo is used to cancel some of the random noise in the qubit transition frequencies. It has differing effectiveness depending on the spectral components of this noise and in particular for non-gaussian noise (see Ch. 7 and Ch. 8 for an example from experiment). Echoes are particularly effective at cancelling fluctuations due to low frequency processes, such as charge noise from quasiparticle tunneling.

### 6.2.6 Pulsed cavity experiments

Transmission spectroscopy of the cavity (see Sect. 6.2.3) can be complicated by its non-linearity, and the most reliable method for determining cavity quality factor is a time-domain measurement similar to a qubit  $T_1$  decay. Three simple experiments together measure the cavity  $\tau$  decay time, (shown in Fig. 6.11) all of which use a final qubit  $N = 0$   $\pi$ -pulse to provide readout contrast.

First, we perform a cavity Ramsey experiment to verify the cavity transition frequency matches that found in spectroscopy. Pulses driving the cavity  $\omega_{01}$  are often 40 dB weaker than a qubit pulse and if possible we use a frequency width  $\sigma_f$  smaller than the cavity anharmonicity, in which case the experiments are completely analogous to qubit coherence measurements.

\* This provides a lock-in signal for fitting which is comfortably similar to  $T_2^*$  Ramsey traces, but is probably not the best practice for measurement as it may obscure the form of the envelope damping function or complicate processing of shot-by-shot measurements.

Otherwise, pulses displace the cavity state, creating a coherent state with a distribution of possible photon numbers. As in a qubit Ramsey experiment, interference fringes form after two detuned displacements but vanish on resonance.

Afterwards, we perform a cavity power Rabi on the cavity  $\omega_{\text{ge}}^0$  resonance and choose a strength which weakly excites the cavity, measuring the return of  $P(N = 0)$  probability over time. If this is impractical because of large  $\kappa$  or small  $\chi$ , the pulse prepares the cavity in a coherent state  $|\alpha\rangle$  (see Ch. 3) which has photon number probabilities:

$$P(n, \alpha) = e^{-|\alpha|^2} \frac{\alpha^{2n}}{n!} \quad (6.10)$$

or in particular  $P(0, \alpha) = e^{-|\alpha|^2}$ . The state decays as  $|\psi(t)\rangle = |\alpha e^{-\kappa t}\rangle$  for  $t > 0$ , giving:

$$P(0, t) = \exp(-e^{-\kappa t} |\alpha|^2) \quad (6.11)$$

as the mean photon number  $|\alpha|^2$  decays at a rate  $\kappa = 1/\tau$ . A stepped delay and final  $\pi$ -pulse on the  $N = 0$  qubit transition allows us to measure the time-domain probability  $1 - P(0, t)$ . For small but finite excitations of the cavity there is a downward correction of the observed  $\tau$  due to complication by the coherent state; for larger  $|\alpha|$  the rise is very clearly non-exponential (see Fig. 6.11).

As a check, it is useful to halve the power again – in the low-power limit, the fit will yield the same value for the exponential decay time constant. This measurement can also be performed using the two-photon sideband transition  $|g, 0\rangle \rightarrow |e, 1\rangle$  followed by a  $\pi$ -pulse on  $\omega_{\text{ge}}^1$ , however this is often experimentally difficult, as it requires either a specially purposed generator or one with high dynamic range. For low  $Q$  cavities in which  $\chi/\kappa \sim 1$  (as is typical for the classic planar transmon) it is more appropriate to use a low-power spectroscopy measurement of the cavity rather than this time-domain experiment.

### 6.2.7 Qubit Anharmonicity and Excited State Population

Qubit anharmonicity is measured using two-tone spectroscopy, often by applying a  $\pi$ -pulse on the  $\omega_{\text{ge}}$  transition before sweeping the second tone to find  $\omega_{ef}$ . Every 3D transmon has shown some small steady-state population of the qubit excited state, and we may measure this using a special protocol [35]. Because the high power readout has little ability to distinguish  $|e\rangle$  from  $|f\rangle$ , we must perform two experiments (see Fig 6.2.7); the first gives the normalization of the readout contrast between  $|g\rangle$  and  $|f\rangle$ . Initially a  $\omega_{\text{ge}}$   $\pi$ -pulse swaps the initial  $|g\rangle$  and  $|e\rangle$

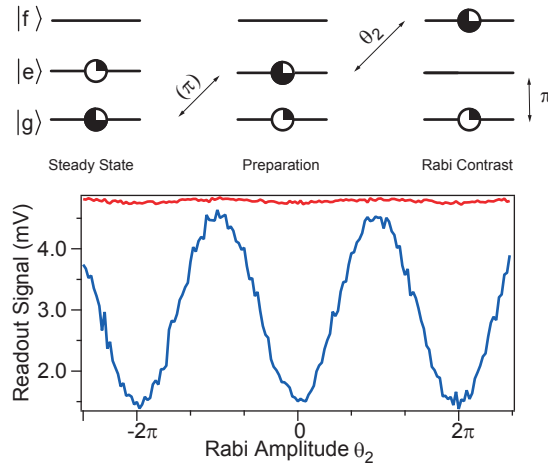


**Figure 6.12:** a) Excited state measurement procedure, composed of two experiments; they differ by the inclusion of an initial  $\omega_{ge}$   $\pi$ -pulse. Afterwards, a power Rabi is performed on  $\omega_{ef}$  ( $\theta_2 = \pi$  is shown in population) followed by a final  $\omega_{ge}$   $\pi$ -pulse. b) Experimental traces with (blue, full contrast) and without (red, small contrast) an initial  $\pi$ -pulse on  $\omega_{ge}$ .

populations, and then a Rabi experiment with varied rotation angle  $\theta_2$  on  $\omega_{ef}$  is performed, before a final  $\omega_{ge}$   $\pi$ -pulse. The experiment is repeated without the initial  $\pi$ -pulse to find the fraction of the population already excited. The transmons higher levels are assumed to be much less populated, as a thermal state has decreasing probability  $P(e) > P(f) > P(h)$  at higher levels, similar to a harmonic oscillator. This has been shown more precisely in newer experiments using the dispersive readout, where the qubit state can be directly determined.

### 6.2.8 Temperature dependence

The 3D transmon is composed of an Al-AlO-Al junction with Al electrodes. When held at any finite temperature, quasiparticles may be created by exciting the superconducting Cooper-pair fluid near the junction over the superconducting gap  $\Delta$ . The density of such equilibrium quasiparticles is temperature-dependent, and can be increased raising the temperature of the sample holder or dilution fridge base plate. These produce a quasiparticle-induced relaxation and frequency shift [87] of the qubit modeled as complex shunt admittance. They are also effectively a thermal bath which may increase the qubit excited state population as they begin

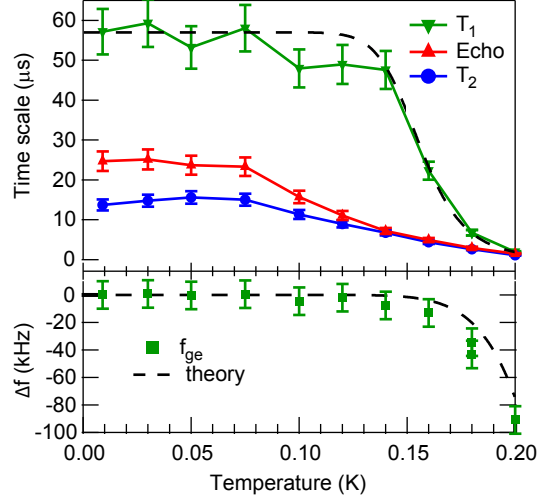


**Figure 6.13:** Temperature dependence of  $T_1$ ,  $T_2^*$  for qubit J1. The decrease in  $T_1$  comes from the thermal activation of quasiparticles in the junction which damp the qubit mode. The decline in  $T_2^*$  and  $T_{2E}$  are due to measurement by thermal photons, similar to experiments in Ch. 8. The plateau in  $T_1$  can be attributed to a non-equilibrium quasiparticle fraction  $x_{ne}$  or an effective temperature of the junction,  $T_{eff}$

to damp the qubit mode\*. The inverse quality factor of a junction due to quasiparticles is:

$$\frac{1}{Q} = \frac{x_{ne}}{\pi} \sqrt{\frac{2\Delta}{\hbar\omega}} + \frac{2}{\pi} e^{-\Delta/k_B T} e^{\hbar\omega/2k_B T} K_0 \left( \frac{\hbar\omega}{2k_B T} \right) [1 + e^{-\hbar\omega/k_B T}] \quad (6.12)$$

Total quasiparticle number is usually separated into equilibrium and non-equilibrium parts; where  $x_{ne}$  is the non-equilibrium quasiparticle fraction,  $K_0$  is the modified Bessel function of the second kind, and  $\Delta$  is the gap in the absence of quasiparticles. Using the same model, the temperature dependence of the relative frequency shift of the qubit is:

$$-\frac{\delta\omega(T)}{\omega} = \frac{x_{ne}}{2\pi} \sqrt{\frac{2\Delta}{\hbar\omega}} + e^{-\Delta/k_B T} e^{-\hbar\omega/2k_B T} I_0 \left( \frac{\hbar\omega}{2k_B T} \right) + \frac{1}{2} [x_{ne} + x_{eq}] \quad (6.13)$$

It is important to note that the presence of non-equilibrium quasiparticles has not been demonstrated in our devices; quasiparticles are not known to limit  $T_1$  for fridge temperatures below 100 mK, at which point their damping follows Eqn. 6.12. Their invocation here only

\* Non-equilibrium quasiparticles likely cause only qubit  $\Gamma_\downarrow$ , not  $\Gamma_\uparrow$  transitions; they have other places to dump excess energy.

Qubit	$f$ (GHz)	$\Delta/2\pi$ ( $\mu\text{V}$ )	$x_{ne}$ ( $10^{-9}$ )
J1	6.808	$195 \pm 1$	400
J2	7.772	$195 \pm 2$	810
J3	7.058	$194 \pm 1$	470
J3 ( $\kappa$ )	6.657	$194 \pm 3$	760
D2	6.4775	$281 \pm 5$	1000
SP1	6.077	$187 \pm 5$	250

**Table 6.1:** The gap  $\Delta$  fit to  $T_1$  during temperature sweeps. Qubit D2 (cQED445) used oxygen doped Al, and therefore has a much higher gap.

represents an upper bound as the minimum detectable fraction, limited by the quality factor or  $T_1$  of the device. A measurement of  $T_1$  and  $\delta\omega(T)$  has been performed for several qubits (see Fig. 6.1), including one in which the gap energy  $\Delta$  is much higher due to oxygen doping of the aluminum in the junction. Independent verification requires a companion device whose superconducting transition is monitored. Non-equilibrium quasiparticles are created in the course of some other superconducting qubit experiments [88], and it may be possible to produce them with infrared light from an LED near the sample holder.

### 6.3 Devices

Many 3D transmon devices have been fabricated and measured. They are largely robust to thermal cycling, transfer between fridges and even cavities, although some degradation of coherence times occurs. On the other hand, as best practices developed, some qubits found better performance with time. A summary of their first or most significant and complete measurements is found in Table 6.2. In a recent publication [51], the energy levels and anharmonicities are fit using HFSS simulations, predicting  $\chi$  and  $\alpha$  to within  $\sim 5\%$ . The properties  $E_C$ ,  $E_J$ , and  $g_{ge}$  recorded here have been calculated from a least-squares fit between the measured transition frequencies and those of a combined cavity-qubit system whose manifold is truncated at 30 energy levels [89].

qubit (cavity)	sample	$f_{01}$ (GHz)	$E_J$ (GHz)	$E_c$ (GHz)	$g_{ge}/2\pi$ (MHz)	$\chi/2\pi$ (MHz)	$\epsilon_1/2\pi$ (Hz)	$f_c$ (GHz)	$Q$ ( $\times 10^3$ )	$T_{cav}$ ( $\mu s$ )	$T_1$ ( $\mu s$ )	$T_2$ ( $\mu s$ )	$T_{echo}$ ( $\mu s$ )	$P(e)$ (pct)	$P(1)$ (pct)
S (D)	cQED381 <sup>‡</sup>	7.625	34.5	0.227	138	35.8	<1	8.01065	340 <sup>†</sup>	7	35	7.3	11	-	-
Sc	cQED381 <sup>‡</sup>	5.638	18.07	0.24	119	-	180	8.00809	9.85	0.2	2-4	-	-	-	-
S (A)	cQED381 <sup>‡</sup>	7.433	32.3	0.230	131	15.9	<1	8.0588	100 <sup>†</sup>	2	20	6	8	16	5
J <sub>1</sub>	cQED394 <sup>‡</sup>	6.808	21.1	0.302	137	8	490	8.00328	340 <sup>†</sup>	7	60	15	25	-	-
J <sub>2</sub>	cQED409 <sup>‡</sup>	7.772	28.7	0.291	152	90	10	8.00362	360 <sup>†</sup>	7	25	15	21	-	-
J <sub>3</sub>	cQED410 <sup>‡</sup>	7.058	22.4	0.305	142	13.2	290	7.9835	320 <sup>†</sup>	6	42	12	12	-	-
J <sub>3</sub> ( $\kappa$ )	cQED410 <sup>‡</sup>	6.657	20.0	0.305	140	7	910	8.01	75-1100	2-22	28	10-27	13-47	5	2
J <sub>4</sub>	cQED432 <sup>*</sup>	7.544	27.5	0.282	138	20	10	8.077	290	6	20	2.5	9.1	12	2.2
J <sub>5</sub>	cQED433 <sup>*</sup>	6.384	19.3	0.291	152	5.4	780	7.82	270	5	28.3	12.2	32.4	6	2.65
J <sub>6</sub>	cQED449 <sup>*</sup>	7.376	26.9	0.277	145	37.5	10	7.8107	410	8	13	10	20	7	-
D <sub>1</sub>	cQED442 <sup>*o</sup>	7.672	-	-	-	res	-	7.839	-	-	10	4.6	16.9	-	-
D <sub>2</sub>	cQED445 <sup>*o</sup>	5.882	16.7	0.287	125	2.8	2800	7.8673	160	3	1.6	2.5	-	-	-
D <sub>3</sub>	cQED446 <sup>*o</sup>	6.478	-	-	-	-	-	7.826	-	-	19	3	13	-	-
SP1 <sup>o‡</sup>		6.078	17.0	0.302	184	3.25	4100	9.16189	190	3	87	42	132	2.5	< 0.03
SP2 <sup>o‡</sup>		6.084	18.3	0.278	181	3.1	840	9.1697	370	6	54	33	101	4	-

**Table 6.2:** Parameters of many transmon qubits (labeled as  $J$  for single junction,  $S$  for SQUID configuration,  $D$  for doped aluminum and  $SP$  for silver phonon pads). <sup>‡</sup>Fabricated by H. Paik and L. Frunzio, <sup>\*</sup>A. Sears, and <sup>o</sup>L. Sun.

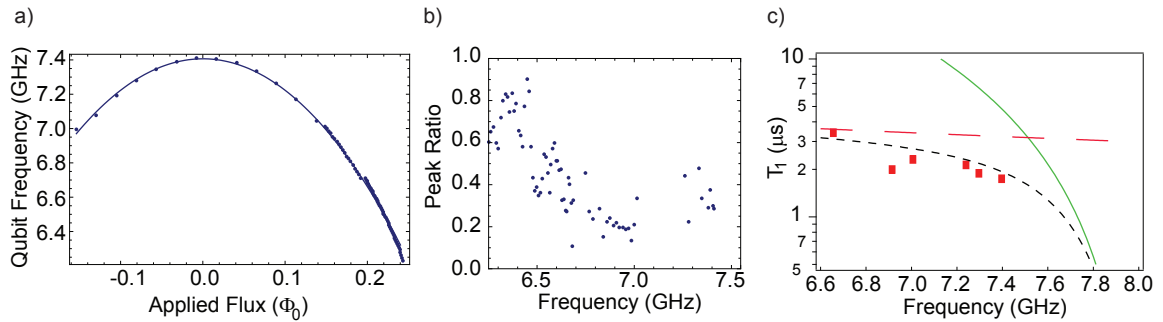


**Figure 6.14:** a) Qubit S is tunable in a copper cavity, with  $f_{\max} = 7.4$  GHz. b) Interestingly, when far detuned for the cavity the amplitudes in spectroscopy of the  $|e\rangle$  peaks were nearly the size of the  $|g\rangle$  peaks. This may be due to Purcell cooling or simply a complication of the readout. c) Its  $T_1$  increases with cavity detuning, but not as much as predicted by Purcell decay (green). The low-power cavity linewidth was 800 kHz for  $Q \approx 10,000$ . Dissipation producing a constant  $Q$  of 150,000 as a separate process has been added (red dashed).

### 6.3.1 Qubit S (SQUID)

Qubit S was the first transmon measured in a 3D cavity. It had two junctions in a  $4 \mu\text{m} \times 8 \mu\text{m}$  SQUID loop, was contained in an aluminum rectangular cavity, and was cooled down in the Cryoconcept Fridge on July 13th 2010. It had an extraordinary  $T_1 > 30 \mu\text{s}$ , with  $T_2^* = 7.3 \mu\text{s}$  and  $T_{2E} = 11.3 \mu\text{s}$ . Because of conservative high  $Q_c$  couplers it required the use of a power amplifier to perform pulsed measurements (which would become standard in later experiments), and pulses heated the fridge to 40 mK; subsequent experiments would use directional couplers to allow some of the reflected power to be dissipated at 4 K. Low power spectroscopy may have shown some excited state population in the qubit, however most data was initially taken at fast repetition rates; later we would change this down to  $\sim 1$  kHz, and prompting the highest measured values of  $T_1$  as well.

The qubit was removed from its Al cavity, remounted in a copper cavity, and placed in the Kelvinox fridge. Its  $T_1$  was found to be  $2 - 4 \mu\text{s}$  at several frequencies via saturation pulses, while we varied its frequency by applying a current using a large superconducting magnet. In Fig. 6.14a we see the frequency tuning of the qubit from high-power spectroscopy. These early scans, as well as most of the pulsed  $T_1$  measurements performed later (see Fig. 6.14c), were done at a fast repetition rate  $\sim 20$  kHz, and the excited state of the qubit was clearly visible in spectroscopy. In the rush to return the qubit to a superconducting cavity Ramsey experiments were not performed; the minimum (though power-broadened) spectroscopy linewidth gave  $T_2^* > 450$  ns.

Several irregularities could have influenced the performance of the qubit in the Kelvinox and may account for the order of magnitude drop in  $T_1$  after transplantation from an Al cavity. A recent retrofit of the fridge had left a light-ray path from nearly from room temperature to inside the vacuum can, potentially exposing it to infrared light that can create non-equilibrium quasiparticles near the junction. In addition, the copper cavity into which it was placed had been used for many cycles in liquid helium dunk tests, and had abundant surface oxidation (although it was washed thoroughly with acetone, methanol and IPA before assembly). It is possible a more aggressive cleaning of the oxide buildup would have provided better results, however the several other appropriate experimental techniques (the use of a much longer repetition rate and nulling of mixer LO leakage) had not yet been put into practice.

At far detuned frequencies the spectroscopy peak height of  $\omega_{ef}$  was only slightly smaller than  $\omega_{ge}$  (see Fig. 6.14b). This is consistent with heating of the internal damping materials of the cavity, due to the large amount of energy being dissipated internally from readout combined with the fast repetition rate. On the other hand, the high power qubit readout can have complications that mimic this effect, rendering the relative peak heights at  $\omega_{ge}$  and  $\omega_{ef}$  inappropriate on their own for estimation of qubit excited state population. A qubit materially connected to a hot cavity would have diminished  $T_1$  due to damping by quasiparticles (see Sect. 6.2.8).

Qubit S was immediately placed into a different superconducting Al cavity and measured in the Kelvinox and found to be at its  $f_{max} = 7.433$  GHz, confirming little aging and low local magnetic field. Its  $T_1$  recovered to  $18.3 \mu\text{s}$  in this new cooldown in the Kelvinox, and a particularly high  $P(e) = 16\%$  and  $P(1) = 6.5\%$  were measured, suggesting that IR light indeed may have been excessive. Ramsey fringes exhibited a 50 kHz beat (too large to be attributable to charge dispersion) which when corrected with echo yielded  $T_{2E} = 8 \mu\text{s}$ .

In principle, there is little reason to doubt the performance of a transmon in a copper 3D cavity (or a suitably designed SQUID transmon), as has been shown in experiments by other groups. If necessary, the complications of Purcell decay due to the finite Q of a copper cavity can perhaps be overcome with a deposited or electroplated layer of superconductor; further experimentation is warranted.

### 6.3.2 Qubits J1, J2, J3

J1, J2 and J3 were the first single-junction qubits measured in a 3D cavity. J1 was originally mounted in an aluminum cavity and placed under vacuum in the Cryoconcept on September

26, 2010, however cooldown was delayed by a failure in the fridge pump system. To mitigate warming of the fridge due to pulse power, a 20 dB directional coupler was installed on the input line. J1 was measured, then thermal cycled to add a second sample\*. In this new run, the qubit e-f transition was visible in spectroscopy and a qubit-excitation pulsed measurement found  $P(e) \sim 10\%$ . Temperature sweeps were performed to be used for publication [82], as well as randomized benchmarking which achieved an optimized single gate error of  $2.5 \times 10^{-3}$ .

J2 and J3 were fabricated in December 2010. J2 was measured in the Cryoconcept, and after being moved to a cryogen-free fridge (and suffering temperature sweeps from another experiment over APS March Meeting 2011) had significantly reduced coherence times  $T_1 = 6 \mu\text{s}$  and  $T_2^* = 6 \mu\text{s}$ , which remained after a thermal cycle. J3 is the first 3D transmon cooled down in a cryogen-free fridge. Its original coherence times were measured to be  $T_1 = 42 \mu\text{s}$ , and  $T_2^* = 12 \mu\text{s}$ , before it was placed in a cavity with a variable coupler. In Ch. 8 we show that its phase coherence was limited by photon dephasing from a coupled heat bath.

### 6.3.3 Qubits J4, J5, and J6

Qubit J4 was installed in a newer version aluminum cavity with couplers at the nodes of the  $TE_{102}$ , yet used one of the earliest wafers diced for qubit fabrication. The cavity required extra machining in order for the wafer to fit and coherence times were miserable:  $T_2^* = 2 \mu\text{s}$  with  $T_{2E} = 8 \mu\text{s}$ . It is a lesson both in the robustness of the 3D transmon and in the importance of taking basic care in their assembly.

Qubit J5 was the first qubit measured with extra filtering. It used an eccosorb filter on both the input and output sides of the cavity to thermalize high frequency modes, and had a record Hahn echo Ramsey time  $T_{2E} = 32 \mu\text{s}$  (discussed more extensively in Ch. 8). During its measurement we developed the qubit excitation experiment and it was the first qubit with a quantified excited state population (as opposed to noticing the presence of  $\omega_{ef}$  transitions in spectroscopy). It was later moved to a different fridge, where with a full set of filters (including KL low-pass on both input and output), qubit and cavity excited state population dropped sharply. The simultaneous increase in coherence and a new  $T_{\phi E} > 800 \mu\text{s}$  discussed in Fig. 8.7 are good evidence that photon dephasing in the 3D transmon has nearly been eliminated through awareness of cryogenic hygiene and proper filtering for a larger number of cavity modes.

---

\* The sample did not work, and the junction was later found to have failed open.

Qubit J6 initially had average coherence times in a 6061 aluminum cavity, with  $T_1 = 13 \mu\text{s}$ . It was later placed in a high-purity 5N aluminum chemically etched cavity, with which our highest measured cavity  $\tau = 42 \mu\text{s}$  with a qubit was measured. With a full slab of sapphire this measurement gives our best upper bound value  $\tan \delta = 1.2 \times 10^{-6}$  of sapphire in the quantum regime (at millikelvin temperatures and single-photon excitations).

#### 6.3.4 D1, D2, and D3

Qubits D1, D2, and D3 were fabricated using a special tri-layer approach [90] which allowed for a large superconducting gap  $\Delta$  using dirty aluminum as one layer of the junction. D1 was nearly resonant with the cavity, which created difficulties in measurement and calibration beyond the intentions of the experiment. D2 was extremely undercoupled, difficult to measure, and had a  $T_1$  of only a couple microseconds; the large proportion of power dissipated in driving it may have heated the qubit, making its coherence times inappropriate for useful deductions. However, D3 was measured with  $T_1 = 19 \mu\text{s}$  at base temperature and allowed us to use measurements in a temperature sweep to observe quasiparticle damping above 200 mK.

#### 6.3.5 Qubits SP1, SP2, and cQED457

Qubit SP1 and SP2 were fabricated with special silver pads on the edge of a small, double-polished substrate. SP1 had record coherence times and a small excited state qubit population; its cavity population was tracked to less than a part in 1000, using a temperature sweep to verify the measurement process (see Fig. 8.8). At  $\leq 37$  mK (also the fridge temperature) this is the coldest a 3D cavity has been observed, requiring considerable averaging; it is most likely significant that the cavity is relatively overcoupled, as one concern is that our high readout power heats the internal temperature of the cavity (or its lossy elements). The sample cQED457 was fabricated by H. Paik with two qubits on a single double-polished chip. After re-cooling with a lower coupling Q, coherence times for one of the pair increased substantially.

## Conclusions

The 3D transmon offers revolutionary insight into issues of coherence through eliminating many distracting components found in earlier superconducting qubit experiments, such as PC-

boards, lossy oxides, and thin films. The fabrication, assembly, and measurement procedures are very robust. Much optimization remains for cavity and qubit design, from a large space of possible modifications: qubit superconductor,  $g$ , substrate size and composition, coupler type, cavity preparation, sealing, and material. Its modularity also encourages experimentation and the swapping of parts.

The 3D transmon achieved record superconducting charge qubit coherence  $T_1$  times without special engineering of the cavity or junction materials. Its increasing coherence times have spurred the adoption of additional microwave components and hardware. Their measurements provide a first test of black-box quantization and a challenge to include charge dispersion within the model.

In the next chapter we discuss briefly the various dephasing processes which may affect it, before investigating photon shot noise dephasing in Ch. 8.

# CHAPTER 7

---

## Introduction to Dephasing

---

**T**HIS The dual of qubit energy decay is pure dephasing, the loss of phase coherence over time as the energy levels of a device fluctuate. Phase coherence is ultimately limited not just by  $T_\phi$  processes but also by dissipation  $T_1$  processes, through the standard equation

$$\frac{1}{T_2^*} = \frac{1}{2T_1} + \frac{1}{T_\phi} \quad (7.1)$$

There are many sources of dephasing known to affect superconducting qubits: charge noise, critical current noise, and fluctuating cavity photon number among others. In this brief chapter we elaborate the influence of mostly classical fluctuators on qubit transition frequencies and the Ramsey experiment, the Hahn echo, and its effectiveness for different types of noise. This is followed by a description of the current estimates of dephasing from recent literature.

### 7.1 Dephasing

We can simplify the influence of the environment by considering an interaction with only the first two transmon energy levels via the Hamiltonian

$$H(t)/\hbar = [\omega_q + \delta\omega(t)] \sigma_z \quad (7.2)$$

These fluctuations in the qubit energy levels cause decoherence as the qubit state accumulates a random amount of phase over time, or as off-diagonal terms in the qubit density matrix decay after experiment repetitions are averaged. The Ramsey experiment (see Sect. 6.2.5) is a simple procedure to quantify the noise spectrum of a transmission frequency. We can characterize the fluctuations  $\delta\omega(t)$  using the “Physicist” spectral density (often normalized with the qubit frequency  $\omega_{ge}$ )

$$S[\omega] = \frac{1}{\omega_{ge}^2} \int_{-\infty}^{\infty} dt \langle \delta\omega(t) \delta\omega(0) \rangle e^{i\omega t} \quad (7.3)$$

describing the intensity of *fractional* fluctuations, with units  $[\text{Hz}]^{-1}$ . The magnitude and rolloff of  $\delta\omega$  the distribution determines the decay rate  $\Gamma_\phi = 1/T_\phi$  and the form of the experimental Ramsey envelope  $F_R$ . In the rotating frame of the qubit, the Ramsey envelope is determined by the time-averaged correlation of the extra qubit phase  $\phi(t)$  derived from fluctuations in qubit frequency:

$$[\phi(t) - \phi(0)] = \int_0^t \delta\omega(t_1) dt_1 \quad (7.4)$$

An ensemble average of the fluctuations gives the phase variance

$$F_R = \langle e^{i[\phi(t) - \phi(0)]} \rangle \quad (7.5)$$

or expressed in terms of the  $c_n$  cumulant expansion of the random variable  $\delta\omega(t)$ :

$$F_R = \left\langle \exp \left[ i \int_0^t \delta\omega(t) \right] \right\rangle \quad (7.6)$$

$$= \exp \left[ \sum_1^{\infty} \frac{i^n}{n!} c_n \right] \quad (7.7)$$

where for example  $c_1 = \langle \delta\omega(t) \rangle = 0$  and  $c_2 = \langle \delta\omega(t)^2 \rangle - \langle \delta\omega(t) \rangle^2$  is the fluctuation variance.

## 7.2 Gaussian Noise

Assuming that fluctuations in qubit frequency are Gaussian greatly simplifies calculations of qubit dephasing; the random variable  $\phi(t)$  can be expanded in terms of its cumulants, all of which vanish except for the mean and variance. The ensemble average gives an envelope

$$F_R = e^{\langle [\phi(t) - \phi(0)]^2 \rangle / 2} \quad (7.8)$$

determined by the nature of the frequency fluctuations

$$\langle [\phi(t) - \phi(0)]^2 \rangle = \int_0^t dt_1 \int_0^t dt_2 \langle \delta\omega(t_2) \delta\omega(t_1) \rangle \quad (7.9)$$

$$= \frac{\omega_{\text{ge}}^2}{2\pi} \int_0^t dt_1 \int_0^t dt_2 \int_{-\infty}^{\infty} S[\omega] e^{-i\omega t} d\omega \quad (7.10)$$

$$= \omega_{\text{ge}}^2 \frac{t}{2\pi} \int_{-\infty}^{\infty} S[\omega] \frac{\sin^2(\omega t/2)}{(\omega t/2)^2} d(\omega t/2) \quad (7.11)$$

where the weighting factor  $W_{\text{Ramsey}} = \sin^2(x)/x^2$  arises due to the specific correlation measured in Ramsey experiments and limits the influence of higher frequency noise. This envelope is an exponential for a noise process that creates broadband white, Gaussian fluctuations  $S[\omega] = S_0$  independent of frequency lead to an exponential decay in the Ramsey signal

$$F_R = e^{-\Gamma_\phi t} \quad (7.12)$$

with  $\Gamma_\phi = \omega_{\text{ge}}^2 S_0/4$ .

## Hahn Echo

The use of multiple echo pulses can prolong qubit coherence by eliminating the influence of low-frequency noise; the weighting function for a Hahn echo experiment with only a single pulse vanishes at zero frequency. Information about the spectral density  $S[\omega]$  may be recovered through additional experiments with different weighting function  $W$  [91]. Most of our qubits display some improvement  $T_{2E} > T_2^*$  of coherence in Hahn echo experiments. Here a Hahn or spin-echo  $\pi$ -pulse is applied to the qubit in between the two  $\pi/2$ -pulses, negating any accumulated phase and removing the influence of noise processes which produce identical phase drift on either side of the echo. The Ramsey with echo signal is

$$F_{\text{echo}} = \langle e^{[\phi(-t) + \phi(t) - 2\phi(0)]} \rangle \quad (7.13)$$

$$\approx e^{\langle [\phi(-t) + \phi(t) - 2\phi(0)]^2 \rangle / 2} \quad (7.14)$$

again using the approximations of Gaussian noise. Integrating the ensemble average it can be shown that

$$\langle [\phi(-t) + \phi(t) - 2\phi(0)]^2 \rangle = \omega_{\text{ge}}^2 \frac{2t}{\pi} \int_{-\infty}^{\infty} S[\omega] \frac{\sin^4(\omega t/2)}{(\omega t/2)^2} d(\omega t/2) \quad (7.15)$$

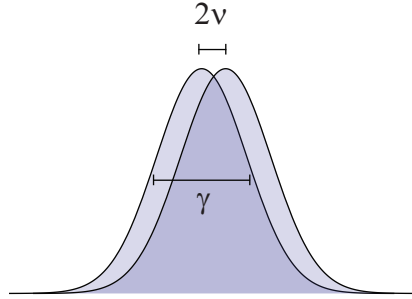


**Figure 7.1:** Weak fluctuator model for a two-level system, in which  $\delta\omega = \pm\nu$  is smaller than the switching rate  $\gamma$ .

where the weighting function vanishes at zero frequency, in contrast to Eqn. 7.11. For white noise it too produces an exponentially decaying signal with a time constant  $\Gamma_{\text{echo}} = \omega_{\text{ge}}^2 S_0/4$ , but for distributions with noise power with more intensity at lower frequencies we expect the envelope decay time to be longer.

### 7.3 Random Telegraph Noise

One comparatively well understood instance of non-Gaussian noise is that of a Random Telegraph Process (RTP). Its simplest model consists of a two-level classical fluctuator or property A which switches between two states  $\xi_A = \pm 1$  at a rate  $\gamma$ , and interacts with the qubit via the Hamiltonian [92]

$$H_{\text{TLS}} = \nu \xi_A(t) \sigma_z \quad (7.16)$$

The fluctuator then has a single-pole Lorentzian spectrum with  $\omega_0$  cutoff frequency which we approximate by a Gaussian process with variance  $\sigma_A^2 = \nu^2$  and a low-frequency cutoff  $\omega_0 = \gamma$

$$S_A = \frac{4\sigma_A^2/\omega_0}{1 + (\omega/\omega_0)^2} \quad (7.17)$$

and we find via contour integral for  $S_0 = 4\sigma_A^2/\omega_0$

$$\langle [\phi(t) - \phi(0)]^2 \rangle = \omega_{\text{ge}}^2 \frac{t}{2\pi} \int_{-\infty}^{\infty} \frac{4\sigma_A^2/\omega_0}{1 + (\omega/\omega_0)^2} \frac{\sin(\omega t/2)^2}{(\omega t/2)^2} d(\omega t/2) \quad (7.18)$$

$$= \frac{S_0}{2} \omega_{\text{ge}}^2 t \left(1 - \frac{1}{\omega_0 t} (1 - e^{-\omega_0 t})\right) \quad (7.19)$$

which in the limit of large  $\omega_0 t$  (weak intensity or experiment times long compared to the noise bandwidth) simply reproduces the white noise result. For small  $\omega_0 t$  we get

$$\langle [\phi(t) - \phi(0)]^2 \rangle / 2 \approx \omega_{\text{ge}}^2 \frac{S_0}{4} \omega_0 t^2 \quad (7.20)$$

$$= \omega_{\text{ge}}^2 \sigma_A^2 t^2 \quad (7.21)$$

The Ramsey decay is no longer described by a rate, it has a characteristic time  $1/\omega_{\text{ge}}\sigma_A$  and a ‘‘Gaussian’’ envelope. Many physical processes are dominated by low-frequency contributions and the sum of many Lorentzian distributions over many octaves produces flicker or  $1/f$  noise. Depending on the actual distribution the envelope decays with exponent  $t^2$  (gaussian) or  $t^\alpha$  ( $1 < \alpha < 2$ ), and these indeed arise as valid explanations in other superconducting [93] and alternative solid-state [94] qubits. Such an envelope has been observed once clearly in a 3D fluxonium device made in the Devoret lab, and once in a low- $T_2^*$  3D transmon where  $\alpha > 1$  better described the Ramsey trace. More sophisticated analyses including multiple echoes and specialized experiments [95] have been used to measure the wider noise spectrum for superconducting qubits.

### 7.3.1 Exact solution

Non-gaussian fluctuations of the qubit transition frequency have been studied far less extensively, and are often treated only briefly. In spectroscopy the lineshape of such a transition is neither Gaussian nor Lorentzian; in the above model the spectrum becomes non-gaussian as  $\nu > \gamma$ , we leave the motional narrowing regime [96], and we can no longer approximate the noise by its variance.

In the RTP model,  $\gamma$  is symmetric and each state is equally likely. Analytical calculations have determined the qubit dephasing induced by the energy level fluctuations as well as the effectiveness of echo pulses in correcting it [97]. They construct and solve a master equation for the probability  $P(\phi, t)$  for the accumulated phase to be  $\phi$  at time  $t$ . There are two regimes: weak and strong coupling, depending on the value of  $\nu/\gamma$ . In both, the dephasing rate which

describes the decay of off-diagonal terms in the qubit density matrix, can be described by:

$$\Gamma_\phi = \gamma \left( 1 - \Re[\sqrt{1 - \nu^2/\gamma^2}] \right) \quad (7.22)$$

This expression has a maximum at  $\nu = \gamma$ , and decreases for smaller  $\nu$  (into the "motional narrowing" regime approximated by Gaussian noise) or for smaller  $\gamma$  (in which case dephasing events become less common, but the fluctuator and qubit are entangled). With echo pulses of sufficient frequency  $1/\tau$  it can be reduced. In their model for dynamical decoupling they consider  $\pi$ -pulses equally spaced in time and infinitely sharp so as to cover all fluctuations in qubit frequency.

For weak fluctuators  $\nu/\gamma < 1$ , the corrected dephasing rate at long timescales is

$$\Gamma_2^{dd} = \frac{\nu^2}{2\gamma} \left( 1 - \frac{1}{\gamma\tau} \tanh \gamma\tau \right) \quad (7.23)$$

and effective decoupling requires echoes more frequently than the switching rate  $1/\tau > \gamma$ . For strong fluctuators,  $\nu/\gamma > 1$ , they find instead

$$\Gamma_2^{dd} = \text{Min} \left[ \gamma \left( 1 \pm \frac{1}{\nu\tau} \sin(\nu\tau) \right) \right] \quad (7.24)$$

where effective decoupling requires echoing at a rate faster than the frequency shift  $1/\tau > \nu$ . A more general solution for RTP dynamical decoupling is an open problem, for models with asymmetric rates and unequal populations for the two states; it may be soluble simply by adjusting the parameters of the master equation. Nevertheless, the model is useful in describing the two regimes (weak and strong coupling) which arise in dephasing phenomena.

## 7.4 Mechanisms of Dephasing

In the remainder of this chapter we revisit several currently known dephasing processes for the 3D transmon: charge noise and quasiparticle tunneling, critical current noise, and photon-induced dephasing. One particularly interesting result is that the strongly coupled regime  $\nu/\gamma > 1$  is important for all three.

### 7.4.1 Charge Noise

In a charge qubit increased  $E_J/E_C$  for the Cooper-pair box leads to a charge dispersion of the energy levels while in the transmon energy levels have exponentially reduced sensitivity to  $n_g$

(see Eqn. 3.44). A change in gate charge  $n_g$  nevertheless modulates  $\omega_{ge}$  with finite amplitude, primarily through the contribution from the first excited level [45]:

$$\frac{\partial \omega_{ge}}{\partial n_g} \approx \frac{\pi}{\hbar} \epsilon_1 \sin(2\pi n_g) \quad (7.25)$$

Motion of trapped charges on the nearby substrate, DC fluctuations on input couplers, or when a quasiparticle tunnels from one pad to another through the junction all may dephase qubit superpositions. For several 3D transmons in Table 6.2 the dispersion may be many kHz and is approaching the natural qubit linewidth, indicating the qubit transition frequency can be sensitive to the quasiparticle tunneling rate.

A 3D transmon with elevated charge dispersion has recently been used to intentionally measure the rate of such quasiparticle tunneling, which follows the above RTP model quite closely [?]. The populations of even and odd parity branches and the transition rates between them seem to be similar, and they find the tunneling times to be about 1 ms (rates  $\Gamma_g^{eo}/2\pi \approx \Gamma_e^{eo}/2\pi \approx 160$  Hz). Each tunneling event shifts the qubit  $\omega_{ge}$  frequency by approximately  $\epsilon_1/\hbar$  as charge dispersion increases with transmon level  $m$ . Even in the absence of significant dephasing from charge or quasiparticle fluctuations, Ramsey experiments using pulses too short to discriminate between the quasiparticle parity will include an oscillating beat at the difference frequency  $\Delta f = f_o - f_e$  of the two parity branches; this is a possible explanation for the beat frequency in some of our Ramsey experiment traces.

When this splitting is larger than  $\Gamma^{eo}$ , each tunneling event dephases the qubit completely and the total dephasing rate is simply

$$\gamma_\phi^{qP} = \Gamma^{eo} \quad (7.26)$$

This holds until charge dispersion is suppressed below 160 Hz and we enter the motional narrowing regime, which for  $\epsilon_1/h = 10$  Hz gives  $T_\phi \approx 1$  s. In fact, their device was not limited by quasiparticle tunneling but by background charge fluctuations. These have increasing noise power at low frequencies, with estimates of the charge spectral density  $S_{n_g} = 2\pi|B|^2/f$  amplitude at 1 Hz of  $B \approx 10^{-4} - 10^{-3} e$  [98]. In between tunneling events in the same experiments, Riste instead measures directly the qubit fluctuation spectral density suspected to be due to charge noise  $S_f = 8.1 \times 10^7/|f|^{1.7}$  Hz which when integrated accounts for the short  $T_2^* < 25 \mu s$  for their device. The spectrum seems to have included a contribution from the fridge mechanical pulse tube, and such measurements may be useful in identifying the origins

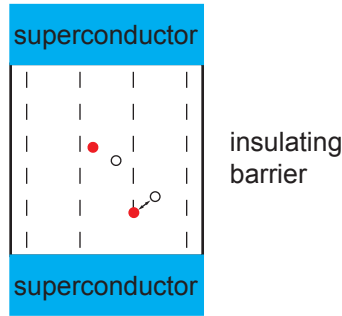


**Figure 7.2:** Josephson junctions have a number of tunneling channels proportional to their area. Fluctuating two-level systems may intermittently block this process, reducing the effective area altering the critical current  $I_C$  which determines qubit parameters.

of other charge fluctuations. Ultimately, however, this is not an untreatable issue; it can be avoided by simply increasing the  $E_J/E_C$  ratio during the design process, particularly for sets of qubits with varied frequency.

#### 7.4.2 Critical Current Noise

Critical current noise is the rearrangement (in effect, the closing and opening) of individual conductance channels through the Josephson junction barrier (see Fig. 7.2); this switching can lead to a fluctuation of  $I_C$  and therefore  $E_J$  (see Eqn. 6.1) and hence  $\omega_{ge}$ , and tends to modulate the effective cross-sectional area of the junction rather than the barrier thickness or other properties. These events seem to be more frequent at higher temperatures [99], with a noise spectrum that may be problematic for junctions at finite temperature if it continues to scale with the universal behavior. The most recent measurements have indicated a linear  $T$  dependence of fractional fluctuations in the critical current which scale with the junction volume [100]

$$\frac{S_{I_c}}{I_c^2} \approx (\delta A)^2 \rho t \frac{1}{A} \frac{T}{f} \quad (7.27)$$

where  $\rho$  is the density of two-level system fluctuators,  $T$  is the temperature in Kelvin,  $A$  and  $t$  are the junction area and thickness. Nugroho et al. posit a universal scaling with  $\rho_{TLS} \approx 10^{17} \text{ cm}^{-1} \text{ K}^{-1}$ , with abnormalities for small-dimensional junctions, suggesting that individual defects may cause fluctuations on the order of  $\delta A \sim 0.1 \text{ nm}^2$  in junction conductance area. The typical volume for our transmon junctions is  $150 \text{ nm} \times 300\text{-}500 \text{ nm}$  (depending upon

the resistance goal) or less than  $0.1 \mu\text{m}^2$ , with a  $t \approx 1 \text{ nm}$  tunnel barrier thickness, and have  $I_C \sim 40 \text{ nA}$ , such that individual fluctuators may modulate the qubit frequency by  $\sim 15 \text{ kHz}$ . If such a large frequency shift is present, the TLS switching rate then determines dephasing.

Instead, in the limit of small  $\delta A$  fluctuations we may calculate the decay time of weak  $1/f$  fluctuators by restricting the frequency span, as the integral for  $S_{I_c}$  otherwise diverges. Limiting the bandwidth to some number of octaves (set by the finite single experiment or total acquisition times, for example), the normalized frequency variance is

$$\sigma_\omega^2 = \left( \frac{\partial \omega_{\text{ge}}}{\partial I_c} \right)^2 \int_{f_{\text{exp}}}^{f_{T_2^*}} \left( \frac{S_{I_c}}{\omega_{\text{ge}}^2} \right) df \quad (7.28)$$

$$= \frac{1}{\omega_{\text{ge}}^2} \left( \frac{\omega_{\text{ge}}}{2I_c} \right)^2 B^2 \ln[f_{T_2^*}/f_{\text{exp}}] \quad (7.29)$$

where we have approximated for large  $E_J/E_C$ , and  $B$  is the density of the  $1/f$  noise at  $1 \text{ Hz}$ . The integral accrues a factor of  $\sim 5x$  over the experimental bandwidth and produces a mostly Gaussian decay with time constant  $T_2^* = 1/\omega_{\text{ge}}\sigma_\omega = 1/4\omega_{\text{ge}}B$ . However, because  $1/f$  spectra are dominated by low-frequency noise the qubit benefits from echo pulses, and we can show that the phase correlator for an echo experiment obeys

$$\langle [\phi(-t) + \phi(t) - 2\phi(0)]^2 \rangle = \omega_{\text{ge}}^2 \frac{t}{2\pi} \cdot \int_{-\infty}^{\infty} \frac{B^2 \sin^4(\omega t/2)}{|f| (\omega t/2)^2} d(\omega t/2) \quad (7.30)$$

$$= \frac{1}{2} \omega_{\text{ge}}^2 t^2 \cdot 2B^2 \ln(2) \quad (7.31)$$

such that

$$F_{\text{echo}} = \exp[-\omega_{\text{ge}}^2 B^2 t^2 \ln(2)/2] \quad (7.32)$$

and the effective decay time with echo is  $T_{2E} = 1/\omega_{\text{ge}}B\sqrt{\ln(2)/2}$ , such that  $T_{\text{echo}}/T_{\text{Ramsey}} \sim 5$ .

These studies are the most comprehensive dataset on critical current noise, yet were performed at temperatures above  $300 \text{ mK}$ ; because our devices are held closer to  $30 \text{ mK}$  their applicability may be limited. In fact our best devices may reach this limit, depending on the assumed value of  $T$ . The mean  $T_2^*$  for qubits that have been measured at  $100 \text{ mK}$  (where thermalization can be guaranteed) have  $T_2^* = 13 \pm 3 \mu\text{s}$ , with quality factors  $Q < 650,000$  and below the upper bound for this value of  $\rho_{\text{TLS}}$ . However, most of this degradation comes from photon dephasing, so it is not clear that we have seen any effects of critical current

noise. Verifying the  $T$  or  $T^2$  scaling of critical current dephasing at low temperatures would illuminate the microscopic origin of the fluctuations [101].

### 7.4.3 Photon Induced Dephasing

The transmon cavity has been engineered to suppress dissipation but also to facilitate measurement using photons and the cavity-qubit state dispersive shift. Modern microwave generators and amplifiers allow us to control the dynamic range of interaction over many orders of magnitude but there may be stray photons that we are unable to eliminate from thermal population of the cavity. Through the same interaction and dispersive shift, these photons can cause dephasing. From the Hamiltonian Eqn. 3.3.2

$$H_{\text{eff}}/\hbar = \omega_c a^\dagger a + (\omega_q - \chi a^\dagger a) b^\dagger b - \frac{\alpha}{2} b^\dagger b^\dagger b b, \quad (7.33)$$

we see that the qubit frequency shifts by  $\chi \sim 2g^2/\Delta$  for each photon in the cavity, decreasing with large detuning  $\Delta$  or small coupling  $g$ . In one classic example [102], a coherent measurement tone applied to the cavity creates a superposition of photon states of the cavity, each with its own AC-Stark shift, giving the qubit a linewidth that corresponds to the measurement rate of the qubit state. In their weak dispersive case where  $\chi/\kappa \ll 1$ , the strength of the photon measurement is diminished. In this limit, a coherent tone gives

$$\Gamma_\phi = 4\theta_0^2 \bar{n} \kappa \quad (7.34)$$

where  $\theta_0^2 \approx \chi^2/\kappa^2$  accounts for the information per photon which is carried away at a rate  $\bar{n}\kappa$  proportional to mean transmitted photon number  $\bar{n}$ . A cavity thermal bath with population  $\bar{n} = 1/(\exp(\hbar\omega_c/kT) - 1)$  from effective temperature  $T$  and cavity frequency  $\omega_c$  induces dephasing at rate\*

$$\Gamma_\phi = \bar{n}(\bar{n} + 1) \frac{\chi^2}{\kappa} \quad (7.35)$$

and limits coherence to less than a microsecond for a quality factor  $Q = 150$  cavity connected to a bath at 70 mK, used for the original study in flux qubits [103]. These are not unreasonable parameters for classic planar transmon cavities, fabricated to have low  $Q$  cavities for readout. The most accurate measurements to date come from the analysis of resonant vacuum-Rabi

---

\* The quadratic dependence arises in the derivation [103] for thermal fields because of the larger variance in photon number for a given  $\bar{n}$  compared to the coherent drive. It only applies in the weak limit. See also Eqn. 8.7

peaks [104], where there is an upper bound of  $\bar{n} < 0.003$  for some experiments; however, the temperature of the internal baths has not been well-studied.

In contrast, most 3D transmon experiments have been designed with cavity decay rate  $\kappa$  reduced to ensure qubit lifetimes are not shortened through the Purcell effect. For the fundamental mode of the cavity typical parameters are  $\chi/2\pi \approx 10$  MHz, while  $\kappa/2\pi \approx 10$  kHz, such that photon dephasing is similar to the strong fluctuator limit. In fact a careful examination in Ch. 8 demonstrates that  $\chi \gg \kappa, \gamma$  for more than just the fundamental cavity mode, significantly affecting predictions for coherence. More recent experiments have even used the photon number split spectrum with selective addressing of the qubit conditional on photon state, or included the anharmonic cavity as a new manifold. It is important to note that here proper dynamical decoupling similar to Sect. 7.3.1 is only achieved when echo pulses are fast enough to cover the full manifold of photon number states (in addition to being more frequent than  $\chi$ ), so slow pulses may be particularly ineffective at cancelling photon induced dephasing.

In the next chapter, we explore photon induced dephasing in the strong dispersive regime. Here, each photon transiting the cavity acquires complete information about the qubit state (the information per photon saturates) and the dephasing rate is no longer proportional to  $\chi^2/\kappa$ , but is simply  $\bar{n}\kappa$ . Photon dephasing is the primary source of decoherence in the first 3D transmons, and although the rate per photon saturates in this regime, the potential for decoherence from all modes of the cavity requires our extra diligence in keeping connected baths cold.

## CHAPTER 8

---

### Photon Induced Dephasing

---

**I**N this chapter we investigate the nature of photon induced dephasing in the 3D transmon. Although the energy relaxation time  $T_1$  of qubits in the new 3D geometry increased by over an order of magnitude with respect to that of planar transmons, their  $T_\phi$  phase coherence time increased by a smaller factor. In seeking to explain this discrepancy, and identify the cause, we make use of their excellent performance characteristics to perform new measurements of the cavity as well, and quantitatively examine of the role of photon shot noise in dephasing the transmon.

Historically the flux of photons from a thermal bath has been known to affect qubit coherence times. This was first demonstrated [103] in flux qubits, where a variation in dispersive  $\chi$  with a thermalized mode lead to increased dephasing rates in a flux qubit. While decoupling from the multiple mode description of the electromagnetic environment [105, 106] has been one fruitful way to eliminate dissipation, such a focus can have side-effects that increase the residual decoherence if one is not careful!

In this chapter we observe photon induced dephasing using several different techniques [107], from applying noise at the cavity transition frequency to physically raising the temperature of the cavity and of all of its linked thermal baths. Furthermore, we make use of a novel moveable coupler to modulate the rate of this process, directly manipulating the interaction between bath and cavity. We learn that indeed, even a very small number of photons could efficiently

dephase the qubit. In addition, confirming our growing understanding of the multi-mode sensitivity of our devices [50], we found that photons in more than one mode affected qubit coherence. This implies that exquisite care should be taken over a wide band of frequencies to keep temperatures low and photons few, and that contemporary best cryogenic practices were either not carefully followed or insufficient and in need of updating. These results also provide evidence that flux noise and critical current noise are not the most important issues to address for evolutions of our design in the near future. Finally, they may reveal that the limit to coherence of the early 3D qubit samples is provided by charge noise or some other slow fluctuating noise.

We begin by reviewing photon induced dephasing in the strong-dispersive limit. We then demonstrate that the dephasing rate of a qubit is directly tied to the cavity decay rate and average photon number by adjusting each over an order of magnitude, observing qubit pure dephasing rates from 1  $\mu\text{s}$  to nearly 100  $\mu\text{s}$ . We confirm that qubit dephasing follows theory first with photons we inject (calibrated in a process similar to Section 6.2.4) and then by generally raising the temperature of the apparatus. Finally we discuss the transition from strong to weak dephasing and draw conclusions based on the change in qubit coherence with cavity  $\kappa$  even in the seeming absence of photons.

## 8.1 Strong Photon-Induced Dephasing

In the spirit of Sect. 7.4.3, let us consider photon-induced dephasing in the strong-dispersive limit. In a transmon which is coupled to a cavity, a change in the cavity photon number shifts the qubit transition frequency by  $\chi$ . A transmitted or reflected photon contains in its frequency or phase shift information about the qubit, such that this change is a measurement of its state. Alternatively, such an event results in a random accumulation rate of phase in superpositions which takes  $|\psi(t_0)\rangle = \frac{1}{\sqrt{2}}(|g, 0\rangle + |e, 0\rangle)$  to:

$$|\psi(t)\rangle = \frac{1}{\sqrt{2}}(|g, 1\rangle + e^{i\chi(t-t_0)}|e, 1\rangle), \text{ for } t > t_0 \quad (8.1)$$

and which if undetected effectively dephases the qubit. Classically, we see this as the diffusion of the accumulated qubit phase as it drifts about a center frequency. When the accumulation is many times the natural cavity and qubit linewidths ( $\chi \gg \kappa, \gamma$ ), this is observed as altogether a shift in qubit frequency.

The transmon in a 3D cavity was designed to have approximately the same  $\chi$  as original

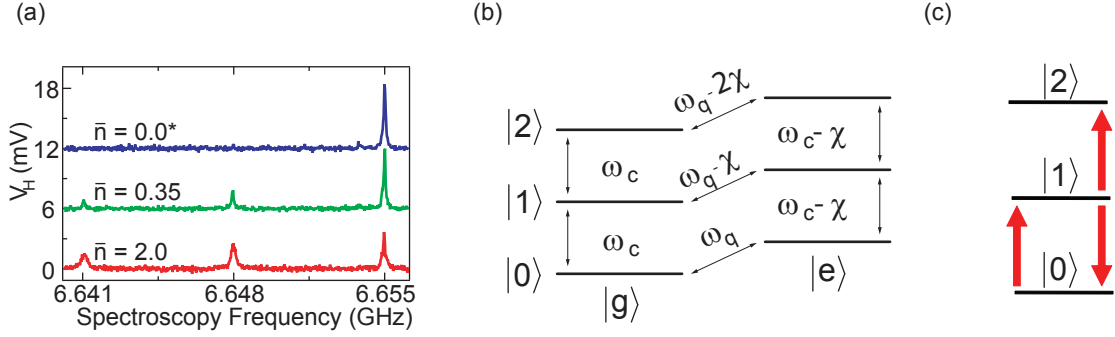


**Figure 8.1:** a) Spectroscopy of qubit  $J_3$  showing a photon number splitting with  $\chi/2\pi = 7$  MHz, with various mean photon numbers  $\bar{n}$ . (\*) As a reminder, we measured steady-state excitations of  $P(1) \approx 0.02$  in the cavity, at base temperatures and without extra driving during the experiment. b) The level diagram of the combined qubit and cavity system, describing the qubit  $|g\rangle \rightarrow |e\rangle$  transition shift by  $-\chi$  for each cavity photon, and the corresponding shift in cavity transition frequency. c) Photon number has  $2N + 1$  ways to change, enhancing dephasing when starting with high  $N$ .

transmons in coplanar waveguide architectures, but due to the virtues of its geometry suffers from dramatically smaller decoherence rates  $\gamma_1$  and  $\gamma_2^*$ . This leads to well-resolved peaks in the qubit spectrum (as seen in Fig. 8.1) with  $\hbar\chi$  larger than  $\kappa, \gamma$  often by a factor of 1000. While this allows conditional manipulation of the qubit depending on cavity photon number, it also saturates the information which is extracted during a photon transit and the dephasing that accompanies it (alternatively, the presence of a photon for even a small fraction of  $1/\kappa$  leads to a rapid phase accumulation). Consequently, the original design parameters of the 3D transmon leave it exposed to photon induced dephasing in the presence of a heat bath, but now at an increased level of sensitivity as other decoherence mechanisms have been removed.

## Thermal Baths

A cavity connected to a thermal bath obeys a system of equations which govern the probability  $P(N)$  of a harmonic oscillator having  $N$  photons [52]:

$$dP(N)/dt = \kappa(\bar{n} + 1)(N + 1)P(N + 1) + \kappa\bar{n}NP(N - 1) - \Gamma_{\text{out}}P(N) \quad (8.2)$$

where the cavity decay rate  $\kappa$  is the inverse of its decay time  $\tau$ ,  $\bar{n}$  is the average number of photons, and

$$\Gamma_{\text{out}} = \kappa [(\bar{n} + 1)N + \bar{n}(N + 1)] \quad (8.3)$$

combines spontaneous emission with stimulated emission due to incident thermal photons.

Because in the strong dephasing limit each change in photon state carries complete information about the qubit state, the pure dephasing rate becomes  $\gamma_\phi = \Gamma_{\text{out}}$ , the rate at which the cavity photon number changes. This rate is intimately tied to both the cavity decay rate  $\kappa$  and  $\bar{n}$ , the average photon number in the cavity, and in order to demonstrate this we adjust literally by hand the cavity coupling *in situ*, altering the rate of dephasing events. In the remainder of this chapter, we compare and contrast the measurements of a single qubit as its 3D cavity is decoupled from the environment and thermal excitations in the cavity are either simulated or created, imposing dephasing.

## 8.2 Photon Injection

We may create a heat bath connected only to the cavity by using an IQ mixer to shift RF noise up to the cavity frequency using a microwave tone, as described in Section 4.11. This simulates blackbody or Johnson-Nyquist noise but over a small bandwidth, where the effective temperature of the input mode of the transmission line has temperature  $T$  and a mean photon number  $\bar{n}_{\text{in}}$  given by the Bose-Einstein population probability  $P_{BE}(T) = 1/(\exp(\hbar\omega/k_b T) - 1)$  of that mode. We can raise the effective cavity temperature to over 1 Kelvin without directly driving any transitions of the qubit by restricting the noise bandwidth to be  $\sim 100$  MHz and cover  $\omega_{01}^g, \omega_{12}^g, \omega_{23}^g, \omega_{01}^e$ , etc. while remaining several GHz from  $\omega_{ge}^0$  (see Fig. 6.7 and Fig. 8.1b).

The average number of photons excited in the cavity itself,  $\bar{n}$  is proportional to the incident power within the cavity bandwidth,  $\kappa$ , and as we saw in Ch. 3, with  $\bar{n} = AP_{BE}(T)Q/Q_c$ .

As described by  $\bar{n}$ , at any given time the photon number fluctuates, with a probability distribution determined by detailed balance of the harmonic oscillator population [52]:

$$P(\bar{n}, N) = \bar{n}^N / (\bar{n} + 1)^{N+1} \quad (8.4)$$

and places the cavity into a mixed state independently of the qubit.

$$\rho = \sum_N \left[ \bar{n}^N / (\bar{n} + 1)^{N+1} \right] |N\rangle \langle N| \quad (8.5)$$

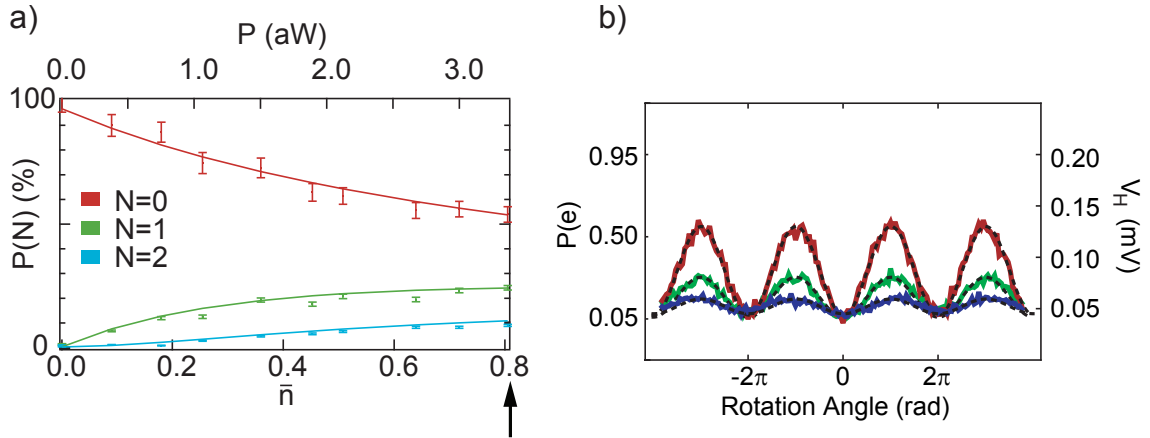


**Figure 8.2:** a) Rabi calibration of thermal state. Power within the cavity bandwidth is directly proportional to  $\bar{n}$ , and the probability for  $N$  photons follows a thermal distribution. b) An example Rabi set for  $\bar{n} = 0.8$ , showing the progressively decreasing occupation of  $N=0$  (red),  $N=1$  (green), and  $N=2$  (blue). In the axes we note that the equilibrium excitation of the qubit for the duration of the experiment was  $\approx 5\%$

Because each distinct number produces a different shift in qubit transition frequency, we may determine these probabilities by interrogating the qubit.

We first calibrate our measurement of the cavity photon state via a procedure similar to Sect. 6.2.4 as seen in Fig. 8.2. Then, for each input power, we may measure the probability that there are  $N$  photons in the cavity, by addressing these transitions using long pulses on the photon peaks of the qubit in a power Rabi experiment to confirm the probability distribution Eqn. 3.107. By combining experiments for the different  $N$  we can find a scaling from voltage in the homodyne readout signal (see Sect. 6.2.2) to probability, and power at the top of the fridge to  $\bar{n}$  inside the cavity.

Repetitions of this procedure yield a scaling factor which varied by  $\sim 5\%$ , primarily due to the variance in full-scale readout, and most clearly evident in the  $N = 0$  Rabi experiment. The full-scale difference in homodyne readout voltage between qubit  $|g\rangle$  and  $|e\rangle$  may fluctuate or even disappear, necessitating the use of averages simply to obtain a correct reading. In addition, for any given experiment, the cavity has been projected into a photon state  $N$  – not a superposition or fraction – by the first selective pulse and simply due to binomial statistics, we need a certain number of averages to reconstruct accurately the probability of occupation.

### Dephasing in Ramsey Experiments

We studied qubit J<sub>3</sub>, one of the first few qubits fabricated for the new 3D geometry in our laboratory. Its  $\chi/2\pi = 7$  MHz meant that the light shift per photon could be 1000 times larger than the qubit linewidth, which was varied from 5 – 12 kHz, and the cavity linewidth  $\kappa/2\pi = 6 - 120$  kHz. We found that the qubit  $T_1$  was unaffected by  $\kappa$  and the Purcell effect within the range of our variable manipulator, but that its  $T_2^*$  and  $T_{2E}$  would change in illuminating ways both with and without our stimulus.

For a given  $\bar{n}$ , Eqn. 8.1 gives the rate of change of the cavity state and thus, in the strong-dispersive regime, the pure dephasing due to photon shot noise in the qubit frequency. The consequences are evident in our Ramsey experiments, where the absorption (emission) of a photon from the input mode (cavity) completely measures the qubit state, projecting any superposition and providing full information in the absorption (emission) spectrum.

Our Ramsey experiments begin with a cavity whose  $TE_{101}$  mode is in a thermal state, due to the continuous application near  $\omega_{101}$  of microwave noise. Using gaussian pulses with  $\sigma_t = 100$  ns, we first select for an empty cavity or the starting photon number with a  $\pi/2$  pulse on the  $N$  photon number split peak. A second selective pulse on the same photon number after a stepped waiting time completes the Ramsey experiment. For the case of  $N = 0$ , and 1, we can plot the dephasing rate  $\gamma$  versus  $\bar{n}$  for many values of  $\kappa$ . Here we saw good agreement between theory and experiment (see Fig. 8.3), where the increase of the dephasing rate of the qubit was equal to the rate of change of the photon state. Ramsey experiments on  $N=2$  and higher are infeasible through creation of a thermal state: the contrast decreases exponentially with an accompanying factor of  $(2N + 1)\bar{n}\kappa$  increase in dephasing rate.

In fact the same procedures can be followed for not only  $TE_{101}$  but  $TE_{103}$  as well, which we find to have  $\chi_{103}/2\pi = 1$  MHz, still much greater than  $\gamma, \kappa$ . This confirms that our qubit is strongly coupled to several modes of the cavity, as predicted in Ch. 3 and that we must take care to use isolators and broadband attenuation that covers more than just the obvious  $\omega_{101}$  and  $\omega_{ef}$  frequencies of the cavity and qubit.

In the next section we will cover an experimental detail of the Ramsey experiments in the presence of photon noise.

### Post-selection by readout

Initial conditions of the Ramsey experiments are prepared by simply waiting for stabilization in steady-state. The selectivity of the first  $\pi/2$  pulse ensures that only repetitions of the

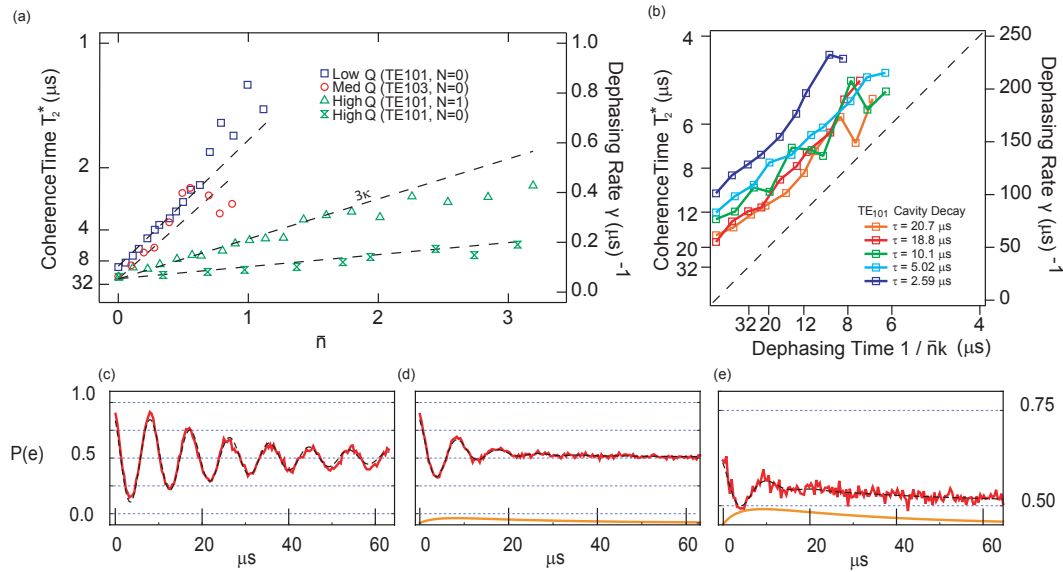


**Figure 8.3:** Qubit dephasing due to photon noise. (a) Qubit coherence time, determined from Ramsey experiments on the  $N = 0$  or  $N = 1$  ( $\Delta$ ) photon peaks, as a function of both cavity  $Q$  and  $\bar{n}$ . The dashed lines are theory, with an offset due to residual dephasing. Each has a slope proportional to  $\kappa$  (or  $3\kappa$  for  $N = 1$  experiments), according to Eqn. 8.1. The (o) are coherence times vs. population in TE<sub>103</sub> mode, which also dephases the qubit. b) Universal dephasing plot: an alternative presentation of our measurements of qubit dephasing versus noise. Here the horizontal axis is  $1/\bar{n}\kappa$ , scaled for each trace, which according to Eqn. 8.1 we expect to be equal to  $T_\phi$  for the qubit. The vertical offsets correspond to residual dephasing even for  $\bar{n} = 0$ , which will be discussed in Section 8.4. (c) Ramsey with no noise injected, fundamental mode  $Q = 1 \times 10^6$ , and  $T_2^* = 26$  μs. The solid line is a fit with an exponentially decaying sine. (d) A Ramsey with moderate noise. Contrast and  $T_2^*$  are reduced. Fundamental mode  $Q = 2.5 \times 10^5$ ,  $\bar{n} = 0.25$ ,  $T_2^* = 7.7$  μs. (e) Ramsey with high noise. Fundamental mode  $Q = 1 \times 10^6$ ,  $\bar{n} = 3.1$ ,  $T_2^* = 5.2$  μs. Our selective ( $N = 0$ ) pulses produce a loss of contrast and a non-oscillating signal addition (orange) as photon population returns to a thermal distribution. The dashed black line is a numerical simulation (see Appendix C)

experiment that begin with the specified value of  $N$  add contrast to the Ramsey interference fringes, however both  $\pi/2$  pulses are photon-state selective, to simplify pulse calibration.

As one consequence of this scheme, the contrast of our Ramsey traces is proportional to the population  $P(N)$  of the peak whose coherence times we are measuring; more repetitions fail to add contrast as  $1 - P(N)$  increases. In addition, because the second  $\pi/2$  pulse is selective, an additional signal is present in averaged traces, which can be described by:

$$P_B(t) = \frac{1}{2} \frac{\bar{n}}{(1 + \bar{n})^2} \frac{1 - e^{-\kappa t}}{1 - \frac{\bar{n}}{1 + \bar{n}} e^{-\kappa t}} \cdot e^{-t/T_1} \quad (8.6)$$

where  $T_1$  is the qubit energy relaxation time. This is due to  $T_1$  decay and photon number transitions during the experiment, and appears in Fig. 8.3; the effect must be removed from the trace in order to recover the true dephasing rate, with analysis in further detail found in Appendix C.

The importance of this effect lies in the fact that it can occur as well for any perturbation that strongly splits the qubit frequency. For example, charge dispersion in the transmon creates two frequencies depending on the parity of the number of quasiparticles in the junction. If a quasiparticle tunnelling (or any other event which takes the qubit temporarily out of our state space) occurs between Ramsey pulses and the charge dispersion is more than  $\kappa$ , we may expect to see similar effects.

## Technical Discussion

The photons here are from non-equilibrium baths, since we generally expect that modes at 20 mK have exponentially suppressed excited populations. However, because the link between room temperature and the base plate of the fridge is only sparingly attenuated (due to the need for efficient drive or readout), it is more appropriate to think in terms of effective number than of effective temperature.

It is important to note that the mere presence of photons in the cavity doesn't automatically cause decoherence. For example, in the case that the cavity state is stable ( $\kappa \rightarrow 0$ ), a Ramsey on a photon peak does not experience an intrinsic decoherence, because no measurement is performed. Even for a non-selective pulse with wide bandwidth over several peaks, a superposition acquires phase at different rates but not in an irretrievable way. Using a Hahn echo, for example, cancels individually the phase acquired by each portion, such that the final Ramsey experiment sees no ill effects from the photons. On the other hand, we cannot

avoid dephasing by simply disconnecting the visible ports of our cavity, by perhaps filling them with superconductor. The cavity retains an internal quality factor  $Q_i$  with temperature  $T_i$  which provides a dephasing heat bath.

Because each mode contributes, we must be wary of accidental population of higher frequency modes outside the operating range of the circulators, and as long as  $\chi > \kappa$  each photon transit carries complete information and should be avoided, and as we have seen there may be many modes that couple in this regime. In fact, the strong coupling between the qubit and  $TE_{103}$  enables state readout, with 50% fidelity, using the same high-power pulses we use on the fundamental mode.

Ramsey experiments are rarely the final goal in a laboratory, and the dephasing we see here should carry over to other experiments. As a subtlety however, here the Ramsey decay is in a sense because of the selective pulse completely missing the qubit; it is a consequence of the measurement and recording. A short  $\pi/2$  pulse would have instead captured the more essential dephasing, with loss of Ramsey contrast without loss of signal contrast.

### 8.3 Temperature Dependence

When the temperature of the entire apparatus is uniformly raised, we can use Eqn. 8.1 and the summation  $\gamma_\phi^{\text{tot}} = \sum \gamma_{\phi,i}$  to make specific predictions about the effects on coherence. A temperature  $T$  populates all harmonic oscillators with a population  $P_{BE} = 1/(\exp(\hbar\omega/k_B T) - 1)$ , decreasing at higher frequency. In particular, it places every mode of the cavity in a mixed thermal state. In Fig. 8.4, we show this coherence time for a cavity coupler setting with low Q of  $\tau = 2 \mu\text{s}$  alongside one with  $\tau = 20 \mu\text{s}$ . Occupation in the  $TE_{101}$  and  $TE_{103}$  modes explain the majority of the dephasing, confirming our model.

These considerations limit the allowable temperature range of our devices, should we wish them to have a certain amount of coherence. For a single mode dominating qubit coherence in the strong-dispersive regime,  $T_\phi = \tau/\bar{n}$ . In particular, a  $100 \mu\text{s}$  coherence time is impossible with cavity population of 10% when  $\tau = 10 \mu\text{s}$ , 1% when  $\tau = 1 \mu\text{s}$ , or 0.1% when  $\tau = 100 \text{ ns}$ \*. This total thermal decoherence rate is shown as the red dashed line in Fig. 8.4b, for typical parameters. Since these modes have  $\hbar\omega_n \gg k_B T$ , the predicted dephasing time is in excess of 100 microseconds below 80 mK due to the exponentially suppressed number of blackbody

---

\* Motional narrowing begins to reduce the severity of photon-induced dephasing at  $\chi = \kappa$ , and usually around  $\tau = 100 \text{ ns}$  for typical qubits.

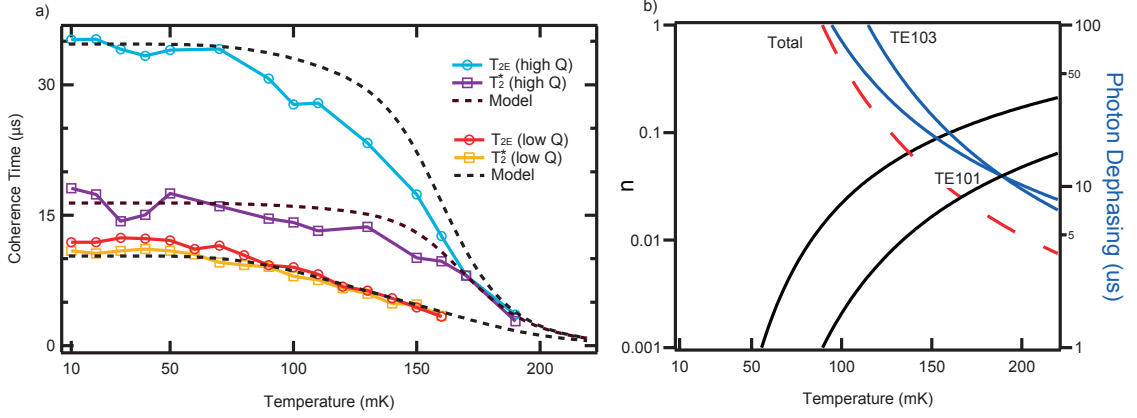


**Figure 8.4:** (a) Decoherence due to thermal photons. The coherence times extracted from Ramsey ( $T_2^*$ ) and Hahn echo ( $T_{2E}$ ) experiments measured as a function of cryostat temperature. To model dephasing (dashed lines), we predict population in the  $TE_{101}$  and  $TE_{103}$  modes of the cavity. Then, we sum the total dephasing rate using the measured quality factors for each mode (High Q:  $\tau_{101} = 20 \mu s$ ,  $\tau_{103} = 4 \mu s$ ; Low Q:  $\tau_{101} = 2 \mu s$ ,  $\tau_{103} = 400 ns$ ). For high Q, the use of a Hahn echo pulse leads to a large  $T_{2E}$  because either the photon state has much longer correlation time or the remaining dephasing similarly occurs at low frequencies (see Sect. 7.3.1). Although the decline in  $T_1$  (see Sect. 6.2.8) [108] contributes to the trend, population in both  $TE_{101}$  and  $TE_{103}$  are needed for a good fit. A more general description based on population in all modes might describe the residual dephasing. (b) Bose-Einstein population of the first two odd- $n$   $TE_{10n}$  modes at 8 and 12.8 GHz (green) and the coherence limits they impose individually (blue) and collectively (dashed red) for the low Q values measured above.

photons. However, since any particular mode coupling to the qubit in the strong-dispersive limit may have a relatively fast decay time  $\tau$ , even very small ( $\sim 10^{-3} - 10^{-2}$ ) non-thermal populations  $\bar{n}$  could easily satisfy  $\bar{n}\kappa \gg 1/2T_1$ , limiting the coherence through pure dephasing alone to  $T_2^* \approx 1/\gamma_\phi = \tau/\bar{n}$ .

In fact, the reduction of photon induced dephasing for this device reveals the presence of much lower-frequency dephasing noise which is highly correctable by a Hahn echo, which is apparent in the spectacular improvement with echo in the high Q trace. Also seen in Fig. 8.6c, this suggests either the photon state has much longer correlation time or the remaining dephasing (such as charge noise) similarly occurs at low frequencies.

## 8.4 Generalization

For fast enough cavity decay rates, the assumptions made at the beginning of this Chapter break down. As  $\kappa$  increases beyond  $\chi$  the qubit is no longer number-split, and similarly a photon transit neither completely dephases it nor does it contain complete information about the qubit state. In this limit in fact the random accumulation of phase due to qubit frequency shift is motionally narrowed, with the dephasing rate becoming:  $\gamma_\phi \approx 4\bar{n}(\bar{n}+1)\chi^2/\kappa$ , significantly reducing the importance of the effect. In general, as recently derived [109, 110], the dephasing rate of a qubit connected by rates  $\kappa_j$  with baths of mean photon number  $\bar{n}_j$  is:

$$\gamma_\phi^{tot} = \frac{\kappa}{2} \Re \left[ \sqrt{\left(1 + \frac{2i\chi}{\kappa}\right)^2 + \left(\frac{8i\chi \sum_j \bar{n}_j \kappa_j}{\kappa^2} - 1\right)} \right] \quad (8.7)$$

When the qubit is no longer photon number-split due to either a larger  $\gamma$  (as in planar transmon experiments) or  $\kappa$  (perhaps for fast qubit readout) the cavity decay experiment must be replaced with a frequency-domain low-power spectroscopy measurement of  $\kappa$  and photon number is calibrated via the Stark shift [102].

### Weakly coupled modes

Several harmonics of the 3D cavity are coupled weakly to the qubit by symmetry, among them the  $TE_{102}$  and  $TE_{104}$  modes at 12.867 GHz and 15.742 GHz. We can apply noise as above and see dephasing, even if we cannot measure  $\bar{n}$  in pulsed experiments. Additionally, we can only simulate the  $Q_c$ , which may reflect much of the noise power. Fig. 8.5 shows the scaling of dephasing rates these small  $\chi$  modes, which although quadratic in  $\bar{n}$  as expected could simply be represent the heating of fridge attenuators. The presence of both high and low quality factor modes could be utilized for dispersive readout without the complications of a physically separate cavity.

### Residual Dephasing

One striking consequence of Eqn. 8.7 is the existence of a global maximum in dephasing, a set of parameters from which any change in  $\kappa$  or  $\chi$  will lead to increased coherence times. In fact this configuration, where  $\chi = \kappa$  is often used for dispersive readout of the qubit. But it has implications in the interest of increasing qubit coherence times: does a cavity need to be high Q or can it be low Q for maximum qubit coherence? Photon dephasing can be

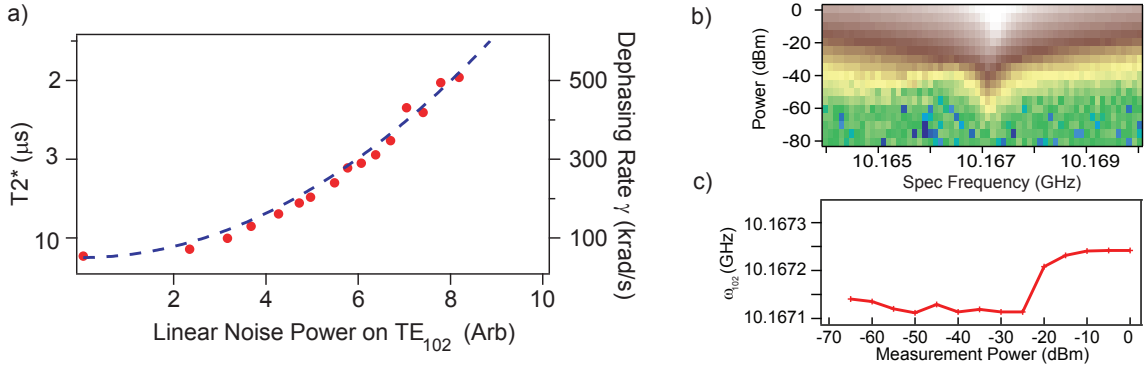


**Figure 8.5:** Noise on higher modes. a) TE<sub>102</sub> at 10.167 GHz has  $g/2\pi \sim 20$  MHz. Because absolute photon number calibration was not performed (and  $Q_c$  was unknown), the quadratic [103] is a guide to the eye. Not shown, TE<sub>104</sub> is at 15.742 GHz with  $g/2\pi \sim 30$  MHz and has a similar sensitivity to incident power. b) High power spectroscopy of the cavity leads to a removal of the cavity-qubit dispersive shift, as typical for readout using TE<sub>101</sub> c) The dispersive shift is small and notably of opposite sign to the readout cavity  $\chi_{01}$  (see Fig. 6.5)).

minimized as long as you choose between the two. For  $\chi/\kappa \gg 1$ , photon measurements are rare but devastating, while for  $\chi/\kappa \ll 1$ , the entanglement between the two systems is small and the total measurement rate induced by the environment is small. In Fig. 8.6 we show a model describing this phenomenon for a fixed exterior mode  $T$  or photon number  $\bar{n}$ .

In the device studied in this Chapter, we observed a monotonic increase in  $T_2^*$  as the output port coupling quality factor increased. Assuming the dominant source of dephasing is non-equilibrium photons from a noisy amplifier or improper heatsinking, there are consequences to that source being of broadband origin compared to  $\kappa$ . The increase indicates it is the output mode itself that provides the non-equilibrium photons and that dephasing is caused by a mode with a  $\chi > \kappa$ , such as that for the TE<sub>101</sub> or TE<sub>103</sub> for example. It also suggests that it is not flux noise or critical current noise which limit many of our early 3D qubits, but photon noise itself, as it is difficult to draw a stronger connection between the  $T_2^*$  behavior and these mechanisms than to  $\kappa$  and photon induced dephasing.

Fig. 8.6a shows that for a thermal bath connected to the input port, coherence times only decrease as the output coupler is extracted from the cavity, decoupling a hypothetically cold mode. In contrast, decoupling from a hot output mode decreases both  $\bar{n}$  and  $\kappa$ , which will suppress  $\gamma_\phi$  if  $\chi > \kappa_c$  for the coupler. Sweeping the coupling of a port has great utility not only in allowing us to assign the location of a thermal bath, but also to determine the dispersive shift of the qubit with the mode responsible for the dephasing.

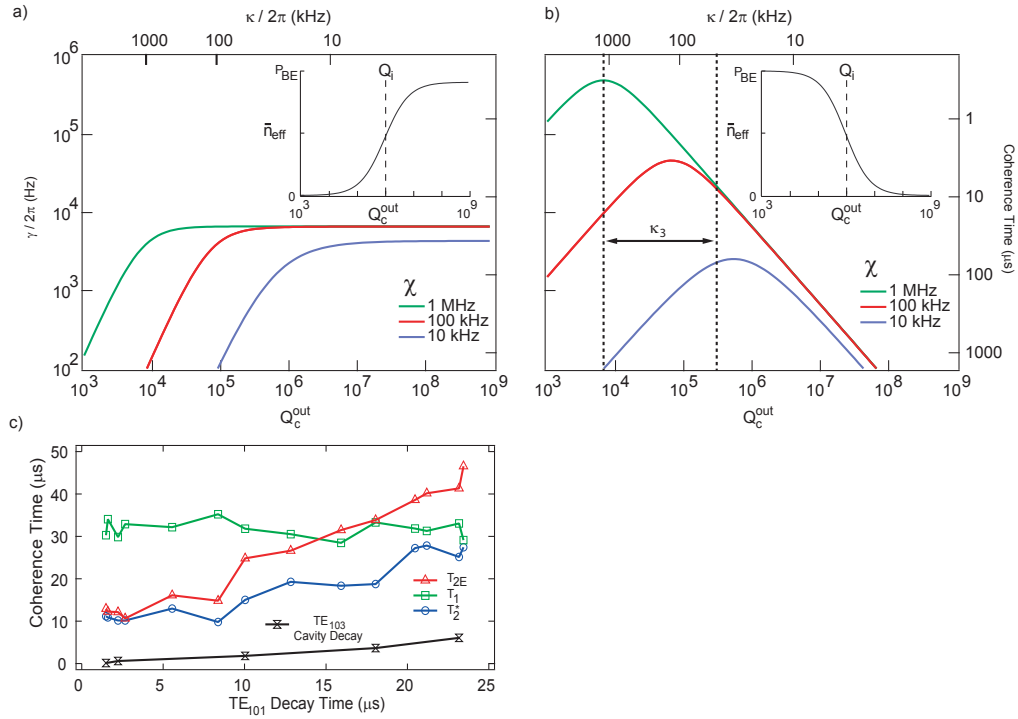


**Figure 8.6:** Control of the coupling quality factor is important for diagnosing the source of incident photons. a) When, as in this experiment, decoupling the output port while connected on the input (or internal) port to a heat bath which emits radiation at a wideband compared to kappa, dephasing rates of the qubit only increase. b) The same experiment, with heat bath on the output (variable) port. Along with c), this suggests the qubit is coupled to a hot cavity mode with  $\chi/2\pi < 1$  MHz c) Coherence times versus  $TE_{101}$  mode decay  $\tau$ . The  $TE_{103}$  cavity, which naturally decays more strongly through the couplers, increases in  $Q$  as the entire resonator is decoupled from our coaxial lines. While  $T_1$  is nearly constant due to the large qubit detuning from the cavity, its  $T_2^*$  and  $T_{2E}$  increase as the coupling pin is withdrawn from the 3D resonator. This is consistent with diminishing dephasing from cavity modes with  $\kappa < \chi$ , where a photon transit strongly measures [111] the qubit state.

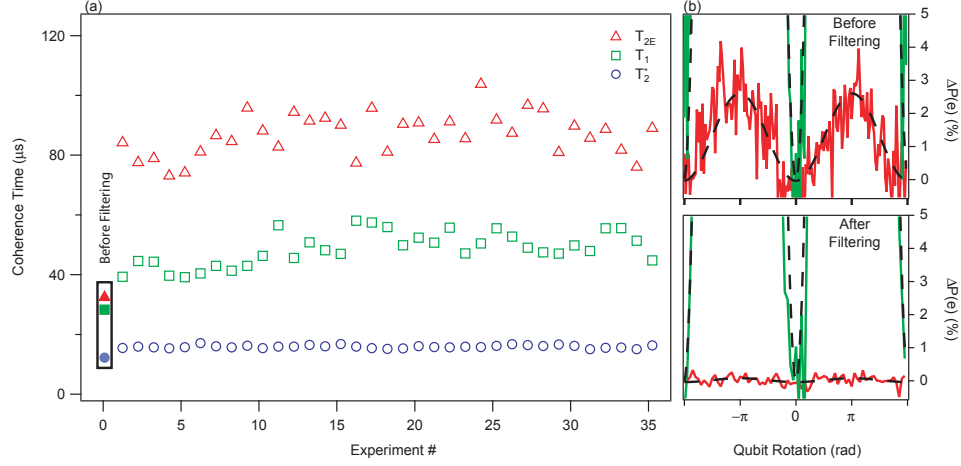


**Figure 8.7:** (a) Series of non-simultaneous measurements of  $T_1$ ,  $T_2^*$ , and  $T_{2E}$  for qubit J5. The filled points represent the original measurements with only absorptive low pass filters. The open points were taken after the addition of reflective low pass filters. (b) Cavity population before and after adding reflective filters. Similar to the measurements in Fig. 8.3, the horizontal axes show the qubit rotation angle while the vertical axes are scaled to show the change in qubit excited state population. The lower (red) traces are Rabi experiments on the N=1 photon peak of the qubit, while the upper (green) traces address the N=0 transition.

## Modifications

In order to verify a solution to the problem of unexpected photon measurement, we tested a qubit of similar design to the one studied in the main text. Qubit J5 had  $\omega_q/2\pi = 6.384$  GHz for a cavity with  $\omega_c/2\pi = 7.82$  GHz and fixed couplers leading to a cavity decay time  $\tau = 5.5$   $\mu$ s. We initially measured a  $T_1 = 28$   $\mu$ s,  $T_2^* = 12$   $\mu$ s, and  $T_{2E} = 32$   $\mu$ s, with qubit excited state population  $P(e) = 6\%$  and cavity photon occupation of  $P(1) = 2.7\%$  (which, it should be noted, is sensitive to cavity population in any mode with  $\chi/2\pi \approx 5$  MHz). These measurements were done using an apparatus equivalent to Fig. 4.3 with the addition of prototype lossy low-pass filters on both the input and output ports, adjacent to the cavity. After transferring the device to a new cryostat and installing both the low-pass absorptive [58] (3 dB in band and 15 dB at 40 GHz) and reflective (KL Microwave low-pass, 50 dB rejection at 14 GHz) filters we measured a  $P(e) = 3.3\%$  and  $P(1) = 0.12\%$ , and verified that the cavity decay time remained unchanged.

We measured a series of coherence times independently in this new configuration in order to place a lower bound on the dephasing time. As shown in Fig. 6, we obtained average

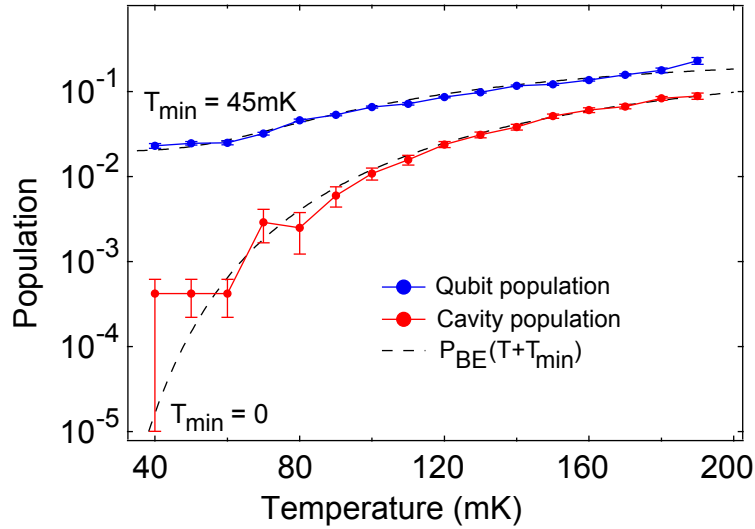


**Figure 8.8:** After proper thermalization, qubit SP1 had undetectable cavity population at the base temperature of the fridge; here it measured  $T_1 = 87 \pm 7 \mu\text{s}$  and  $T_{2E} = 132 \pm 12 \mu\text{s}$  (data provided by L. Sun and A. Petrenko.)

$T_1 = 49 \mu\text{s}$ ,  $T_2^* = 16 \mu\text{s}$ , and  $T_{2E} = 87 \mu\text{s}$ . With such a large ratio  $T_{2E}/T_1 = 1.8$ , the dephasing time can depend strongly on the accuracy of our measurements. We estimate the residual dephasing rate not corrected by a Hahn echo to be  $(1.2 \pm 1.5) \text{ kHz}$ , with  $800 \mu\text{s}$  for a best estimate of the dephasing time with echo.

These measurements suggest that extra heatsinking and filtering measures have mitigated the problem of photon induced dephasing from exterior thermal baths, although they do nothing for and may even exacerbate the effect of a lossy interior. Careful budgeting of power and dissipation is necessary to avoid its reemergence.

## Conclusions and Epilog

We have performed experiments involving precise thermal photon populations to quantitatively induce qubit dephasing in good agreement with simple theory. The sensitivity of the qubit to photons at many frequencies requires that we either keep all modes of the cavity in their ground state, or else minimize the influence of non-thermal populations by reducing their measurement rate [20]. Inclusion of the cavity harmonics in dephasing calculations leads to an understanding of the earlier, anomalous, temperature-dependent decoherence in our devices [82]. Finally, we see that residual photons in our 3D cavity likely mask the

intrinsic coherence time of the Josephson junction, suggesting they may do so for many other superconducting qubit designs [112, 113], quantum dots [114], and more generally any Quantum Information system coupled to a bosonic mode [115]. As qubit linewidths shrink in the future, other effects such as quasiparticle parity [90, 116?] or far in the future even interactions with nuclear spins may further split the qubit spectrum, inducing dephasing in a similar manner.

We have identified and resolved the mechanism which prevented early 3D transmons from matching their dramatic increase in  $T_1$  times with an equally improved dephasing times. In fact, the inclusion of better filtering and thermalization has led to the smallest population measurement to date of one of our transmons, seen in Fig. 8.8. The accompanying coherence measurements, in which  $T_1$  and  $T_{2E}$  are well above 100  $\mu s$ , validate our conclusions about dephasing in the first 3D transmons, and suggest that photon induced dephasing can be eliminated with best practice cryogenic techniques.

## CHAPTER 9

---

### Conclusions and Outlook

---

**T**HE The experimental work in this thesis has been the study of two radically simple attempts to improve coherence in solid-state quantum devices. In the first (Ch. 5), we tried to coax natural electron spins to couple more strongly than they are typically inclined and in the second (Ch. 6) we removed coupling to extraneous, lossy electromagnetic modes. In this final Chapter, I will briefly describe future directions for this research, most already in progress.

#### 9.1 Expanded Hamiltonians

We often use simple energy levels for qubits and their resonators, but a truly exhaustive description of the system Hamiltonian can be intimidating. In fact, the recent modeling of resonant qubit and cavity systems using an astonishingly large state manifold was a *tour de force* [89]; the general numerical technique is robust even for more complicated situations such as the “straddling regime” [45]. On the other hand, black-box quantization (BBQ), while powerful, ignores at the moment subtle effects like charge dispersion [116] which have been directly implicated in some of the most recent 3D transmon experiments with distinct frequency fluctuations [?]. A precise account of charge dispersion in BBQ due to the multiple modes of a cavity has not been completed yet; complications arise as the larger dispersion of higher levels  $\epsilon_m$  competes with the limited hybridization of cavity and qubit modes, and it

is not clear whether the result is larger or greater than the standard  $E_J/E_C$  prediction. The expansion of the black-box quantization treatment here and its routine use at higher order promise to be immensely useful for precision planning of qubit experiments, required for design down to the last 1% or 0.1% precision of parameters.

In addition, as experiments look beyond the treatment of single devices, the development of BBQ for multiple cavities [117] or qubits [Paik et al., in prep] should be extremely useful in predicting more realistic behavior for systems that may not have a simple analytic description. Combinations of storage and readout cavities, logical and ancilla qubits, and spatially separated yet interacting systems require as much attention as single devices. For example, we may ask how far away is 99% of the qubit energy stored, and how closely can two qubits be placed? Many laboratories are considering schemes where hundreds or thousands [49] of devices form logical qubits based on their dressed interactions – at what density can this be done? Starting from the isolation of two qubits in physically separated cavities, how can their separation be relaxed in order to form dense networks for surface codes [118] or other computational topologies [119]? The effective use of commercial simulation software can help us approach these questions as well.

## 9.2 Conclusive Dissipation

One of the lessons of the 3D transmon is that the sample holder or generally neglected environment can unexpectedly be the source of problems. In Ch. 2 we detailed several mechanisms for dissipation as well as the incredibly powerful concept of participation ratio, where the rate of energy total energy loss is proportional to the linear combination of individual participation ratios and loss rates  $\gamma = \sum_i p_i \gamma_i$ , and

$$\frac{1}{Q} = \sum_i \frac{p_i}{Q_i} \quad (9.1)$$

Much time has been spent making small adjustments to experiments hoping for improvement, and a rigorous accounting using participation ratios allows for real conclusions. What is needed now is a concerted effort to quantify the quality of different materials, done in such a way that we verify their participation in the qubit mode. Amazingly, the participation can be calculated in modern finite element simulation software like HFSS, predicting  $p_i$  for substrate and cavity surfaces, bulk materials, oxide layers, conductors, and junctions. With the proper control experiments, it should be possible to identify and make appropriate

conclusions about the real sources of dissipation in superconducting qubits—not only for charge qubits, but flux, phase, fluxonium, and perhaps even quantum dots. It is a challenge to make a single qubit device as coherent as possible; what are the ultimate limitations? Our devices leverage the lossless Josephson junction and dissipationless superconducting cavities, but quasiparticle tunneling damps the qubit mode at any finite temperature [108]. Measuring cryogenic temperatures can be technically difficult; our measurements have been limited to temperatures above  $\sim 40$  mK (see Fig. 8.8), although most cavities and qubits are hotter. Can extremely decoupled qubits with long decay times be thermalized?

### 9.3 New experiments and hybrid systems

But coherence is not an end-goal, merely something that is useful for most experiments. The 3D resonator architecture enables investigations of materials science [56] and superconducting qubit design by stripping away many distracting components. Meanwhile, the transmon, which is correspondingly simple to fabricate, can be immediately put to use studying issues in quantum optics [120] and hybrid systems [23] utilizing its extraordinary coherence. Together, increased solid-state qubit coherence allows enough latency to integrate modern electronics into feedback loops with reduced degradation from fridge transit times [121], and allow for us to study things with longer natural timescales (such as critical current switching or quasiparticle generation, recombination, and tunneling [? ]). Some groups are continuing to investigate strongly coupled spin ensembles [80], but we may also try to incorporate single spins into our devices [63]; room-temperature spin experiments can have inconveniently long coherence times [77], which would be an entirely novel experience for us at cryogenic temperatures (requiring driven [? ] or tunable reset [122]). Already the maturity of circuit QED allows quantum dots coupled to coplanar resonators [24], and transmons coupled to NV center ensembles; it may be possible to translate these experiments into different cavity geometries.

### Future of decoherence

It is true there are no novel mechanisms of dephasing presented in this thesis; charge noise, photon induced dephasing, critical current noise have all been studied before. However, this work discusses dephasing as it enters a novel regime in which the fluctuator becomes entangled with the qubit, acquiring complete information on its state with every change. The first 3D

transmons are proofs of concept that retained many of the classic design parameters of planar transmons even as the increased coherence exposed sensitivities to smaller contributions from these effects. There are several immediate corrections to be made: coherence times will likely increase after raising  $E_J/E_C$  slightly and diligently correcting thermalization; the rest is left as an exercise for the reader.





**Figure 9.1:** *The thesis in abstract cookie form* (2012). Mixed media: cookie, icing, gummi bear, sprinkle, edible marker.

---

## Bibliography

---

1. M. Planck, “Ueber das gesetz der energieverteilung im normalspectrum,” *Annalen der Physik* **309**, 553–563 (1901). Cited on page 14.
2. A. Einstein, “Über einen die erzeugung und verwandlung des liches betreffenden heuristischen gesichtspunkt. (german) [on the production and transformation of light from a heuristic viewpoint],” *Annalen der Physik (1900) (series 4)* **322**, 132–148 (1905). Cited on page 14.
3. N. Bohr, “The spectra of helium and hydrogen,” *Nature* **92**, 231–232 (1914). Cited on page 14.
4. C. Cohen-Tannoudji, B. Diu, and F. Laloë, *Quantum mechanics*. Quantum Mechanics. Wiley, 1977. Cited on page 14.
5. M. A. Nielsen and I. L. Chuang, *Quantum computation and quantum information*. Cambridge University Press, Cambridge; New York, 2010. Cited on pages 14 & 111.
6. C. M. Caves, C. A. Fuchs, and R. Schack, “Subjective probability and quantum certainty,” *Studies in History and Philosophy of Science Part B: Studies in History and Philosophy of Modern Physics* **38**, 255–274 (2007). Cited on page 14.
7. R. P. Feynman, “Simulating physics with computers,” *International journal of theoretical physics* **21**, 467–488 (1982). Cited on page 15.
8. P. W. Shor, “Algorithms for quantum computation: discrete logarithms and factoring,” in *Foundations of Computer Science, 1994 Proceedings., 35th Annual Symposium on*, pp. 124–134. 1994. Cited on page 15.

9. R. L. Rivest, A. Shamir, and L. Adleman, "A method for obtaining digital signatures and public-key cryptosystems," *Communications of the ACM* **21**, 120–126 (1978). Cited on page 15.
10. C. H. Bennett and G. Brassard, "Quantum cryptography: Public key distribution and coin tossing," in *Proceedings of the IEEE International Conference on Computers, Systems and Signal Processing*, pp. 175–179. 1984. Cited on page 15.
11. S. Aaronson and P. Christiano, "Quantum money from hidden subspaces," in *Proceedings of the 44th Symposium on Theory of Computing*, pp. 41–60. 2012. Cited on page 15.
12. L. K. Grover, "Quantum mechanics helps in searching for a needle in a haystack," *Phys. Rev. Lett.* **79**, 325–328 (1997). Cited on page 15.
13. J. R. Petta, H. Lu, and A. C. Gossard, "A coherent beam splitter for electronic spin states," *Science* **327**, 669–672 (2010). Cited on page 15.
14. J. J. L. Morton, D. R. McCamey, M. A. Eriksson, and S. A. Lyon, "Embracing the quantum limit in silicon computing," *Nature* **479**, 345–353 (2011). Cited on page 15.
15. D. Leibfried, R. Blatt, C. Monroe, and D. Wineland, "Quantum dynamics of single trapped ions," *Reviews of Modern Physics* **75**, 281 (2003). Cited on page 15.
16. F. Jelezko and J. Wrachtrup, "Single defect centres in diamond: A review," *physica status solidi (a)* **203**, 3207–3225 (2006). Cited on pages 15 & 100.
17. S. Haroche and J.-M. Raimond, *Exploring the quantum: atoms, cavities and photons*. Oxford graduate texts. Oxford University Press, Oxford ; New York, 2006. Cited on pages 15 & 40.
18. A. A. Houck, J. Koch, M. H. Devoret, S. M. Girvin, and R. J. Schoelkopf, "Life after charge noise: recent results with transmon qubits," *Quantum Information Processing* **8**, 105–115 (2009). Cited on page 16.
19. L. DiCarlo, M. D. Reed, L. Sun, B. R. Johnson, J. M. Chow, J. M. Gambetta, L. Frunzio, S. M. Girvin, M. H. Devoret, and R. J. Schoelkopf, "Preparation and measurement of three-qubit entanglement in a superconducting circuit," *Nature* **467**, 574–578 (2010). Cited on pages 16 & 102.
20. M. Hatridge, S. Shankar, M. Mirrahimi, F. Schackert, K. Geerlings, T. Brecht, K. M. Sliwa, B. Abdo, L. Frunzio, S. M. Girvin, R. J. Schoelkopf, and M. H. Devoret, "Quantum back-action of an individual variable-strength measurement," *Science* **339**, 178–181 (2013). Cited on pages 16 & 151.

21. B. D. Josephson, "Possible new effects in superconductive tunnelling," *Physics Letters* **1**, 251–253 (1962). Cited on page 17.
22. C. Ospelkaus, U. Warring, Y. Colombe, K. R. Brown, J. M. Amini, D. Leibfried, and D. J. Wineland, "Microwave quantum logic gates for trapped ions," *Nature* **476**, 181–184 (2011). Cited on page 17.
23. Y. Kubo, I. Diniz, C. Grezes, T. Umeda, J. Isoya, H. Sumiya, T. Yamamoto, H. Abe, S. Onoda, and T. Ohshima, "Electron spin resonance detected by a superconducting qubit," *Phys. Rev. B* **86**, 064514 (2012). Cited on pages 17, 101 & 155.
24. J. Basset, D.-D. Jarausch, A. Stockklauser, T. Frey, C. Reichl, W. Wegscheider, T. M. Ihn, K. Ensslin, and A. Wallraff, "Exploring the single-electron regime of a double quantum dot in the circuit quantum electrodynamics architecture," *arXiv preprint arXiv:1304.5141* (2013). Cited on pages 17 & 155.
25. D. Schuster, *Circuit Quantum Electrodynamics*. PhD thesis, Yale University, 2007. Cited on pages 24, 26, 27, 39, 44, 62, 65, 78 & 105.
26. B. A. Mazin, *Microwave Kinetic Inductance Detectors*. PhD thesis, California Institute of Technology, 2004. Cited on page 25.
27. M. Goppl, A. Fragner, M. Baur, R. Bianchetti, S. Filipp, J. M. Fink, P. J. Leek, G. Puebla, L. Steffen, and A. Wallraff, "Coplanar waveguide resonators for circuit quantum electrodynamics," *J. Appl. Phys.* **104**, 113904 (2008). Cited on pages 26, 63 & 75.
28. K. Yoshida, K. Watanabe, T. Kisu, and K. Enpuku, "Evaluation of magnetic penetration depth and surface resistance of superconducting thin films using coplanar waveguides," *Applied Superconductivity, IEEE Transactions on* **5**, 1979–1982 (1995). Cited on page 27.
29. A. J. Annunziata, D. F. Santavicca, L. Frunzio, G. Catelani, M. J. Rooks, A. Frydman, and D. E. Prober, "Tunable superconducting nanoinductors," *Nanotechnology* **21**, 445202 (2010). Cited on page 28.
30. B. Ho Eom, P. K. Day, H. G. LeDuc, and J. Zmuidzinas, "A wideband, low-noise superconducting amplifier with high dynamic range," *Nat. Phys.* **8**, 623–627 (2012). Cited on page 28.
31. B. A. Mazin, D. Sank, S. McHugh, E. A. Lucero, A. Merrill, J. Gao, D. Pappas, D. Moore, and J. Zmuidzinas, "Thin film dielectric microstrip kinetic inductance detectors," *Appl. Phys. Lett.* **96**, 102504 (2010). Cited on page 28.

32. J. Wenner, R. Barends, R. C. Bialczak, Y. Chen, J. Kelly, E. Lucero, M. Mariani, A. Megrant, P. J. J. O'Malley, D. Sank, A. Vainsencher, H. Wang, T. C. White, Y. Yin, J. Zhao, A. N. Cleland, and J. M. Martinis, "Surface loss simulations of superconducting coplanar waveguide resonators," *Appl. Phys. Lett.* **99**, 113513 (2011). Cited on page 29.
33. J. Gao, M. Daal, A. Vayonakis, S. Kumar, J. Zmuidzinas, B. Sadoulet, B. A. Mazin, P. K. Day, and H. G. Leduc, "Experimental evidence for a surface distribution of two-level systems in superconducting lithographed microwave resonators," *Appl. Phys. Lett.* **92**, 152505 (2008). Cited on pages 28 & 29.
34. M. R. Vissers, J. S. Kline, J. Gao, D. S. Wisbey, and D. P. Pappas, "Reduced microwave loss in trenched superconducting coplanar waveguides," *Appl. Phys. Lett.* **100**, 082602 (2012). Cited on page 28.
35. K. Geerlings, Z. Leghtas, I. M. Pop, S. Shankar, L. Frunzio, R. J. Schoelkopf, M. Mirrahimi, and M. H. Devoret, "Demonstrating a driven reset protocol for a superconducting qubit," *Phys. Rev. Lett.* **110**, (2013). Cited on pages 28 & 116.
36. C. P. Poole, *Electron spin resonance : a comprehensive treatise on experimental techniques*. Wiley, New York [u.a.], 1967. Cited on pages 30, 78 & 82.
37. R. E. Collin, *Foundations for microwave engineering*. IEEE Press, New York, 2001. Cited on page 34.
38. L. Bishop, *Circuit Quantum Electrodynamics*. PhD thesis, Yale University, 2010. Cited on pages 39, 41, 48 & 53.
39. B. Johnson, *Circuit Quantum Electrodynamics II*. PhD thesis, Yale University, 2011. Cited on page 39.
40. J. Chow, *Quantum Information Processing with Superconducting Qubits*. PhD thesis, Yale University, 2010. Cited on pages 39 & 71.
41. S. M. Girvin, "Superconducting qubits and circuits: Artificial atoms coupled to microwave photons," *École d'été Les Houches* (2011). Cited on pages 39 & 40.
42. D. I. Schuster, A. A. Houck, J. A. Schreier, A. Wallraff, J. M. Gambetta, A. Blais, L. Frunzio, J. Majer, B. Johnson, M. H. Devoret, S. M. Girvin, and R. J. Schoelkopf, "Resolving photon number states in a superconducting circuit," *Nature* **445**, 515–518 (2007). Cited on page 40.
43. M. H. Devoret, "Quantum fluctuations in electrical circuits," in *Fluctuations Quantiques/Quantum Fluctuations*, S. Reynaud, E. Giacobino, and J. Zinn-Justin, eds., p. 351. 1997. Cited on pages 41 & 55.

44. D. J. Griffiths, *Introduction to electrodynamics*. Prentice Hall, Upper Saddle River, N.J., 3rd ed ed., 1999. Cited on page 44.
45. J. Koch, M. Y. Terri, J. Gambetta, A. A. Houck, D. I. Schuster, J. Majer, A. Blais, M. H. Devoret, S. M. Girvin, and R. J. Schoelkopf, “Charge-insensitive qubit design derived from the cooper pair box,” *Phys. Rev. A* **76**, 042319 (2007). Cited on pages 44, 48, 52, 107, 132 & 153.
46. L. DiCarlo, J. M. Chow, J. M. Gambetta, L. S. Bishop, B. R. Johnson, D. I. Schuster, J. Majer, A. Blais, L. Frunzio, S. M. Girvin, and R. J. Schoelkopf, “Demonstration of two-qubit algorithms with a superconducting quantum processor,” *Nature* **460**, 240–244 (2009). Cited on page 49.
47. A. Blais, R. S. Huang, A. Wallraff, S. M. Girvin, and R. J. Schoelkopf, “Cavity quantum electrodynamics for superconducting electrical circuits: An architecture for quantum computation,” *Phys. Rev. A* **69**, 062320 (2004). Cited on page 52.
48. S. Filipp, M. Göppl, J. Fink, M. Baur, R. Bianchetti, L. Steffen, and A. Wallraff, “Multi-mode mediated qubit-qubit coupling and dark-state symmetries in circuit quantum electrodynamics,” *Phys. Rev. A* **83**, (2011). Cited on page 54.
49. B. R. Johnson, M. D. Reed, A. A. Houck, D. I. Schuster, L. S. Bishop, E. Ginossar, J. M. Gambetta, L. DiCarlo, L. Frunzio, S. M. Girvin, and R. J. Schoelkopf, “Quantum non-demolition detection of single microwave photons in a circuit,” *Nat. Phys.* **6**, 663–667 (2010). Cited on pages 54, 71, 105, 111 & 154.
50. A. Houck, J. Schreier, B. Johnson, J. Chow, J. Koch, J. Gambetta, D. Schuster, L. Frunzio, M. Devoret, S. Girvin, and R. Schoelkopf, “Controlling the spontaneous emission of a superconducting transmon qubit,” *Phys. Rev. Lett.* **101**, 080502 (2008). Cited on pages 54, 71 & 138.
51. S. E. Nigg, H. Paik, B. Vlastakis, G. Kirchmair, S. Shankar, L. Frunzio, M. H. Devoret, R. J. Schoelkopf, and S. M. Girvin, “Black-box superconducting circuit quantization,” *Phys. Rev. Lett.* **108**, 240502 (2012). Cited on pages 54 & 119.
52. D. F. Walls and G. J. Milburn, *Quantum optics*. Springer, Berlin; New York, 1994. Cited on pages 60, 139 & 140.
53. D. I. Schuster, L. S. Bishop, I. L. Chuang, D. DeMille, and R. J. Schoelkopf, “Cavity QED in a molecular ion trap,” *Phys. Rev. A* **83**, 012311 (2011).
54. J. M. Sage, V. Bolkhovskiy, W. D. Oliver, B. Turek, and P. B. Welander, “Study of loss in superconducting coplanar waveguide resonators,” *J. Appl. Phys.* **109**, 063915 (2011). Cited on page 63.

55. J. Zmuidzinas, “Superconducting microresonators: Physics and applications,” *Annu. Rev. Condens. Matter Phys.* **3**, 169–214 (2012). Cited on page 63.
56. V. B. Braginskii?, V. P. Mitrofanov, V. I. Panov, K. S. Thorne, and C. Eller, *Systems with small dissipation*. University of Chicago Press, Chicago, 1985. Cited on pages 65, 75 & 155.
57. G. Dôme, “RF systems: Waveguides and cavities,” in *AIP Conference Proceedings*, vol. 153, p. 1296. 1987. Cited on page 65.
58. D. F. Santavicca and D. E. Prober, “Impedance-matched low-pass stripline filters,” *Meas. Sci. Technol.* **19**, 087001 (2008). Cited on pages 70 & 150.
59. W. E. Shanks, D. L. Underwood, and A. A. Houck, “A scanning transmon qubit for strong coupling circuit quantum electrodynamics,” *arXiv preprint arXiv:1303.0874* (2013). Cited on page 74.
60. T. Robertson, B. Plourde, T. Hime, S. Linzen, P. Reichardt, F. Wilhelm, and J. Clarke, “Superconducting quantum interference device with frequency-dependent damping: Readout of flux qubits,” *Phys. Rev. B* **72**, 024513 (2005). Cited on page 75.
61. J. H. N. Loubser and J. A. van Wyk, “Electron spin resonance in the study of diamond,” *Reports on Progress in Physics* **41**, 1201 (2001). Cited on pages 78 & 79.
62. J. Twamley and S. D. Barrett, “Superconducting cavity bus for single nitrogen-vacancy defect centers in diamond,” *Phys. Rev. B* **81**, 241202 (2010). Cited on page 78.
63. K. Sandner, H. Ritsch, R. Amsüss, C. Koller, T. Nöbauer, S. Putz, J. Schmiedmayer, and J. Majer, “Strong magnetic coupling of an inhomogeneous nitrogen-vacancy ensemble to a cavity,” *Phys. Rev. A* **85**, 053806 (2012). Cited on pages 78 & 155.
64. R. Amsüss, C. Koller, T. Nöbauer, S. Putz, S. Rotter, K. Sandner, S. Schneider, M. Schramböck, G. Steinhauser, and H. Ritsch, “Cavity QED with magnetically coupled collective spin states,” *Phys. Rev. Lett.* **107**, 60502 (2011). Cited on page 78.
65. H. Wu, R. E. George, J. H. Wesenberg, K. Mølmer, D. I. Schuster, R. J. Schoelkopf, K. M. Itoh, A. Ardavan, J. J. L. Morton, and G. A. D. Briggs, “Storage of multiple coherent microwave excitations in an electron spin ensemble,” *Phys. Rev. Lett.* **105**, 140503 (2010). Cited on page 78.
66. A. M. Tyryshkin, S. A. Lyon, A. V. Astashkin, and A. M. Raitsimring, “Electron spin relaxation times of phosphorus donors in silicon,” *Phys. Rev. B* **68**, 193207 (2003). Cited on pages 79 & 101.
67. G. Feher and E. A. Gere, “Electron spin resonance experiments on donors in silicon. II. electron spin relaxation effects,” *Phys. Rev.* **114**, 1245 (1959). Cited on page 79.

68. D. Schuster, A. Sears, E. Ginossar, L. DiCarlo, L. Frunzio, J. Morton, H. Wu, G. Briggs, B. Buckley, D. Awschalom, and R. Schoelkopf, “High-cooperativity coupling of electron-spin ensembles to superconducting cavities,” *Phys. Rev. Lett.* **105**, 140501 (2010). Cited on page 79.
69. J. A. Weil and J. R. Bolton, *Electron paramagnetic resonance: elementary theory and practical applications*. Wiley-Interscience, Hoboken, N.J, 2nd ed ed., 2007. Cited on page 82.
70. A. M. Prokhorov and V. B. Fedorov, “Antiferromagnetism of free radicals,” *Soviet Journal of Experimental and Theoretical Physics* **16**, 1489 (1963). Cited on page 86.
71. J. A. Van Wyk, E. C. Reynhardt, G. L. High, and I. Kiflawi, “The dependences of ESR line widths and spin-spin relaxation times of single nitrogen defects on the concentration of nitrogen defects in diamond,” *J. Phys. D: Appl. Phys.* **30**, 1790 (1999). Cited on page 89.
72. J. H. van Vleck, “The dipolar broadening of magnetic resonance lines in crystals,” *Phys. Rev.* **74**, 1168–1183 (1948). Cited on page 96.
73. L. K. Alexander, N. Suwuntanasarn, and W. D. Hutchison, “Phosphorus spin coherence times in silicon at very low temperatures,” *arXiv preprint arXiv:1009.4240* (2010). Cited on page 97.
74. P. H. Kasai, “ESR of VO in argon matrix at 4 degree k; establishment of its electronic ground state,” *J. Chem. Phys.* **49**, 4979 (1968). Cited on page 100.
75. L. Robledo, L. Childress, H. Bernien, B. Hensen, P. F. A. Alkemade, and R. Hanson, “High-fidelity projective read-out of a solid-state spin quantum register,” *Nature* **477**, 574–578 (2011). Cited on page 100.
76. G. Balasubramanian, P. Neumann, D. Twitchen, M. Markham, R. Kolesov, N. Mizuochi, J. Isoya, J. Achard, J. Beck, and J. Tessler, “Ultralong spin coherence time in isotopically engineered diamond,” *Nat. Mater.* **8**, 383–387 (2009). Cited on page 100.
77. P. C. Maurer, G. Kucsko, C. Latta, L. Jiang, N. Y. Yao, S. D. Bennett, F. Pastawski, D. Hunger, N. Chisholm, M. Markham, D. J. Twitchen, J. I. Cirac, and M. D. Lukin, “Room-temperature quantum bit memory exceeding one second,” *Science* **336**, 1283– (2012). Cited on pages 100 & 155.
78. R. M. Brown, A. M. Tyryshkin, K. Porfyakis, E. M. Gauger, B. W. Lovett, A. Ardavan, S. A. Lyon, G. A. D. Briggs, and J. J. L. Morton, “Coherent state transfer between an electron and nuclear spin in N@C<sub>60</sub>,” *Phys. Rev. Lett.* **106**, 110504 (2011). Cited on page 101.

79. Y. Kubo, C. Grezes, A. Dewes, T. Umeda, J. Isoya, H. Sumiya, N. Morishita, H. Abe, S. Onoda, and T. Ohshima, “Hybrid quantum circuit with a superconducting qubit coupled to a spin ensemble,” *Phys. Rev. Lett.* **107**, 220501 (2011). Cited on page 101.
80. B. Julsgaard, C. Grezes, P. Bertet, and K. Mølmer, “Quantum memory for microwave photons in an inhomogeneously broadened spin ensemble,” *arXiv preprint arXiv:1301.1500* (2013). Cited on pages 101 & 155.
81. M. D. Reed, L. DiCarlo, S. E. Nigg, L. Sun, L. Frunzio, S. M. Girvin, and R. J. Schoelkopf, “Realization of three-qubit quantum error correction with superconducting circuits,” *Nature* **482**, 382–385 (2012). Cited on page 102.
82. H. Paik, D. Schuster, L. Bishop, G. Kirchmair, G. Catelani, A. Sears, B. Johnson, M. Reagor, L. Frunzio, L. Glazman, S. Girvin, M. Devoret, and R. Schoelkopf, “Observation of high coherence in josephson junction qubits measured in a three-dimensional circuit QED architecture,” *Phys. Rev. Lett.* **107**, 240501 (2011). Cited on pages 102, 123 & 151.
83. K. Gloos, R. S. Poikolainen, and J. P. Pekola, “Wide-range thermometer based on the temperature-dependent conductance of planar tunnel junctions,” *Appl. Phys. Lett.* **77**, 2915 (2000). Cited on page 107.
84. M. D. Reed, L. DiCarlo, B. R. Johnson, L. Sun, D. I. Schuster, L. Frunzio, and R. J. Schoelkopf, “High-fidelity readout in circuit quantum electrodynamics using the jaynes-cummings nonlinearity,” *Phys. Rev. Lett.* **105**, 173601 (2010). Cited on page 109.
85. R. Bianchetti, S. Filipp, M. Baur, J. Fink, M. Göppl, P. J. Leek, L. Steffen, A. Blais, and A. Wallraff, “Dynamics of dispersive single-qubit readout in circuit quantum electrodynamics,” *Phys. Rev. A* **80**, (2009). Cited on page 109.
86. J. J. Sakurai and S. F. Tuan, *Modern quantum mechanics*. Addison-Wesley Pub. Co, Reading, Mass, rev. ed ed., 1994. Cited on page 111.
87. G. Catelani, R. J. Schoelkopf, M. H. Devoret, and L. I. Glazman, “Relaxation and frequency shifts induced by quasiparticles in superconducting qubits,” *Phys. Rev. B* **84**, (2011). Cited on page 117.
88. M. Lenander, H. Wang, R. C. Bialczak, E. Lucero, M. Mariantoni, M. Neeley, A. D. O’Connell, D. Sank, M. Weides, J. Wenner, T. Yamamoto, Y. Yin, J. Zhao, A. N. Cleland, and J. M. Martinis, “Measurement of energy decay in superconducting qubits from nonequilibrium quasiparticles,” *Phys. Rev. B* **84**, (2011). Cited on page 119.
89. L. S. Bishop, J. M. Chow, J. Koch, A. A. Houck, M. H. Devoret, E. Thuneberg, S. M. Girvin, and R. J. Schoelkopf, “Nonlinear response of the vacuum rabi resonance,” *Nat. Phys.* **5**, 105–109 (2008). Cited on pages 119 & 153.

90. L. Sun, L. DiCarlo, M. Reed, G. Catelani, L. Bishop, D. Schuster, B. Johnson, G. Yang, L. Frunzio, L. Glazman, M. Devoret, and R. Schoelkopf, "Measurements of quasiparticle tunneling dynamics in a band-gap-engineered transmon qubit," *Phys. Rev. Lett.* **108**, 230509 (2012). Cited on pages 124 & 152.
91. J. Martinis, S. Nam, J. Aumentado, K. Lang, and C. Urbina, "Decoherence of a superconducting qubit due to bias noise," *Phys. Rev. B* **67**, 094510 (2003). Cited on page 128.
92. J. Eroms, L. C. van Schaarenburg, E. F. C. Driessen, J. H. Plantenberg, C. M. Huizinga, R. N. Schouten, A. H. Verbruggen, C. J. P. M. Harmans, and J. E. Mooij, "Low-frequency noise in josephson junctions for superconducting qubits," *Appl. Phys. Lett.* **89**, 122516 (2006). Cited on page 129.
93. F. Yoshihara, K. Harrabi, A. O. Niskanen, Y. Nakamura, and J. S. Tsai, "Decoherence of flux qubits due to  $1/f$  flux noise," *Phys. Rev. Lett.* **97**, 167001 (2006). Cited on page 130.
94. A. Bermudez, F. Jelezko, M. B. Plenio, and A. Retzker, "Electron-mediated nuclear-spin interactions between distant nitrogen-vacancy centers," *Phys. Rev. Lett.* **107**, 150503 (2011). Cited on page 130.
95. J. Bylander, S. Gustavsson, F. Yan, F. Yoshihara, K. Harrabi, G. Fitch, D. G. Cory, Y. Nakamura, J.-S. Tsai, and W. D. Oliver, "Noise spectroscopy through dynamical decoupling with a superconducting flux qubit," *Nat. Phys.* **7**, 565–570 (2011). Cited on page 130.
96. J. Li, M. P. Silveri, K. S. Kumar, J.-M. Pirkkalainen, A. Vepsäläinen, W. C. Chien, J. Tuorila, M. A. Sillanpää, P. J. Hakonen, E. V. Thuneberg, and G. S. Paraoanu, "Motional averaging in a superconducting qubit," *Nature Communications* **4**, (2013). Cited on page 130.
97. J. Bergli and L. Faoro, "Exact solution for the dynamical decoupling of a qubit with telegraph noise," *Phys. Rev. B* **75**, (2007). Cited on page 130.
98. A. B. Zorin, F.-J. Ahlers, J. Niemeyer, T. Weimann, H. Wolf, V. A. Krupenin, and S. V. Lotkhov, "Background charge noise in metallic single-electron tunneling devices," *Phys. Rev. B* **53**, 13682–13687 (1996). Cited on page 132.
99. D. J. Van Harlingen, T. L. Robertson, B. L. T. Plourde, P. A. Reichardt, T. A. Crane, and J. Clarke, "Decoherence in josephson-junction qubits due to critical-current fluctuations," *Phys. Rev. B* **70**, 064517 (2004). Cited on page 133.
100. C. D. Nugroho, V. Orlyanchik, and D. J. Van Harlingen, "Low frequency resistance and critical current fluctuations in al-based josephson junctions," *Appl. Phys. Lett.* **102**, 142602 (2013). Cited on page 133.

101. L. Faoro and L. Ioffe, “Microscopic origin of critical current fluctuations in large, small, and ultra-small area josephson junctions,” *Phys. Rev. B* **75**, (2007). Cited on page 135.
102. D. I. Schuster, A. Wallraff, A. Blais, L. Frunzio, R. S. Huang, J. Majer, S. M. Girvin, and R. J. Schoelkopf, “ac stark shift and dephasing of a superconducting qubit strongly coupled to a cavity field,” *Phys. Rev. Lett.* **94**, 123602 (2005). Cited on pages 135 & 147.
103. P. Bertet, I. Chiorescu, G. Burkard, K. Semba, C. J. P. M. Harmans, D. P. DiVincenzo, and J. E. Mooij, “Dephasing of a superconducting qubit induced by photon noise,” *Phys. Rev. Lett.* **95**, 257002 (2005). Cited on pages 135, 137 & 148.
104. L. Bishop, E. Ginossar, and S. Girvin, “Response of the strongly driven jaynes-cummings oscillator,” *Phys. Rev. Lett.* **105**, (2010). Cited on page 136.
105. M. Neeley, M. Ansmann, R. C. Bialczak, M. Hofheinz, N. Katz, E. Lucero, A. O’Connell, H. Wang, A. N. Cleland, and J. M. Martinis, “Transformed dissipation in superconducting quantum circuits,” *Phys. Rev. B* **77**, 180508(R) (2008). Cited on page 137.
106. M. Steffen, F. Brito, D. DiVincenzo, S. Kumar, and M. Ketchen, “Decoherence of floating qubits due to capacitive coupling,” *New Journal of Physics* **11**, 033030 (2009). Cited on page 137.
107. A. P. Sears, A. Petrenko, G. Catelani, L. Sun, H. Paik, G. Kirchmair, L. Frunzio, L. I. Glazman, S. M. Girvin, and R. J. Schoelkopf, “Photon shot noise dephasing in the strong-dispersive limit of circuit QED,” *Physical Review B* **86**, 180504 (2012). Cited on page 137.
108. G. Catelani, J. Koch, L. Frunzio, R. J. Schoelkopf, M. H. Devoret, and L. I. Glazman, “Quasiparticle relaxation of superconducting qubits in the presence of flux,” *Phys. Rev. Lett.* **106**, 077002 (2011). Cited on pages 146 & 155.
109. C. Rigetti, J. Gambetta, S. Poletto, B. Plourde, J. Chow, A. Córcoles, J. Smolin, S. Merkel, J. Rozen, G. Keefe, M. Rothwell, M. Ketchen, and M. Steffen, “Superconducting qubit in a waveguide cavity with a coherence time approaching 0.1 ms,” *Phys. Rev. B* **86**, 100506 (2012). Cited on page 147.
110. A. Clerk and D. Utami, “Using a qubit to measure photon-number statistics of a driven thermal oscillator,” *Phys. Rev. A* **75**, (2007). Cited on page 147.
111. I. Serban, E. Solano, and F. K. Wilhelm, “Crossover from weak- to strong-coupling regime in dispersive circuit QED,” *Europhysics Letters (EPL)* **80**, 40011 (2007). Cited on page 149.

112. A. A. Abdumalikov, O. Astafiev, Y. Nakamura, Y. A. Pashkin, and J. S. Tsai, “Vacuum rabi splitting due to strong coupling of a flux qubit and a coplanar-waveguide resonator,” *Phys. Rev. B* **78**, 180502 (2008). Cited on page 152.
113. M. S. Allman, F. Altomare, J. D. Whittaker, K. Cicak, D. Li, A. Sirois, J. Strong, J. D. Teufel, and R. W. Simmonds, “rf-SQUID-Mediated coherent tunable coupling between a superconducting phase qubit and a lumped-element resonator,” *Phys. Rev. Lett.* **104**, 177004 (2010). Cited on page 152.
114. T. Frey, P. J. Leek, M. Beck, A. Blais, T. Ihn, K. Ensslin, and A. Wallraff, “Dipole coupling of a double quantum dot to a microwave resonator,” *Phys. Rev. Lett.* **108**, 046807 (2012). Cited on page 152.
115. M. Brune, F. Schmidt-Kaler, A. Maali, J. Dreyer, E. Hagley, J. M. Raimond, and S. Haroche, “Quantum rabi oscillation: A direct test of field quantization in a cavity,” *Phys. Rev. Lett.* **76**, 1800 (1996). Cited on page 152.
116. J. Schreier, A. Houck, J. Koch, D. Schuster, B. Johnson, J. Chow, J. Gambetta, J. Majer, L. Frunzio, M. Devoret, S. Girvin, and R. Schoelkopf, “Suppressing charge noise decoherence in superconducting charge qubits,” *Phys. Rev. B* **77**, 180502(R) (2008). Cited on pages 152 & 153.
117. G. Kirchmair, B. Vlastakis, Z. Leghtas, S. E. Nigg, H. Paik, E. Ginossar, M. Mirrahimi, L. Frunzio, S. M. Girvin, and R. J. Schoelkopf, “Observation of quantum state collapse and revival due to the single-photon kerr effect,” *Nature* **495**, 205–209 (2013). Cited on page 154.
118. A. G. Fowler, M. Mariantoni, J. M. Martinis, and A. N. Cleland, “Surface codes: Towards practical large-scale quantum computation,” *Phys. Rev. A* **86**, (2012). Cited on page 154.
119. D. P. DiVincenzo, “Fault-tolerant architectures for superconducting qubits,” *Phys. Scr. T137*, 014020 (2009). Cited on page 154.
120. D. L. Underwood, W. E. Shanks, J. Koch, and A. A. Houck, “Low-disorder microwave cavity lattices for quantum simulation with photons,” *Phys. Rev. A* **86**, (2012). Cited on page 155.
121. D. Ristè, C. C. Bultink, K. W. Lehnert, and L. DiCarlo, “Feedback control of a solid-state qubit using high-fidelity projective measurement,” *Phys. Rev. Lett.* **109**, (2012). Cited on page 155.
122. M. D. Reed, B. R. Johnson, A. A. Houck, L. DiCarlo, J. M. Chow, D. I. Schuster, L. Frunzio, and R. J. Schoelkopf, “Fast reset and suppressing spontaneous emission of a superconducting qubit,” *Appl. Phys. Lett.* **96**, 203110 (2010). Cited on page 155.

123. A. A. Clerk, S. M. Girvin, F. Marquardt, and R. J. Schoelkopf, “Introduction to quantum noise, measurement, and amplification,” *Reviews of Modern Physics* **82**, 1155–1208 (2010). Cited on page 170.
124. N. Ramsey, *Molecular beams*. Clarendon Press ; Oxford University Press, Oxford; New York, 1985. Cited on page 176.

## APPENDIX A

---

### Input-Output Theory of Transmission

---

**N**UMERICAL we can derive the transmission of a resonator coupled to several different populations of spins through input-output theory [123]. We begin with the system Hamiltonian in the rotating frame:

$$H = \omega_0 a^\dagger a + \sum_{n=1}^{N_s} \Omega_n s_n + \sum_n (g_n \cdot a^\dagger s_n + g_n^* \cdot s_n^\dagger a) \quad (\text{A.1})$$

Then in the Heisenberg picture, we can describe the time dependent operators  $a$  and  $s$  via:

$$\dot{a} = -i\omega_0 a - (\kappa_c + \kappa_{ci})a - i \sum_{n=1}^{N_s} g_n s_n - \sqrt{\kappa_c} b_{in} e^{-i\omega_d t} \quad (\text{A.2})$$

$$\dot{s}_n = -i\Omega_n s_n - \frac{\kappa_s}{2} s_n - i g_n^* a \quad (\text{A.3})$$

which, after moving to the drive frame,  $\Delta_0 = \omega_0 - \omega_d$ ,  $\Delta_n = \Omega_n - \omega_d$ , making it static:

$$\dot{a} = -i\Delta_0 a - (\kappa_{\text{tot}})a - i \sum_{n=1}^{N_s} g_n s_n - \sqrt{\kappa_c} b_{in} \quad (\text{A.4})$$

$$\dot{s}_n = -i\Omega_n s_n - \frac{\kappa_s}{2} s_n - i g_n^* a \quad (\text{A.5})$$

In order to address the frequency domain, we apply a Fourier transform:

$$[i(\omega - \Delta_0) - \kappa_{\text{tot}}]a - i \sum_{n=1}^N g_n s_n = \sqrt{\kappa_c} b_{\text{in}} \quad (\text{A.6})$$

$$[i(\omega - \Delta_n) - \kappa_s/2]s_n = i g_n^* a \quad (\text{A.7})$$

From which

$$s_n = \frac{i g_n^*}{i(\omega - \Delta_n) - \kappa_s/2} a \quad (\text{A.8})$$

Then:

$$\left[ (i(\omega - \Delta_0) - \kappa_{\text{tot}}) + \sum_{n=1}^{N_s} \frac{|g_n|^2}{i(\omega - \Delta_n) - \kappa_s/2} \right] a = \sqrt{\kappa_c} b_{\text{in}} \quad (\text{A.9})$$

and finally:

$$b_{\text{out}} = b_{\text{in}} \left[ 1 + \kappa_c \left( \frac{1}{i(\omega - \Delta_0) - \kappa_{\text{tot}} + \sum_{n=1}^{N_s} \frac{|g_n|^2}{i(\omega - \Delta_n) - \kappa_s/2}} \right) \right] \quad (\text{A.10})$$

$$\left| \frac{b_{\text{out}}}{b_{\text{in}}} \right|^2 = \left[ 1 + \kappa_c \left( \frac{1}{i(\omega_m - \omega_0) - (\kappa_c + \kappa_{ci}) + \sum_{n=1}^{N_s} \frac{|g_n|^2}{i(\omega_m - \Omega_n) - \kappa_s/2}} \right) \right]^2 \quad (\text{A.11})$$

## APPENDIX B

---

### ESR of Substrates

---

As part of our collaboration with Oxford University, they measured the ESR spectra of several of our typical substrates as part of our collaboration with Oxford University; in Fig. B.1 we see the spectra of c-plane and r-plane sapphire, as well as a high-resistivity silicon wafer and a doped silicon with SiO<sub>2</sub> sample. Cr dopants in sapphire and other ZFS spins present a possible mechanism for dissipation of qubit energy without necessarily having a finite magnetic bias field.

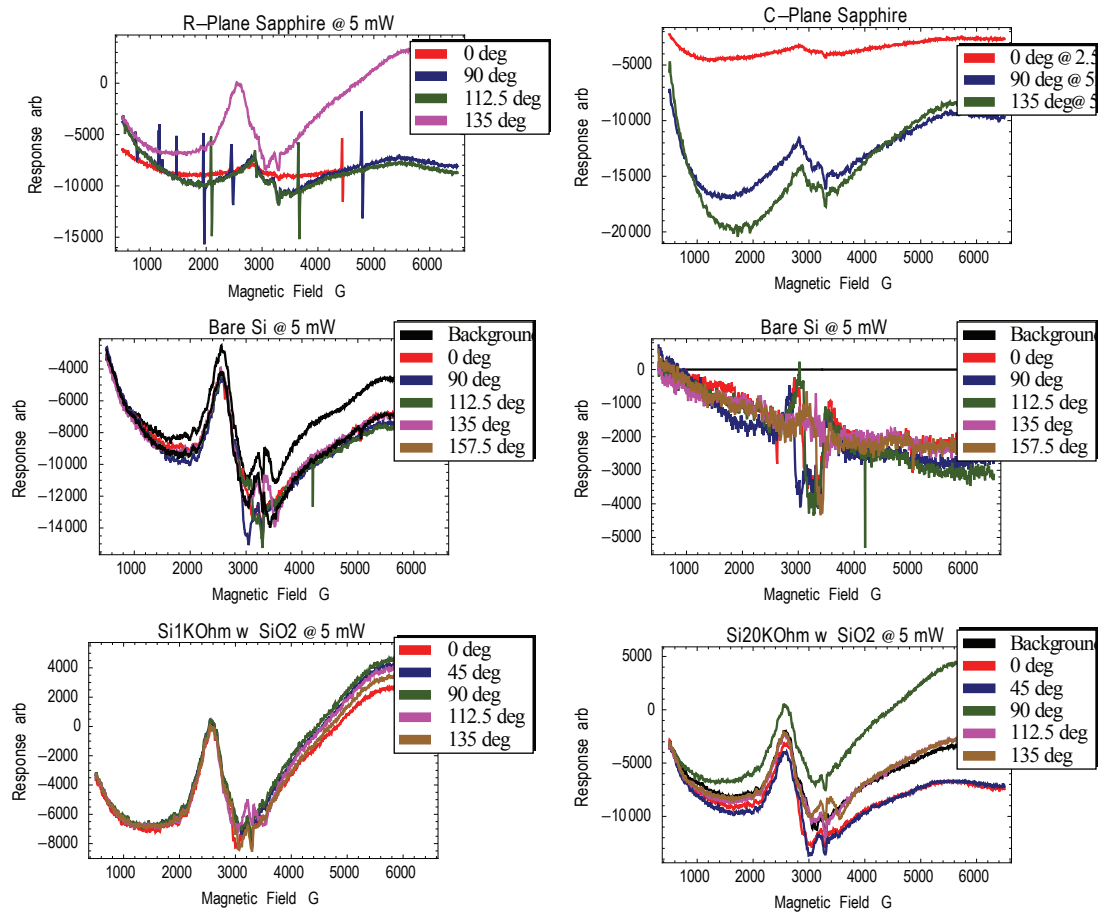


**Figure B.1:** Oxford ESR of our common substrates. These spectra are taken in a cavity at 9.5 GHz, so the peaks at  $\sim 2.5$  kG are for typical paramagnetic spins. The sapphire peaks correspond to unintentional Chromium doping, much like the ruby sample in the next figure. The r-plane sapphire was found to have trace Cr dopants. The results are provided without concentration calibration, which requires the simultaneous measurement of a standard material and close attention to filling factor, etc.

## APPENDIX C

---

### Ramsey Incoherent Response

---

In this section we give a brief explanation of the procedure used to fit the Ramsey experiments. The energy level diagram in Fig. 8.1b can be interpreted as showing that for a given qubit state the cavity is effectively a harmonic oscillator with frequency  $\omega_c$ , or  $\omega_c - \chi$  when the qubit is excited. Assuming long qubit relaxation time  $T_1 \gg 1/\kappa$ , the qubit does not relax during the evolution of the cavity occupation. Then for a given qubit state the dynamics of the probability  $P(N)$  of having  $N$  photons in the cavity at any time  $t$  is governed by the rate equations:

$$\frac{dP(N)}{dt} = \kappa(\bar{n} + 1)(N + 1)P(N + 1) + \kappa\bar{n}NP(N - 1) - \kappa[\bar{n}(N + 1) + (\bar{n} + 1)N]P(N) \quad (\text{C.1})$$

and the steady-state probability  $P_s(N)$  is

$$P_s(\bar{n}, N) = \bar{n}^N / (\bar{n} + 1)^{N+1} \quad (\text{C.2})$$

Now we can introduce the occupation probability  $P(\sigma, N; t)$  for each qubit population  $\sigma$  at time  $t$ . After starting in the qubit ground state, a  $\pi/2$  pulse at the  $N = 0$  peak will coherently split the occupation probability between ground and excited states, leading to an initial

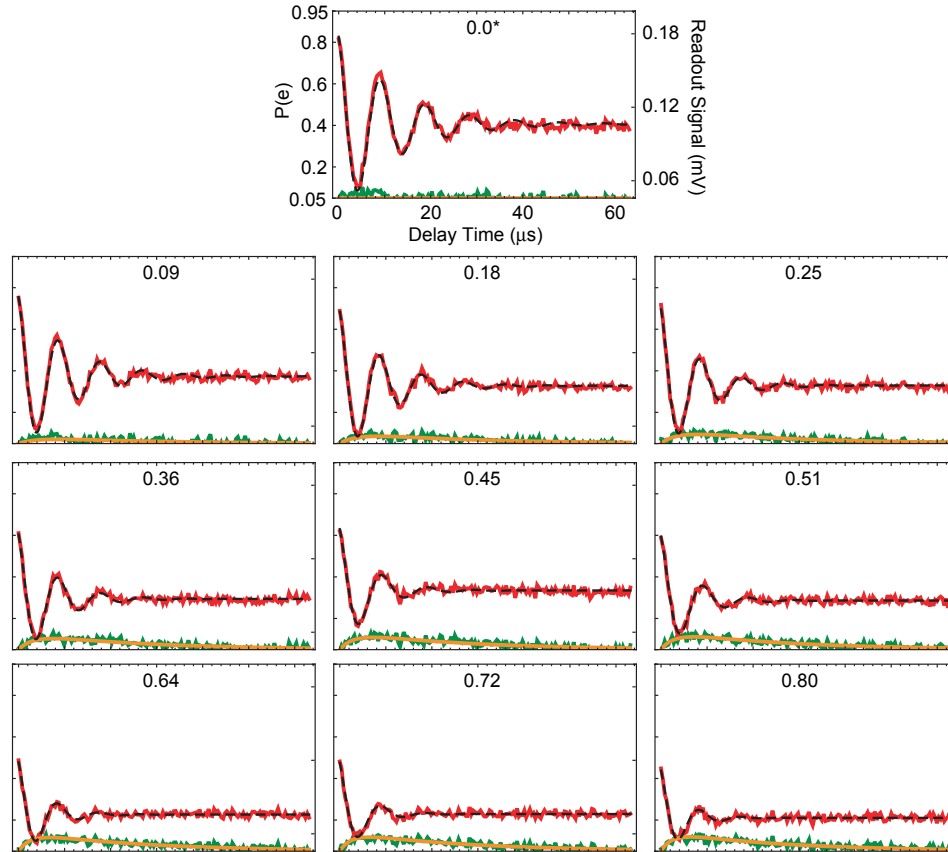


**Figure C.1:** A set of Ramsey experiments similar to those used for the series in Fig. 8.3. Each graph has the same axes and is labelled by the  $\bar{n}_{\text{eff}}$ , as calibrated by the Rabi thermometry experiments. The horizontal axes are the delay time between  $\pi/2$  pulses, and the vertical axes are integrated readout signal and final qubit excitation probability. The adjusted data (red) has had the incoherent readout response (orange) subtracted from the readout signal, before being fit with a exponentially decay sine (dashed). Additionally, the original data after subtracting the final fitted decaying sine is shown (green). At a cavity Q of  $2.5 \times 10^5$ , the photon induced dephasing is much larger than that from (\*) the natural cavity population  $\bar{n}_{\text{eff}} \sim 0.02$  which we find even without applying noise.

excited state probability distribution after the  $\pi/2$  pulse at  $t = 0$

$$P(e, N; 0) = \begin{cases} \frac{1}{2} \frac{1}{1+\bar{n}}, & N = 0 \\ 0, & N > 0 \end{cases} \quad (\text{C.3})$$

After the second  $\pi/2$  pulse at time  $t_f$ , the probability distribution for  $N > 0$  is simply  $P(e, N; t_f)$  as determined by the evolution of  $P(N)$  from the above initial conditions, while  $P(e, 0; t_f)$  is the usual Ramsey fringe signal [124] which we denote  $S_R(t_f)$ , exhibiting decay times which scale according to  $1/\bar{n}\kappa$  (see Fig. 8.3). As the readout sums over all photon number states, the signal  $S(t_f)$  is

$$S(t_f) = S_R(t_f) + P_B(t_f) \quad (\text{C.4})$$

with the ‘‘bump’’  $P_B$  defined as

$$P_B(t_f) = \sum_{N>0} P(e, N; t_f). \quad (\text{C.5})$$

To fit the signal, we need to calculate the function  $P_B(t)$ . This can be done by solving the rate equations (C.1) with the initial conditions (C.3) giving

$$P_B(t) = \frac{1}{2} \frac{\bar{n}}{(1+\bar{n})^2} \frac{1 - e^{-\kappa t}}{1 - \frac{\bar{n}}{1+\bar{n}} e^{-\kappa t}} \quad (\text{C.6})$$

So far we have ignored the qubit and its relaxation. A more detailed analysis gives a reduction of the amplitude of the bump (which we account for with the factor  $M$  in Eq. 8 below) and its relaxation over the  $T_1$  time scale. Then the actual signal is given by

$$S(t_f) = S_R(t_f) + S_B(t_f) \quad (\text{C.7})$$

with

$$S_B(t_f) = M P_B(t_f) e^{-t/T_1}, \quad (\text{C.8})$$

consistent with the dashed curves in Fig. 8.3c-e.

We account for this signal with the following process. First we simulate the system using values obtained via experiment: cavity decay time  $\tau$ , and  $\bar{n}$  obtained through calibration. Then, we take the expected  $S_B(t_f)$  (the excited qubit population with  $N > 0$ ) and remove it from the Ramsey signal, fitting the remainder to a decaying exponential. This typically leads

to a correction to  $\gamma$  that is  $\sim 10 - 30\%$  from the naive Ramsey fit. The products of this process are shown in Fig. C.1 for a series with the same  $\kappa = 1/\tau$  as that in Fig. 8.3.

---

## Copyright Permissions

---